UNIVERSITÉ DE TOURS

École Doctorale MIPTIS

Institut Denis Poisson UMR CNRS 7013, France

THÈSE présentée par :

Aleksandr BEGUN

soutenue le: 15 décembre 2021

pour obtenir le grade de : Docteur de l'université de Tours
Discipline: Physique Théorique

Phase diagram and properties of vortices of PT -symmetric non-Hermitian superfluids

THÈSE dirigée par :

CHERNODUB Maxim	Directeur de Recherche (DR2) CNRS, Université de Tours
MOLOCHKOV Alexander	Professeur, Université Fédérale d'Extrême Orient, Vladivostok, Russie

RAPPORTEURS :

ZAREMBO Konstantin	Professeur, NORDITA, AlbaNova University Center, Stockholm, Suède
MILLINGTON Peter	Nottingham Research Fellow, School of Physics and Astronomy, University of Nottingham, Nottingham, United Kingdom

---

PRÉSIDENT DU JURY

KAZAKOV Vladimir	Professeur Classe Exceptionnelle, 2eme echelon, Ecole Normale Superiore, Paris, France

JURY :

ZAREMBO Konstantin	Professeur, NORDITA, AlbaNova University Center, Stockholm, Suède
MILLINGTON Peter	Nottingham Research Fellow, School of Physics and Astronomy, University of Nottingham, Nottingham, United Kingdom
CHERNODUB Maxim	Directeur de Recherche (DR2) CNRS, Université de Tours
MOLOCHKOV Alexander	Professeur, Université Fédérale d'Extrême Orient, Vladivostok, Russie
NICOLIS Stam	Maître de conférence, Université de Tours
KAZAKOV Vladimir	Professeur Classe Exceptionnelle, 2eme echelon, Ecole Normale Superiore, Paris, France

Acknowledgements

Throughout the writing of this dissertation I have received a great deal of support and assistance.

First and foremost, I am extremely grateful to my supervisors, Prof. Maxim Chernodub and Prof. Alexander Molochkov for their invaluable advice, continuous support, and patience during my PhD study. Their insight and knowledge into the subject matter steered me through this research.

I would like to thank Doctor Peter Millington and Professor Konstantin Zarembo for the acceptance of being the reviewers of my thesis.

I would like to extend my sincere thanks to Professor Stam Nicolis and Professor Vladimir Kazakov for the acceptance of being members of the committee of the jury.

I would like to offer my special thanks to my collegues and friends from Far Eastern Federal university. I would like to offer my special thanks to Anatolii Korneev, who has shared his time during our PhD study. I would particularly like to single out Vladimir Goy for his patience and willingness to answer any my question at any time.

Finally, I would like to express my gratitude to my parents and my wife. Without their tremendous understanding and encouragement in the past few years, it would be impossible for me to complete my study.

Abstract

In this thesis, we discuss the phase diagram and properties of global vortices in the non-Hermitian parity-time symmetric relativistic model possessing two interacting scalar complex fields.

To provide a consistent and complete description of non-Hermitian theories we first consider symmetries that possess existing of the entire real energy spectrum - so-called $\mathcal{PT}$-symmetry. We describe in details methods of solving problems that can arise in non-Hermitian theories and discuss the possibility of applying standard quantum field theorems in non-Hermitian $\mathcal{PT}$-symmetrical theories. We also make a brief description of vortices in both the general case and in the case of strong self-interacting fields.

The phase diagram of the considered theory contains stable $\mathcal{PT}$-symmetric regions and unstable $\mathcal{PT}$-broken regions, which intertwine nontrivially with the $U(1)$-symmetric and $U(1)$-broken phases, thus forming rich patterns in the space of parameters of the model. The notion of the $\mathcal{PT}$ symmetry breaking is generalized to the interacting theory. At finite quartic couplings, the non-Hermitian model possesses classical vortex solutions in the $\mathcal{PT}$-symmetric regions characterized by broken $U(1)$ symmetry. In the long-range limit of two-component Bose-Einstein condensates, the vortices from different condensates experience mutual dissipative dynamics unless their cores overlap precisely. For comparison, we also consider a close Hermitian analogue of the system and demonstrate that the non-Hermitian two-component model possesses much richer dynamics than its Hermitian counterpart.

Résumé

Dans cette thèse, nous discutons du diagramme de phase et des propriétés des tourbillons globaux dans le modèle relativiste symétrique non hermitien possédant deux champs complexes scalaires en interaction.

Pour fournir une description cohérente et complète des théories non hermitiennes, nous considérons d'abord les symétries qui possèdent l'ensemble du spectre d'énergie réelle - ce qu'on appelle la $\mathcal{PT}$-symétrie. Nous décrivons en détail les méthodes de résolution des problèmes qui peuvent survenir dans les théories non hermitiennes, et discutons de la possibilité d'appliquer les théorèmes quantiques standard des champs dans les théories $\mathcal{PT}$-symétriques non hermitiennes. Nous faisons également une brève description des tourbillons à la fois dans le cas général et dans le cas de forts champs auto-interagissants.

Le diagramme de phases de la théorie considérée contient des régions $\mathcal{PT}$-symétriques stables et des régions $\mathcal{PT}$-cassées instables, qui s'entrelacent de manière non triviale avec les phases $U(1)$-symétriques et $U(1)$-cassées, ainsi formant des motifs riches dans l'espace des paramètres du modèle. La notion de brisure de symétrie $\mathcal{PT}$ est généralisée à la théorie de l'interaction. Aux couplages quartiques finis, le modèle non hermitien possède des solutions de vortex classiques dans les régions $\mathcal{PT}$-symétriques caractérisées par une rupture de symétrie $U(1)$. Dans la limite à longue portée des condensats de Bose-Einstein à deux composants, les tourbillons de différents condensats subissent une dynamique dissipative mutuelle à moins que leurs noyaux ne se chevauchent précisément. À titre de comparaison, nous considérons également un analogue hermitien proche du système et démontrons que le modèle à deux composants non hermitien possède une dynamique beaucoup plus riche que son homologue hermitien.

Contents

1 Introduction **19**

2 Peculiar properties of non-Hermitian theories **29**

2.1 $\mathcal{PT}$ symmetry 29

2.2 Unitary time evolution. $\mathcal{CPT}$-inner product 31

2.3 Energy levels and observables of non-Hermitian Hamiltonian 33

2.4 Continuous symmetries and Noether theorem 35

2.4.1 Non-Hermitian Noether theorem 37

2.5 Spontaneous global symmetry breaking at U(1). Goldstone boson . . . 38

2.5.1 Non-Hermitian Goldstone theorem 40

2.6 Vortices in scalar field theory 43

2.7 Gross-Pitaevskii equation 47

2.7.1 Vortices in Gross-Pitaevskii formalism 49

3 The phase diagram and vortex properties of $\mathcal{PT}$-symmetric non-Hermitian two-component superfluid **53**

3.1 (Non-)Hermitian scalar theory 54

3.1.1 Lagrangians 54

3.1.2 Symmetries 55

3.1.3 Ground states 56

3.2 Vortices in fixed-length condensates 68

3.2.1 Vortices in one-component superfluids: brief review 68

3.2.2 Two-component superfluids in long-range limit 73

3.3 Vortices in general case 82

3.4 Discussion and Conclusion 87

Appendices **93**

A Modelling of protein dynamics in terms of Landau-Ginzburg-Wilson approach **93**

A.1 Curves on the plane and in space 94

A.2 Protein structure 97

A.3 Abelian Higgs model 99
A.3.1 Soliton solutions 100
A.4 Protein tertiary structure and the myoglobin phase diagram 101
A.5 Topology and knotty entanglement in protein folding 107

B Technical details of protein modelling **115**
B.1 Building of protein's soliton structure 115
B.2 Simulation of protein dynamics 117

Author's articles

[1] Begun, A. M. and Chernodub, M. N. and Molochkov, A. V. Phase diagram and vortex properties of a $\mathcal{PT}$-symmetric non-Hermitian two-component superfluid // Phys. Rev. D. — 2021, V. 104. — P. 056024.

[2] Begun, A. M., Bornyakov, V.G., Gerasimeniuk, N.V. et al. Analytic Continuation in Lattice QC_2D. Phys. Part. Nuclei 52, 529–535 (2021)

[3] Begun A, Liubimov S, Molochkov A, Niemi A.J. (2021) On topology and knotty entanglement in protein folding. PLOS ONE 16(1): e0244547.

[4] Begun, A. M., Molochkov, A. Niemi, A.J. Protein tertiary structure and the myoglobin phase diagram. Sci Rep 9, 10819 (2019)

[5] Adam K. Sieradzan, Anatolii Korneev, Alexander Begun, Khatuna Kachlishvili, Harold A. Scheraga, Alexander Molochkov, Patrick Senet, Antti J. Niemi, and Gia G. Maisuradze Journal of Chemical Theory and Computation 2021 17 (5), 3203-3220

List of Figures

1.1 Energy levels of the Hamiltonian $H = p^2 - (ix)^N$ as a function of the parameter N. This figure has been taken from the work from Carl M. Bender, Making Sense of Non-Hermitian Hamiltonians, Reports on Progress in Physics 70 nr.6, (2007): 947-1018. 21

1.2 A $\mathcal{PT}$-symmetric optical waveguide. The corresponding symmetric fundamental mode of the structure exists only below a certain critical value of the imaginary index of the waveguide (a). Above this threshold, $\mathcal{PT}$ symmetry is lost and the fundamental mode breaks up into 2 modes: one experiencing gain (b) while the other loss (c). This figure has been taken from the work from A. Guo et al., Observation of $\mathcal{PT}$ -Symmetry Breaking in Complex Optical Potentials, Physical review letters 103 nr.9, (2009): 093902. 23

1.3 The superconducting fluctuations above the superconductor–normal-metal transition in the quasi-1D superconducting wire of the finite length L driven far from equilibrium by an electric field ε. Evolution of the two lowest energy levels. The asymmetry of $\psi_0(x)$ is the signature of the $\mathcal{PT}$-invariance breakdown. This figure has been taken from the work of N. M. Chtchelkatchev et al., Stimulation of the Fluctuation Superconductivity by $\mathcal{PT}$ Symmetry, Physical Review Letters, vol. 109, nr. 15, (2012): 150405 24

1.4 Electronic implementation of a PT-symmetric dimer. The negative resistance gain element is provided by feedback from a voltage-doubling buffer. The coils are inductively coupled, and V_1 and V_2 provide access to the system variables. This figure has been taken from the work from J. Schindler et. al. Experimental study of active LRC circuits with $\mathcal{PT}$ symmetries, Physical Review A, vol. 84, nr. 4, (2011): 040101 24

2.1 The regions in the complex-x plane, where $\psi(x)$ vanishes exponentialy for $N = 4.5$ 34

2.2 Form of potential $V(\phi)$. Panel a) stands for case of $m^2 \geq 0$, panel b) for $m^2 < 0$ 39

2.3 Illustration of number of windings n. a) $n = 0$, b) $n = 1$, c) $n = 2$. . . . 44

2.4 Scheme of potential trap 49

2.5 Wave function modulus of 5000 atoms ^{87}Rb of vortex with $\varkappa = 1$. Unit of length is $a = \sqrt{\hbar/m\omega_\perp}$. x and z axes represent x and z coordinates respectively. This figure has been taken from the work from Lev P. Pitaevskii, Bose-Einstein condensation in magnetic traps. Introduction to the theory, Uspekhi Fizicheskih Nauk 168 nr.6, (1998): 641-653. [71] 51

3.1 The upper panel: (a) the (minus) energy density (3.25) and the condensates (b) v_1 and (c) v_2 in the ground state of the non-Hermitian model (3.5) are shown in the plane of the mass parameter squared m_2^2 and the non-Hermitian mass squared m_5^2. The mass (squared) of the first field ϕ_1 is taken positive, $m_1^2 > 0$, and the quartic couplings for both scalar fields are fixed: $\lambda_1 = \lambda_2 = 1$. The middle panel, with the plots (d), (e) and (f), corresponds to the same quantities obtained for the negative diagonal mass $m_1^2 < 0$. The lower panel, with the plots (g), (h) and (i), depicts the Hermitian case (3.7). All dimensionful quantities are shown in the units of the absolute value of the first mass parameter, $|m_1|$. This figure has been taken from the work from A. Begun et. al, Phase diagram and vortex properties of a $\mathcal{PT}$-symmetric non-Hermitian two-component superfluid, Phys.Rev.D 104 (2021), 056024. 61

3.2 The contour plots of of the condensates of the non-Hermitian (panels (a) and (b)) and Hermitian (panel (c)) models. Panel (a) corresponds to the mass of first field ϕ_1 is taken negative, and (b) to taken positive. 62

3.3 The stable ($\mathcal{PT}$-symmetric, marked by the green colour) region and the unstable (spontaneously $\mathcal{PT}$-broken, marked by the red colour) regions in the interacting non-Hermitian theory in the (m_5^2, m_2^2) plane. The mass squared of the first scalar field takes positive values ($m_1^2 > 0$) at the upper panel and negative values ($m_1^2 < 0$) at the lower panel. The dark green and light green colours denote regions with stable $\mathcal{PT}$-symmetric ground states with non-vanishing and vanishing condensates, respectively. The dark red and light red areas are unstable $\mathcal{PT}$-broken regions with, respectively, nontrivial and vanishing solutions of the classical equations of motion (3.27). This figure has been taken from the work from A. Begun et. al, Phase diagram and vortex properties of a $\mathcal{PT}$-symmetric non-Hermitian two-component superfluid, Phys.Rev.D 104 (2021), 056024. 66

3.4 The stable ($\mathcal{PT}$-symmetric, marked by the green color) region and the unstable (spontaneously $\mathcal{PT}$-broken, marked by the red color) regions in the interacting non-Hermitian theory in the (m_5^2, m_2^2) plane. The mass squared of the first scalar field takes positive values ($m_1^2 > 0$) at the upper panel and negative values ($m_1^2 < 0$) at the lower panel. The dark green and light green colors denote regions with stable $\mathcal{PT}$-symmetric ground states with non-vanishing and vanishing condensates, respectively. The dark red and light red areas are unstable $\mathcal{PT}$-broken regions with, respectively, nontrivial and vanishing solutions of the classical equations of motion (3.27). This figure has been taken from the work from A. Begun et. al, Phase diagram and vortex properties of a $\mathcal{PT}$-symmetric non-Hermitian two-component superfluid, Phys.Rev.D 104 (2021), 056024. 67

3.5 Finite domain wall with a closed boundary C 78

3.6 Pairs of vortices appearing at nonzero Ω 78

3.7 The profile functions of the elementary $n = 1$ vortex solution at the mass parameters $m_2^2 = |m_1^2|$ and $m_5^2 = 0.1|m_1^2|$ with $m_1^2 < 0$ and the equal quartic couplings $\lambda_1 = \lambda_2 = 1$. This figure has been taken from the work from A. Begun et. al, Phase diagram and vortex properties of a $\mathcal{PT}$-symmetric non-Hermitian two-component superfluid, Phys.Rev.D 104 (2021), 056024. 84

3.8 Hermitian and non-Hermitian vortex energies vs. the off-diagonal mass squared m_5^2 in different stability areas (a) $m_2^2 = -m_1^2 > 0$ corresponding to the border of the stable and unstable regions and (b) $m_2^2 = 2.5m_1^2 < 0$ residing within the stable region, at $\lambda_1 = \lambda_2 = 1$, Fig. 3.4(g). This figure has been taken from the work from A. Begun et. al, Phase diagram and vortex properties of a $\mathcal{PT}$-symmetric non-Hermitian two-component superfluid, Phys.Rev.D 104 (2021), 056024. 86

A.1 Aminoacid molecule 97

A.2 Peptide bond formation 98

A.3 Structure of peptide plane 98

A.4 Comparison between simulated (sperm whale) value Q_α that counts the relative number of residues in α-helical posture, and experimentally determined (horse heart) α-helical content during thermal denaturation. Experimental data is adapted from [120]. This figure has been taken from the work from A. Begun et. al, Protein tertiary structure and the myoglobin phase diagram, Scientific Reports vol. 9 (2019), 10819. . . . 104

A.5 (Dis)ordering temperatures for the eight helices A-H at $\mu = 0$, in terms of deviations in torsion angles from their α-helical values. This figure has been taken from the work from A. Begun et. al, Protein tertiary structure and the myoglobin phase diagram, Scientific Reports vol. 9 (2019), 10819. 105

A.6 The R_g phase diagram: Collapsed native state (N), (dis)ordering of F-helix (F), two molten globules (I_a and I_b) and random coil (U) phase are identified. This figure has been taken from the work from A. Begun et. al, Protein tertiary structure and the myoglobin phase diagram, Scientific Reports vol. 9 (2019), 10819. 105

A.7 The phase diagram in terms of the observable Q_α that counts the relative number of residues in α-helical posture, at low temperatures $T < 40$℃. This figure has been taken from the work from A. Begun et. al, Protein tertiary structure and the myoglobin phase diagram, Scientific Reports vol. 9 (2019), 10819. 106

A.8 A 3D view of the AFV3-109 (PDB code 2J6B), the yellow knotting loop extends over residues 8-77 and the red threaded slipknot consists of residues 78-106. This figure has been taken from the work from A. Begun et. al, On topology and knotty entanglement in protein folding, PLOS ONE 16(1) (2021), e0244547. 108

A.9 Multi-soliton model summarizing. Panel (a) shown overlay comparison of PDB structure 2J6B (red) and its multi-soliton structure (blue). The RMS distance between the two structures is 1.23 Å. Panel (b) shows the virtual C_α trace bond and torsion angles, for the PDB structure 2J6B and for its multi-soliton model. This figure has been taken from the work from A. Begun et. al, On topology and knotty entanglement in protein folding, PLOS ONE 16(1) (2021), e0244547. 109

A.10 Panel (a) shows the evolution of radius of gyration R_g of the multi-soliton during the heating stage, and Panel (b) shows the R_g evolution during the cooling stage. The solid line shows the mean value of the simulation ensemble that consist of 1.000 independent cycles, and the spread denotes one standard deviation. Panels (c) and (d) are close looks to the R_g values, at early/late stages of heating/cooling. This figure has been taken from the work from A. Begun et. al, On topology and knotty entanglement in protein folding, PLOS ONE 16(1) (2021), e0244547. . . 110

A.11 The Panel (a) shows the native folded conformation, and the Panel (b) shows the conformation with the minimal R_g value. This figure has been taken from the work from A. Begun et. al, On topology and knotty entanglement in protein folding, PLOS ONE 16(1) (2021), e0244547. . . 111

A.12 The Panel (a) shows the initial increase in the thermal fluctuations $\Delta\tau_{61}$ of the torsion angle located at the proline with residue number 61 (the mean value of τ_{61} and its one standard deviation at the given $\log_{10}(\beta)$ value). The peak that is visible at $\log_{10}(\beta)13 - 12.5$ identifies the β-values where we observe an intermediate trefoil knot. The Panel (b) shows the trefoil knot folding intermediate identified in the Panel (a). The Panel shows that the trefoil knot forms, when the C-terminal of the looped segment pulls out from the knotting loop. This figure has been taken from the work from A. Begun et. al, On topology and knotty entanglement in protein folding, PLOS ONE 16(1) (2021), e0244547. . . 112
A.13 Shows the relative number (in percentage) of slipknotted structures in the final folded ensemble, as a function of Monte Carlo steps after one full heating-cooling cycle. 113

B.1 The graphs of Frenet coordinates of a part of myoglobin 1ABS. Panel (a) stands for PDB data, panel (b) stands for soliton structure 116
B.2 Superposition of experimental (red) and soliton (yellow) protein models. 116

Chapter 1

Introduction

Quantum mechanics is based on several axioms:

- The energy spectrum is required to be real and to be bounded below,
- The operator of time evolution must be unitary,
- Hamiltonian must be Hermitian.

Let us look at all of them.

The first one is obviously necessary, as all results of physical measurements should provide real results. At the same time, the bounded below spectrum guarantees the existence of the lowest energy state. The second one stands for probability conserving so that the total probability should be equal to unity at all moments of time. And the last one is rather mathematical than physical, but it implies that other axioms hold.

However, as some studies show, the latter requirement is optional. In his works, Carl M. Bender asserts [1] that the condition that the Hamiltonian is Hermitian can be replaced by the requirement for its space-time symmetry ($\mathcal{PT}$-symmetry).

$$H = H^{\mathcal{PT}}, \tag{1.1}$$

which is equivalent to the commutation of the Hamiltonian with the combined parity $\mathcal{P}$ and time-reversal inversion $\mathcal{T}$ operation [2], $[\mathcal{PT}, H] = 0$. This combined symmetry leads to a real-valued energy spectrum that ensures the stability of the system. One can show that all $\mathcal{PT}$-symmetric non-Hermitian Hamiltonians belong to the class of the so-called pseudo-Hermitian Hamiltonians $\eta H \eta^{-1} = H^{\dagger}$, where η is a Hermitian linear automorphism [3]. The pseudo-Hermiticity is a generalization of the $\mathcal{PT}$-symmetry which, in turn, depends crucially on the fact that the time-reversal transformation $\mathcal{T}$ is an anti-linear operation. It was shown that the entirely real energy spectrum of $\mathcal{PT}$-symmetric Hamiltonians is a consequence of the pseudo-Hermiticity of the Hamiltonian.

Initially, there were several disconnected discoveries of non-Hermitian Hamiltonians. In 1980 E. Caliceti and co-authors [4] studied the perturbation theory of the

Hamiltonian

$$H = p^2 + x^2 + \beta x^3. \tag{1.2}$$

During the study of Borel summation of divergent perturbation series, they have found that for imaginary β (i.e. non-Hermitian Hamiltonian) all eigenvalues existing are real.

Next, in his article [5] A. Andrianov providing perturbative studies of $-x^4$ potentials, made a proof that such systems might have real eigenvalues. Later, Hollowood [6] found soliton solutions in affine Toda field theories with imaginary coupling constant, which despite of non-unitary form of Lagrangian (1.3) have real classical masses and are stable to small perturbations.

$$\mathcal{L} = \frac{1}{2}\left((\partial_t\phi)^2 - (\partial_x\phi)^2\right) - \frac{m^2}{\gamma^2}\sum_{j=0}^{r} n_j(e^{\gamma\alpha_j\phi} - 1). \tag{1.3}$$

At the same time, F. Scholtz et al. in their paper [7] show how a set of non-Hermitian operators can consistently describe a quantum-mechanical system. They discuss the necessity of the construction of a metric for a set of non-Hermitian observables and the uniqueness of this metric. The authors built a framework for performing calculations with a set of non-Hermitian operators. They stated that the operators must be quasi-Hermitian to consistently describe the system. To do calculations, one needs first to construct the metric concerning the full set of observables. The problem is that the full metric may not exist while it seems that it does if not all observables in the set are quasi-Hermitian.

One should distinguish quasi-Hermitian and pseudo-Hermitian operators. Quasi-Hermitian operators are the operators A which satisfy a relation of the form $GA = A^*G$, where G is a metric operator. Pseudo-Hermitian operator is an operator which can be related to its adjoint through a similarity transformation $H = S^{-1}H^\dagger S$.

In their article [1] Carl M. Bender and Stefan Boettcher investigate a wide class of Hamiltonians of the form

$$H = p^2 + m^2x^2 - (ix)^N. \tag{1.4}$$

They show that such systems can have a real and positive spectrum. In addition, authors mention that Hamiltonian has different phases depending on values of N and m^2: its spectrum can be entirely real, positive and infinite ($\mathcal{PT}$-symmetrical phase), or can have an only finite number of real eigenvalues and an infinite number of complex ones ($\mathcal{PT}$-symmetry is broken), or there can be no any real eigenvalues at all. This phase diagram is shown in Figure 1.1.

C. Bender made an enormous contribution to the study of non-Hermitian systems. In his articles, he developed a mathematical apparatus for working with non-Hermitian Hamiltonians and theoretically substantiated the possibility of their application in describing real systems. In the article [1], Hamiltonians of the form $H = p^2 + x^2(ix)^\nu$

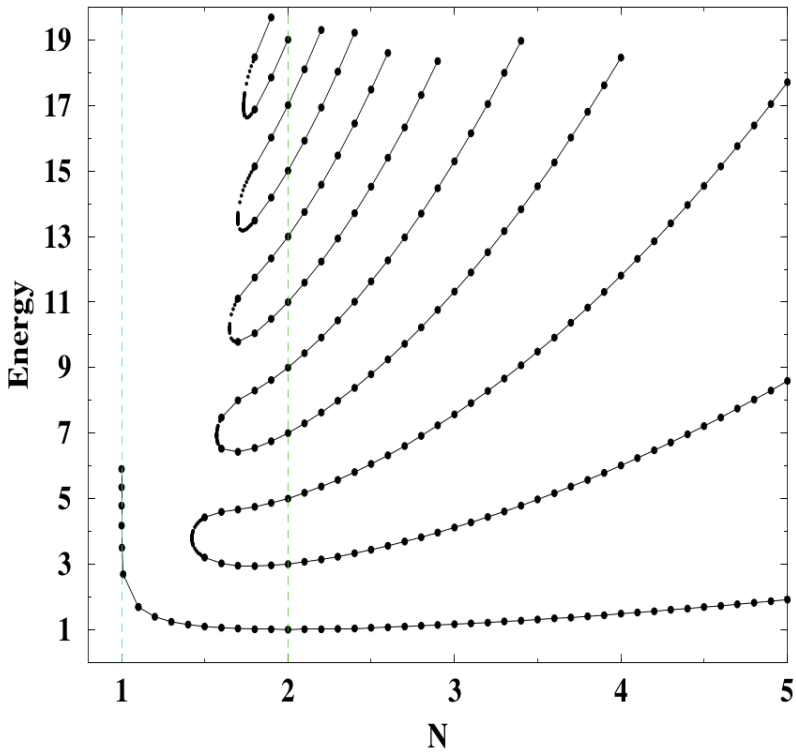

Figure 1.1: Energy levels of the Hamiltonian $H = p^2 - (ix)^N$ as a function of the parameter N. This figure has been taken from the work from Carl M. Bender, Making Sense of Non-Hermitian Hamiltonians, Reports on Progress in Physics 70 nr.6, (2007): 947-1018.

are studied in detail. It is shown that being non-Hermitian, but at the same time $\mathcal{PT}$-symmetric, they can have a real spectrum of eigenvalues and their asymptotic behaviour is considered. To do that, the authors analytically continued the parameter N of Hamiltonian (1.4) to the area of large N. This analytical continuation of the eigenvalue problem requires a correct definition of boundary conditions in the complex plane. Authors use the Stokes and anti-Stokes lines to solve this problem and define areas, where $\psi(x) \to 0$ as $x \to \infty$. They achieve the formula of Hamiltonian's eigenvalues and check its agreement with the WKB approximation.

In an article [8], C. Bender et al. investigated the applicability of supersymmetric quantum mechanics methods to non-Hermitian theories. The application proved to be successful and at the saddle point, the numerical prediction of the ground state energy made it possible to very accurately describe the wave functions and energy eigenvalues for a wide range of N. And even despite of being a saddle point instead of a minimum, stationary point gives the correct physical information. They also note that conventional quantum mechanical norm is not an analytic function, and not invariant under $\mathcal{PT}$ transformation, but the momentum-space version of the norm is.

Also, C. Bender et al. in the article [9] proposed the possibility of a complex contin-

uation of quantum mechanics and proposed a solution to the problem of non-unitary evolution of time by introducing a new symmetry operator $\mathcal{C}$ and a corresponding change in the inner product. C. Bender proved that if $\mathcal{PT}$ symmetry is not spontaneously broken, one can construct extra symmetry $\mathcal{C}$ of Hamiltonian and construct a new inner product which norm would be positive definite. Such procedure is relevant for any $\mathcal{PT}$-symmetrical Hamiltonian and provides the unitary time evolution of the system. Thus Bender and coauthors showed that their theory is a complex generalization of quantum mechanics and not in conflict with it.

Issues of unitarity were also raised in the articles [10, 11] by T. Ohlsson and S. Zhou during investigation of neutrino oscillations with $\mathcal{PT}$-symmetric non-Hermitian Hamiltonians. Authors found that time evolution can be unitary only in the case of Hermitian Hamiltonian. These questions were resolved in the article of J. Alexandre, J. Ellis and P. Millington [12]. They proved that by introducing the orthogonal and consistent with a positive definite norm, the $\mathcal{C}'\mathcal{PT}$ inner product unitarity is respected.

Ideas of non-Hermitian systems have found application in different branches of physics, such as optics [13–18], photonics [19–23], superconducting wires[24, 25], $\mathcal{PT}$-symmetric electronic circuits [26] and also in theoretical studies [27–30].

Formal equivalence between the optical wave equation and Schrodinger equation makes it possible to realize complex PT-symmetric potentials in the framework of optics. In the article [31], the authors studied the beam dynamics in a new type of optical structures possessing $\mathcal{PT}$-symmetric potential. They showed that such structures can provide power oscillations, double refraction, and secondary emission.

Later, in their paper, A. Guo et al. [14] demonstrated experimentally the onset of passive $\mathcal{PT}$-symmetry breaking within the context of optics. They specially designed non-Hermitian guiding potentials and showed that symmetry breaking leads to a loss-induced optical transparency in specially designed pseudo-Hermitian guiding potentials. This paper stimulated the investigation of $\mathcal{PT}$-related features in pseudo-Hermitian lattices. The authors suggested studying power oscillations, optical cavities, and wave propagation in such medium.

Also in [13] author states that light propagation in distributed-feedback optical structures with gain or loss regions is shown to provide an accessible laboratory tool to visualize in optics the spectral properties of the one-dimensional Dirac equation with non-Hermitian interactions. He suggested that phenomena occurring in distributed-feedback (DFB) structures, such as spectral narrowing of resonances and self-oscillation, are the measurable quantities associated with the onset of spectral singularities and $\mathcal{PT}$ symmetry breaking of Dirac Hamiltonians with certain complex couplings. C.E. Ruter with co-authors [15] investigating two Ti in-diffused parallel waveguide channels in Fe-doped $LiNbO_3$ observed spontaneous $\mathcal{PT}$ symmetry braking and power oscillations violating left-right symmetry. These results pave the way to a new class of optical

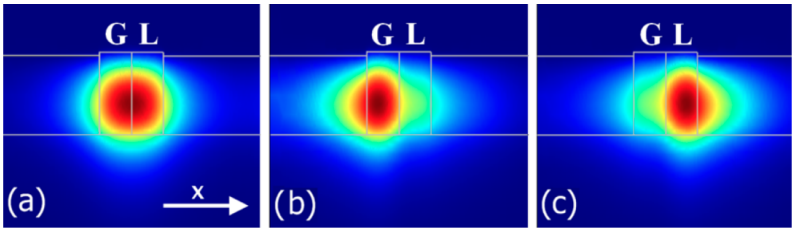

Figure 1.2: A $\mathcal{PT}$-symmetric optical waveguide. The corresponding symmetric fundamental mode of the structure exists only below a certain critical value of the imaginary index of the waveguide (a). Above this threshold, $\mathcal{PT}$ symmetry is lost and the fundamental mode breaks up into 2 modes: one experiencing gain (b) while the other loss (c). This figure has been taken from the work from A. Guo et al., Observation of $\mathcal{PT}$ -Symmetry Breaking in Complex Optical Potentials, Physical review letters 103 nr.9, (2009): 093902.

materials with nonreciprocal light propagation and transverse energy flow.

Ideas of $\mathcal{PT}$ symmetric non-Hermitian Hamiltonians found their application in experiments on superconductors. In [25] N.M. Chtchelkatchev and co-authors are studying superconducting fluctuations above the superconductor-normal metal transition in quasi-1D superconducting wire. They found that the appearance of $\mathcal{PT}$ symmetry in the Cooperon propagator has a strong effect on the structure of fluctuations (see Figure 1.3). Authors demonstrated that with breaking down $\mathcal{PT}$ symmetry by an applied electric field higher than the critical value, the superconducting fluctuations in the weak link, connected to this symmetry, are also destroyed. They also have described using non-Hermitian Hamiltonian experimentally observed differential resistance.

J. Schindler et al. [26] conducted an experiment on a pair of active LRC circuits (see Figure 1.4) with amplification and attenuation, which is a model of a system with gain and loss mechanisms, i.e. $\mathcal{PT}$ symmetrical systems with non-Hermitian Hamiltonians. This simple and mathematically transparent example displays all the universal phenomena encountered in systems with generalized $\mathcal{PT}$ symmetries. The authors highlight that $\mathcal{PT}$-symmetric electronic circuits may be applied in a wide range of problems: from the integrated tuning of antenna arrays to real-time control of exotic metamaterials.

Henning Schomerus in his article [32] shows that non-Hermiticity can provide self-sustained sources of radiation under microreversibility-breaking quantum noise. The self-sustained radiation identified in this work shows that accounting for quantum noise, non-Hermitian $\mathcal{PT}$-symmetric systems are physically distinct from ordinary Hermitian quantum systems: the canonical commutation relations for the input and output operators are only invariant under unitary transformations, which constraints the possibility to introduce alternative scalar products. A. Mostafazadeh [33] offered a physical inter-

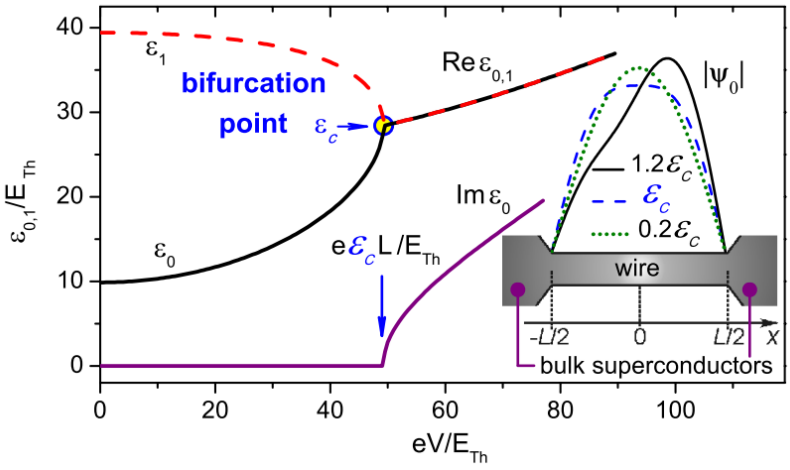

Figure 1.3: The superconducting fluctuations above the superconductor–normal-metal transition in the quasi-1D superconducting wire of the finite length L driven far from equilibrium by an electric field ε. Evolution of the two lowest energy levels. The asymmetry of $\psi_0(x)$ is the signature of the $\mathcal{PT}$-invariance breakdown. This figure has been taken from the work of N. M. Chtchelkatchev et al., Stimulation of the Fluctuation Superconductivity by $\mathcal{PT}$ Symmetry, Physical Review Letters, vol. 109, nr. 15, (2012): 150405

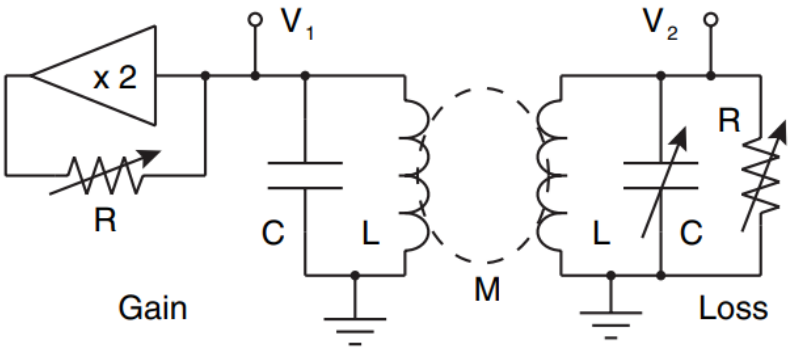

Figure 1.4: Electronic implementation of a PT-symmetric dimer. The negative resistance gain element is provided by feedback from a voltage-doubling buffer. The coils are inductively coupled, and V_1 and V_2 provide access to the system variables. This figure has been taken from the work from J. Schindler et. al. Experimental study of active LRC circuits with $\mathcal{PT}$ symmetries, Physical Review A, vol. 84, nr. 4, (2011): 040101

pretation for the spectral singularities of complex scattering potentials.

Also, there are a lot of theoretical works on non-Hermiticity. Thus, in the article [28] M. Znojil considers two families of theories: with Hermitian and with non-Hermitian Hamiltonian operators. He shows that at a weakly nonlocal interaction potential, these two families can smoothly transform into each other. Hamiltonian symmetries of non-Hermitian systems are widely described in the paper [34] of M. Simon and J. Muga. They provided a super operator formulation of Hamiltonian symmetries and discussed a link between symmetries and conservation laws. A. Fring and T. Frith [29] studied entropy of non-Hermitian quantum systems. They found time-dependent metric by solving the Dyson equation. Three different ways of behaviour of entropy were found depending on the phase of theory ($\mathcal{PT}$-unbroken, $\mathcal{PT}$ spontaneously broken, and the exceptional point). In the unbroken regime, the entropy underwent a rapid decay to zero, at the exceptional point, the entropy decayed asymptotically to zero, and in the spontaneously broken regime, the entropy decayed asymptotically from a maximum to a finite minimum that remained constant with time.

Models with imaginary interaction potentials are studied widely in terms of non-Hermitian Hamiltonians. It was shown in [35] that applied to Hamiltonian $H = \frac{1}{2}(p^2 + m^2x^2) + igx^3$ the linear δ expansion provides naturally real eigenvalues in non-Hermitian $\mathcal{PT}$ symmetric theories. Series of works [35–39] was devoted to investigating of $i\phi^3$ potential. Hermitian models were compared with non-Hermitian analogues and it was shown that non-Hermitian ones also can be energetically stable, trivial, and perturbatively renormalizable. It was shown that because of its stability non-Hermitian $i\phi^3$ theory can have higher predictive power than the ϕ^3 theory.

$\mathcal{PT}$ symmetric $-\phi^4$ theory was considered in work [40]. Authors notice a possibility of this model to play the role of the Higgs mechanism in the standard model. They suggest that replacing the Hermitian Higgs mechanism with the $\mathcal{PT}$ symmetric one can be very beneficial. In the article [41] authors, considering $-\phi^4$ $\mathcal{PT}$ symmetrical model, found a stable Higgs vacuum and make an assumption that the real world is in $\mathcal{PT}$-broken state.

Some quantum field theories such as free fermion theory with a γ_5 mass term, massive Thirring model, sine-Gordon model, described by non-Hermitian $\mathcal{PT}$ symmetrical Hamiltonians were considered in [42]. Authors showed that when $\mathcal{PT}$ symmetry is not broken, theories possess real spectra. It was proved that massive Thirring and sine-Gordon models are equivalent to Hermitian analogues with shifted masses. Potential applications of non-Hermitian mass term in quantum field theories were discussed in [43].

The non-Hermitian massive Thirring Model in (1+1) dimensions was described by C.Bender et al. in Ref. [27]. They showed that this model with the purely imaginary coupling in front of the sine-term resides in the $\mathcal{PT}$-broken domain and, therefore,

should be characterized by complex energy dispersions which correspond to dissipation or instability, or both. Later this theory was discussed by J. Alexandre et al. [44]. They considered a non-Hermitian extension to QED and showed that full gauge invariance of theory is restored with equal Hermitian and anti-Hermitian masses. The authors mention the possibility of explaining the smallness of neutrino masses and providing and an additional source of leptonic $\mathcal{CP}$ violation in non-Hermitian Yukawa theory. On the example of $1 + 1$ lattice model, it was shown by M. Chernodub [45] that in the case of non-Hermitian $\mathcal{PT}$ symmetric theory the excitation spectrum of the theory may contain a non-equal number of left- and right-handed massless fermions. Also, it was demonstrated that the Dirac cone is stable to local disorder.

Applying non-Hermitian $\mathcal{PT}$ symmetric Hamiltonians to describing two-flavour neutrino oscillations [46, 47] can give rise to sub-leading effects in neutrino flavour transitions. The reality of the spectrum of the effective Hamiltonian depends on fundamental parameters of $\mathcal{PT}$ symmetric extension of the usual neutrino oscillation formalism.

Also, non-Hermitian Hamiltonians were suggested to the describing of dark matter [48] and decay of the Higgs boson [30].

In this work, we deal with vortex topological defects in a bosonic non-Hermitian model which involves a pair of scalar fields associated with interacting condensates. The topological solutions in the multicomponent scalar models are interesting because they appear in the models which have applications from condensed matter to high energy physics. Some of these models can serve as viable extensions of the Standard Model of fundamental particle physics [12, 49–51]. Similarly to the Grand Unification particle models and their close counterparts, they host 't Hooft–Polyakov monopole configurations [52] along with complex skyrmions [53] and kink/anti-kink solutions [54] with real-valued energies. As in the Hermitian models, these classical solutions are associated with the saddle points of the corresponding partition functions.

In Chapter 2 we consider the properties of non-Hermitian theories. We discuss how non-Hermitian Hamiltonians can describe real systems. We show how one can solve problems, which are connected with non-Hermiticity, such as complexity of energy spectrum or non-unitary evolution of time operator. We focus on Hamiltonian symmetries, which guarantee an entirely real spectrum of energy and thus can replace the requirement of Hermiticity. We also review the possible solution of the time evolution non-unitarity problem by adding a new symmetry that redefines the inner product and provides allow to avoid this difficulty. We consider Goldstone and Noether theorems in relation to Hermitian and non-Hermitian theories, highlighting differences and similarities of both. We conclude this chapter by describing vortices in the London limit and in the general case as preparing to consider vortices in non-Hermitian scalar field theory.

Next, we continue with an investigation of the non-Hermitian two-component superfluid. In Chapter 3 we introduce the simplest non-Hermitian Lagrangian of scalar field theory that possesses $\mathcal{PT}$-symmetry and thus needs to contain two scalar fields coupled by a mass matrix. Also, the classical Hermitian self-interaction potentials for the scalar fields we added to this Lagrangian. We analyze the ground states of the theory and look for the values of condensates and ground state energy of fields. During all the Chapter we provide a comparison with the Hermitian analogue of considering theory. We also analyze the stability of the ground state and obtain nontrivial rather curious figures for the non-Hermitian case. We notice that the corresponding fluctuation matrix in the $U(1)$ broken phase has one zero eigenvalue which corresponds to the Goldstone mode. Further investigation is dedicated to vortices both in fixed-length condensates and in the general case. We found that both Hermitian and non-Hermitian tend to form pairs, albeit for different reasons. The process of vortex pairs formation is considered in details. The non-Hermitian two-field model possesses vortex solutions also at finite values of the quartic couplings and we focus on the static straight vortex solutions of the classical equations of motion. We solve these equations numerically and obtain profile functions of vortices solutions in both Hermitian and non-Hermitian cases.

It seems interesting to apply the developed apparatus to the real system. The appendix presents the application of topological solitons in one-dimensional scalar field theory with gauge interaction for modelling the structure and dynamics of biopolymers. Topological techniques are often very powerful. They are used with great success to analyze numerous problems in Physics, from theories of fundamental interactions to models of condensed matter. Topology influences on the system's dynamics and possesses a nontrivial phase diagram. Here we propose to introduce topological techniques to study protein folding and dynamics. The protein chain is considered as a piecewise linear curve in terms of Frenet frames. Such formalism allowed us to draw an analogy between Frenet coordinates and fields (scalar and gauge) of the Abelian Higgs model. In the case of one-dimensional model, the gauge field transforms into a scalar field, and we obtain a theory of two scalar fields. Equations of motion provide soliton solutions, which can be considered as one-dimensional vortices, and the entire protein chain is represented as a superposition of such solitons. This approach gives the opportunity to simulate not only the structure but dynamics of proteins. We present the result of modelling myoglobin T-pH phase diagram and investigation of topologically knotted protein. Both studies were successful and are in rather good agreement with experimental data and theoretical predictions.

Chapter 2

Peculiar properties of non-Hermitian theories

2.1 $\mathcal{PT}$ symmetry

Before we have noticed that requirement of Hermiticity, we should replace by the requirement of $\mathcal{PT}$-symmetry. Now we will consider $\mathcal{PT}$ operator in details.

The space-time reflection operator is a sequential action of the parity operator ($\mathcal{P}$) and the time reversal operator ($\mathcal{T}$). The $\mathcal{P}$ operator changes the sign of the coordinate operator and the momentum operator to the opposite:

$$\mathcal{P}\hat{x}\mathcal{P} = -\hat{x}, \tag{2.1}$$

$$\mathcal{P}\hat{p}\mathcal{P} = -\hat{p}. \tag{2.2}$$

The time reversal operator changes only the momentum operator and produces complex conjugation:

$$\mathcal{T}\hat{p}\mathcal{T} = -\hat{p}, \tag{2.3}$$

$$\mathcal{T}i\mathcal{T} = -i. \tag{2.4}$$

In terms of matrix operators

$$\mathcal{P} : \begin{pmatrix} t \\ \mathbf{x} \end{pmatrix} \to P_0 \begin{pmatrix} t \\ \mathbf{x} \end{pmatrix} = \begin{pmatrix} t \\ -\mathbf{x} \end{pmatrix}, \tag{2.5}$$

$$\mathcal{T} : \begin{pmatrix} t \\ \mathbf{x} \end{pmatrix} \to T_0 \begin{pmatrix} t \\ \mathbf{x} \end{pmatrix} = \begin{pmatrix} -t \\ \mathbf{x} \end{pmatrix} \tag{2.6}$$

and corresponding transformation matrices are

$$T_0 = \begin{pmatrix} -1 & 0 & 0 & 0 \\ 0 & 1 & 0 & 0 \\ 0 & 0 & 1 & 0 \\ 0 & 0 & 0 & 1 \end{pmatrix} \tag{2.7}$$

$$P_0 = \begin{pmatrix} 1 & 0 & 0 & 0 \\ 0 & -1 & 0 & 0 \\ 0 & 0 & -1 & 0 \\ 0 & 0 & 0 & -1 \end{pmatrix} \tag{2.8}$$

Combined transformation is just the consequent action of this two operators

$$\mathcal{PT} : \mathbf{x} = \begin{pmatrix} t \\ x \\ y \\ z \end{pmatrix} \rightarrow P_0 T_0 \begin{pmatrix} t \\ x \\ y \\ z \end{pmatrix} = \begin{pmatrix} -t \\ -x \\ -y \\ -z \end{pmatrix} = -\mathbf{x} \tag{2.9}$$

Since both of these operators are reflection operators, their squares give the identity matrix, which can be verified by direct multiplication

$$\mathcal{P}^2 = \mathcal{T}^2 = \mathcal{I}. \tag{2.10}$$

In addition, the operators of spatial and temporal reflection commute with each other and with the Hamiltonian (if it is $\mathcal{PT}$ - symmetric)

$$\mathcal{PT} - \mathcal{TP} = 0, \tag{2.11}$$

$$H(\mathcal{PT}) - (\mathcal{PT})H = 0. \tag{2.12}$$

A system is said to possess unbroken $\mathcal{PT}$ -symmetry if the system is both $\mathcal{PT}$ - symmetric and the Hamiltonian H and $\mathcal{PT}$ operators have the same eigenstates.

Consider eigenvalue equations of the Hamiltonian H and of $\mathcal{PT}$ operator

$$\mathcal{PT}\psi = \lambda\psi, \tag{2.13}$$

$$H\psi = E\psi, \tag{2.14}$$

where ψ is an eigenstate.

Using the property that $\mathcal{PT}$ operator is involutory i.e. $(\mathcal{PT})^2 = 1$, from the first equation we obtain

$$\psi = \mathcal{PT}\lambda\psi = \lambda^*\lambda\psi = |\lambda|^2 \psi, \tag{2.15}$$

and finally

$$\lambda = e^{i\alpha}. \tag{2.16}$$

Next, doing all the same transformations with equation (2.14) it follows that

$$\mathcal{PT}(H\psi) = \mathcal{PT}(E\psi) = E^*\mathcal{PT}(\psi) = E^*\lambda\psi. \tag{2.17}$$

On the other hand, using the commutation relation of Hamiltonian and operator of space-time reflection (2.12) we obtain

$$(\mathcal{PT})H\psi = H\lambda\psi = \lambda H\psi = \lambda E\psi. \tag{2.18}$$

Combining these two results, easy to see that the eigenvalue E is real: $E = E^*$.

Thus, we have shown that in unbroken $\mathcal{PT}$ region non-Hermitian, but $\mathcal{PT}$-symmetric Hamiltonian provides real values of energy and also other physical quantities.

2.2 Unitary time evolution. $\mathcal{CPT}$-inner product

One can argue that non-Hermitian Hamiltonian does not possess unitary time evolution. However, this problem can be solved and below we will give a solution to this problem according to [9].

There is one important difference between non-Hermitian theories and Hermitian ones. It consists in the relation between the left and right eigenfunctions. Cause of this we need to redefine the inner product to possess an orthonormal basis. It can be illustrated by considering 2×2 symmetric Hamiltonian matrix

$$H = \begin{pmatrix} re^{i\theta} & s \\ s & r^{-i\theta} \end{pmatrix}, \tag{2.19}$$

where $r, s, \theta \in \mathbb{R}$. Obviously, this Hamiltonian is not Hermitian, and we need to construct parity and time-reversal operators, which will leave the matrix invariant. As the parity operator we choose matrix

$$\mathcal{P} = \begin{pmatrix} 0 & 1 \\ 1 & 0, \end{pmatrix} \tag{2.20}$$

and time-reversal operator $\mathcal{T}$ performs complex conjugation.

Write down the eigenvalues of Hamiltonian

$$\epsilon_\pm = r\cos\theta \pm \sqrt{s^2 - r^2\sin^2\theta}. \tag{2.21}$$

Easy to see that two parametric regions exist. If $s^2 \geq r^2\sin^2\theta$ then eigenvalues are real, this is the region of unbroken $\mathcal{PT}$ symmetry. In the opposite case, the eigenvalues form a pair of complex conjugated values

$$\epsilon_\pm = r\cos\theta \pm i\sqrt{r^2\sin^2\theta - s^2}, \tag{2.22}$$

and this is the region of broken $\mathcal{PT}$ symmetry.

In the region of unbroken symmetry, setting new variable α

$$\sin\alpha = \frac{r}{s}\sin\theta, \tag{2.23}$$

the eigenvectors of operator H are

$$|\epsilon_+\rangle = N_+ \begin{pmatrix} e^{i\alpha/2} \\ e^{-i\alpha/2} \end{pmatrix}, \tag{2.24}$$

$$|\epsilon_-\rangle = N_- \begin{pmatrix} e^{-i\alpha/2} \\ -e^{i\alpha/2} \end{pmatrix}. \tag{2.25}$$

Values of normalizing coefficients (N_+, N_-) one can obtain from conditions

$$(\epsilon_\pm, \epsilon_\pm) = \pm 1, \tag{2.26}$$

$$(\epsilon_\pm, \epsilon_\mp) = 0, \tag{2.27}$$

with respect to $(u, v) = (\mathcal{PT}u)\dot{v}$

$$N_+ = \frac{1}{\sqrt{2\cos\alpha}}, \tag{2.28}$$

$$N_- = \frac{i}{\sqrt{2\cos\alpha}}. \tag{2.29}$$

The resulting vector space spanned by energy eigenstates has a metric of signature $(+,-)$. It allows us to define a new linear operator $\mathcal{C}$ that is provided by the previously hidden symmetry and acts on the eigenvectors as

$$\mathcal{C}(|\epsilon_\pm\rangle) = \begin{cases} +\,|\epsilon_\pm\rangle \text{ if } |\epsilon_\pm|^2_{\mathcal{PT}} > 0 \\ -\,|\epsilon_\pm\rangle \text{ if } |\epsilon_\pm|^2_{\mathcal{PT}} < 0 \end{cases} \tag{2.30}$$

This operator commutes with the Hamiltonian and $\mathcal{PT}$-operator

$$\mathcal{C}H - H\mathcal{C} = 0, \tag{2.31}$$

$$\mathcal{C}(\mathcal{PT}) - (\mathcal{PT})\mathcal{C} = 0. \tag{2.32}$$

This allows us to define a physically consistent inner product of the form

$$\langle u|v\rangle = (\mathcal{CPT}u)v, \tag{2.33}$$

for which the eigenvectors of H form an orthonormal basis. Also under such inner product a unitary time evolution exists

$$\langle\psi|\psi\rangle_{\mathcal{CPT}} \to \langle\psi|\, e^{-it\hat{H}} e^{it\hat{H}}\, |\psi\rangle_{\mathcal{CPT}} = \langle\psi|\psi\rangle_{\mathcal{CPT}}\,. \tag{2.34}$$

We have discussed both problems of non-Hermitian Hamiltonians, and both of them were solved. The unbroken $\mathcal{PT}$ symmetry guarantees the reality of the spectrum of energy of our system. Unitary time evolution also can be held by non-Hermitian systems if we complete them with a $\mathcal{CPT}$ inner product. It shows that non-Hermitian Hamiltonians in the unbroken $\mathcal{PT}$-symmetric phase can consistently describe a stable physical subsystem.

2.3 Energy levels and observables of non-Hermitian Hamiltonian

Now, let us consider the example of a quantum mechanical non-Hermitian system that is given in [1, 55] by Carl Bender. The authors give a detailed prescription of how to calculate the eigenvalues of the complex Hamiltonian operator. We will briefly describe it in this chapter.

The author describes a family of Hamiltonians of a form

$$\hat{H} = \hat{p}^2 - (i\hat{x})^N, \tag{2.35}$$

where $N \in \mathbb{R}$. In the general case (arbitrary N) these Hamiltonians are not Hermitian, but they an invariant under $\mathcal{PT}$ transformation. The case of $N = 2$ corresponds to the harmonic oscillator. According to Figure 1.1 there are a finite number of real eigenvalues and an infinite number of complex eigenvalues at $1 < N < 2$. This area is said to be a region of broken $\mathcal{PT}$ symmetry. However, at $N \geq 2$ all eigenvalues are real and positive and their number is infinite. And this is a region of unbroken $\mathcal{PT}$ symmetry. With decreasing N from 2 to 1, the number of real eigenvalues decreases and at $N \leq 1.422$ the only eigenvalue remains.

To be able to solve the eigenvalue problem, i.e., to find the energy levels of $\mathcal{PT}$ symmetrical Hamiltonian, one needs to convert it to a Schrodinger differential equation with appropriate boundary conditions and then solve it.

Schrodinger differential equation for considering the model is

$$-\phi_n''(x) - (ix)^N \phi_n(x) = E_n \phi_n(x), \tag{2.36}$$

where E_n are the eigenvalues. Boundary conditions of Hermitian case $\phi_n(\pm x) \to 0$ should be generalized to the complex plane in the case of non-Hermitian theory. To do that, we need to replace the real x axis (as it was at $1 < N < 4$) by a complex plane. The wave function $\psi(x)$ possesses two asymptotics, each with its own region $\psi(x) \to 0$ as $|x| \to \infty$. In complex-x plane, these regions have wedge-shaped form, bounded by the Stokes lines. The centres of the wedges are anti-Stokes lines, $\psi(x)$ vanishes there most rapidly.

For arbitrary N the anti-Stokes lines lie at the angles

$$\theta_1 = -\pi + \frac{(N-2)\pi}{(N+2)2}, \tag{2.37}$$

$$\theta_2 = -\frac{(N-2)\pi}{(N+2)2}, \tag{2.38}$$

and the angle of wedges is

$$\Theta = \frac{2\pi}{N+2}. \tag{2.39}$$

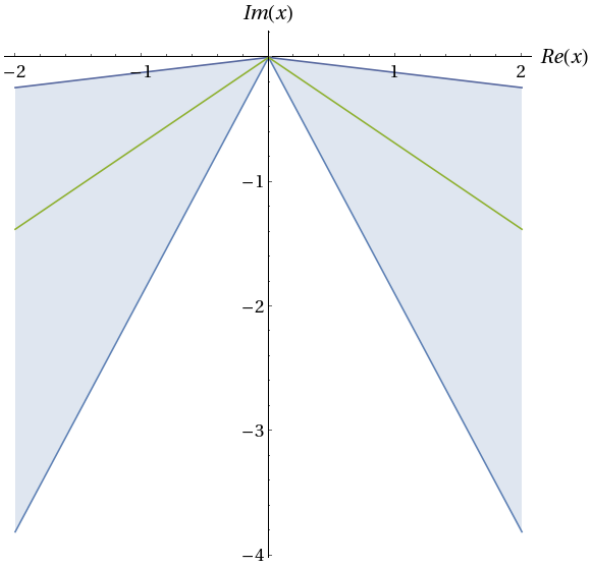

Figure 2.1: The regions in the complex-x plane, where $\psi(x)$ vanishes exponentialy for $N = 4.5$

The WKB quantization condition is

$$(n + 1/2)\pi = \int_{x_-}^{x_+} dx\sqrt{E + (ix)^N}. \tag{2.40}$$

When $N \geq 2$ by integrating the contour one can obtain values of E_n

$$E_n \sim \left[\frac{\Gamma(3/2 + 1/N)\sqrt{\pi}(n + 1/2)}{\sin(\pi/N)\Gamma(1 + 1/N)}\right]^{2N/N+2}. \tag{2.41}$$

These results are in very good agreement with the eigenvalues obtained by the Runge-Kutta method [1].

All physical observables in ordinary quantum mechanics should possess real expectation values, to fulfil this requirement the condition for a linear operator A to be observable is that $A = A^\dagger$. In the case of $\mathcal{PT}$-symmetric theory, the analogous condition is

$$A^T = \mathcal{CPT}A\mathcal{CPT}. \tag{2.42}$$

If condition (2.42) holds at time $t = 0$, then it will continue to hold for all time because we assume that H is symmetric ($H = H^T$). This condition also guarantees that the expectation value of A in any state is real.

Thus the operator $\mathcal{C}$ is observable itself, also the Hamiltonian operator is. But x and p are not observables and it means that there is no position operator in $\mathcal{PT}$-symmetric quantum mechanics as in fermionic theories [55].

2.4 Continuous symmetries and Noether theorem

It is well known in classical mechanics that conserved quantities in many cases can be easily constructed from the Lagrange function. For example, if the Lagrange function is clearly independent of time, then the generalized energy is conserved

$$E = \frac{\partial L}{\partial \dot{q}_i}\dot{q}_i - L. \tag{2.43}$$

If it does not depend on one of the generalized coordinates, then the constant of motion is the corresponding component of the generalized momentum

$$p_i = \frac{\partial L}{\partial \dot{q}_i}. \tag{2.44}$$

These conservation laws are a special case of a more general statement called Noether's theorem [56]. Its essence lies in the fact that each symmetry of the classical action corresponds to some conserved quantity. In particular, in the case of a finite number of degrees of freedom considered in mechanics, the invariance of the action with respect to shifts in time leads to the conservation of the generalized energy, and the invariance with respect to shifts along the cyclic coordinate - to the conservation of the corresponding component of the generalized momentum.

A similar statement can be proved in field theory, i.e., for the case of an infinite number of degrees of freedom. The corresponding theorem is called Noether theorem. K. Stepanjantz in his book [57] suggests the following proof of it.

Noether theorem. Suppose that the action

$$S = \int d^4x \mathcal{L}(\phi_i, \partial_\mu \phi_i, x^\mu) \tag{2.45}$$

is invariant under infinitesimal transformations of coordinates and fields

$$x^\mu \to x'^\mu = x^\mu + \delta x^\mu, \tag{2.46}$$

$$\phi(x) \to \phi'(x,) \tag{2.47}$$

$$\phi'_i(x') = \phi_i(x) + \tilde{\delta}\phi_i(x), \tag{2.48}$$

if the domain of integration M is arbitrary, that is,

$$\int_M' d^4x' \mathcal{L}(\phi'_i(x'), (\partial_\mu \phi'_i)(x'), x') = \int_M d^4x \mathcal{L}(\phi_i(x), (\partial_\mu \phi_i)(x), x). \tag{2.49}$$

Then

$$\frac{d}{dx^\mu}\left[\left(\frac{\partial \mathcal{L}}{\partial(\partial_\mu \phi_i)}\partial_\nu \phi_i) - \delta^\nu_\mu \mathcal{L}\right)\delta x^\nu - \frac{\partial \mathcal{L}}{\partial(\partial_\mu \phi_i)}\tilde{\delta}\phi_i\right] = 0. \tag{2.50}$$

Proof. As the action is invariant under transformations (2.48)

$$0 = \delta S = \int_M' d^4x' \mathcal{L}(\phi'_i(x'), (\partial_\mu \phi'_i)(x'), x') - \int_M d^4x \mathcal{L}(\phi_i(x), (\partial_\mu \phi_i)(x), x). \tag{2.51}$$

Passing in the first integral from integration over x' to integration over x using a change of variables, we obtain that

$$\delta S = \int_M^{\prime} d^4x' \left(\det \frac{\partial x'^{\alpha}}{\partial x^{\beta}} \mathcal{L}(\phi_i'(x'), \frac{\partial x^{\nu}}{\partial x'^{\mu}} \partial_{\nu} \phi_i')(x'), x') - \mathcal{L}(\phi_i(x), (\partial_{\mu}\phi_i)(x), x) \right). \quad (2.52)$$

Note that in this case the region of integration M is assumed to be arbitrary.

Since $x'^{\alpha} = x^{\alpha} + \delta x^{\alpha}$ the Jacobian of the transition can be written as

$$\det \frac{\partial x'^{\alpha}}{\partial x^{\beta}} = \begin{vmatrix} 1 + \partial_0 \delta x^0 & \partial_1 \delta x^0 & \partial_2 \delta x^0 & \partial_3 \delta x^0 \\ \partial_0 \delta x^1 & 1 + \partial_1 \delta x^1 & \partial_2 \delta x^1 & \partial_3 \delta x^1 \\ \partial_0 \delta x^2 & \partial_1 \delta x^2 & 1 + \partial_2 \delta x^2 & \partial_3 \delta x^2 \\ \partial_0 \delta x^3 & \partial_1 \delta x^3 & \partial_2 \delta x^3 & 1 + \partial_3 \delta x^3 \end{vmatrix}. \quad (2.53)$$

Due to the smallness of $\partial_{\beta} \delta x^{\alpha}$ in the lowest approximation, this determinant is equal to 1. It is easy to check that in the next approximation, the terms of the first order in δ_x^{α} can arise only from the product of diagonal elements and turn out to be equal

$$\partial_0 \delta x^0 + \partial_1 \delta x^1 + \partial_2 \delta x^2 + \partial_3 \delta x^3 = \partial_{\mu} \delta x^{\mu}. \quad (2.54)$$

Consequently, up to terms of the first order of smallness in δx^{α}

$$\det \frac{\partial x'^{\alpha}}{\partial x^{\beta}} \approx 1 + \partial_{\mu} \delta x^{\mu}. \quad (2.55)$$

Therefore, the variation of action (2.52) can be written as

$$\delta S = \int d^4x \left(\frac{d\delta x^{\mu}}{dx^{\mu}} \mathcal{L} + \frac{\partial \mathcal{L}}{\partial \phi_i} \tilde{\delta} \phi_i + \frac{\partial \mathcal{L}}{\partial (\partial_{\mu} \phi_i)} (\partial_{\mu} \tilde{\delta} \phi_i - \partial_{\mu} \delta x^{\nu} \delta_{\nu} \phi_i) + \frac{\partial \mathcal{L}}{\partial x^{\mu}} \delta x^{\mu} \right). \quad (2.56)$$

Since the Lagrange function depends on the coordinates both explicitly and through the field variables $\phi_i(x)$, then

$$\frac{d\mathcal{L}}{dx^{\mu}} = \frac{\partial \mathcal{L}}{\partial \phi_i} \partial_{\mu} \phi_i + \frac{\partial \mathcal{L}}{\partial (\partial_{\nu} \phi_i)} \partial_{\mu} \partial_{\nu} \phi_i + \frac{\partial \mathcal{L}}{\partial x^{\mu}}, \quad (2.57)$$

where the total derivatives act on all $\boldsymbol{x}^m u$ (including inside $\phi_i(x)$), and the partial derivatives act only on x^{μ}, which are explicitly present in the Lagrange function. Expressing the partial derivative of the Lagrange function from formula (2.57) and substituting it into (2.56), we obtain that δS can be rewritten as

$$\begin{aligned} \delta S &= \int d^4x \left(\frac{\partial \mathcal{L}}{\partial \phi_i} (\tilde{\delta} \phi_i - \partial_{\nu} \phi_i \delta x^{\nu}) + \frac{\partial \mathcal{L}}{\partial (\partial_{\mu} \phi_i)} (\tilde{\delta} \phi_i - \partial_{\nu} \phi_i \delta x^{\nu}) + \frac{d}{dx^{\mu}} (\mathcal{L} \delta x^{\mu}) \right) \\ &= \int d^4x \frac{d}{dx^{\mu}} \left(\frac{\partial \mathcal{L}}{\partial (\partial_{\mu} \phi_i)} (\tilde{\delta} \phi_i - \partial_{\nu} \phi_i \delta x^{\nu}) + \mathcal{L} \delta x^{\mu} \right) \\ &+ \int d^4x \left(\frac{\partial \mathcal{L}}{\partial \phi_i} - \partial_{\mu} \frac{\partial \mathcal{L}}{\partial (\partial_{\mu} \phi_i)} \right) \left(\tilde{\delta} \phi_i - \partial_{\nu} \phi_i \delta x^{\nu} \right). \end{aligned} \quad (2.58)$$

The last term disappears when using the Lagrange equations, so that on the equations of motion

$$0 = \delta S = \int d^4x \frac{d}{dx^{\mu}} \left(\frac{\partial \mathcal{L}}{\partial (\partial_{\mu} \phi_i)} (\tilde{\phi}_i - \partial_{\nu} \phi_i \delta x^{\nu}) + \mathcal{L} \delta x^{\mu} \right). \quad (2.59)$$

Due to the arbitrariness of the region of integration, the integrand must be equal to 0 for an arbitrary value of the coordinates. So finally,

$$\frac{d}{dx^\mu}\left[\left(\frac{\partial\mathcal{L}}{\partial(\partial_\mu\phi_i)}\partial_\nu\phi_i-\delta^\nu_\mu\mathcal{L}\right)\delta x^\nu-\frac{\partial\mathcal{L}}{\partial(\partial_\mu\phi_i)}\tilde{\delta}\phi_i\right]=0. \tag{2.60}$$

2.4.1 Non-Hermitian Noether theorem

Discussed earlier Noether theorem (Section 2.4) works perfectly in Hermitian theories, but it should be modified in case of non-Hermeticity [58]. In their article authors consider non-Hermitian scalar field theory of two complex fields

$$\mathcal{L}=\partial_\mu\Phi^\dagger\partial^\mu\Phi-\Phi^\dagger\hat{M}^2\Phi, \tag{2.61}$$

where mass matrix M^2 is the source of non-hermiticity

$$M^2=\begin{pmatrix} m_1^2 & m_5^2 \\ -m_5^2 & m_2^2\end{pmatrix}. \tag{2.62}$$

They show that variation of the action

$$\begin{aligned}\delta S=\int d^4x\Bigg[&\left(\frac{\partial\mathcal{L}}{\partial\Phi}-\partial_\nu\frac{\partial\mathcal{L}}{\partial(\partial_\nu\Phi)}\right)\delta\Phi+\delta\Phi^\dagger\left(\frac{\partial\mathcal{L}}{\partial\Phi^\dagger}-\partial_\nu\frac{\partial\mathcal{L}}{\partial(\partial_\nu\Phi^\dagger)}\right)\\&+\delta_\nu\left(\frac{\partial\mathcal{L}}{\partial(\partial_\nu\Phi)}\delta\Phi+\delta\Phi^\dagger\frac{\mathcal{L}}{\partial(\partial_\nu\Phi^\dagger)}\right)\Bigg]\end{aligned} \tag{2.63}$$

provides Euler-Lagrange equations in case of vanishing surface terms by choosing boundary conditions.

But in case of non-Hermitian theory both Euler-Lagrange equations

$$\frac{\delta S}{\delta\Phi^\dagger} = \frac{\partial\mathcal{L}}{\partial\Phi^\dagger}-\partial_\nu\frac{\partial\mathcal{L}}{\partial(\partial_\nu\Phi^\dagger)}, \tag{2.64}$$

$$\frac{\delta S}{\delta\Phi} = \frac{\partial\mathcal{L}}{\partial\Phi}-\partial_\nu\frac{\partial\mathcal{L}}{\partial(\partial_\nu\Phi)} \tag{2.65}$$

can not be satisfied simultaneously, and only one of them can have nontrivial solutions ($\Phi\neq 0$). When we follow the least action principle ($\delta S=0$) we obtain that at least one surface term must provide a finite contribution.

Considering Lagrangian (2.61) yields the standard Noether's current

$$j_i^\nu=\frac{\partial\mathcal{L}}{\partial(\partial_\nu\phi_i)}\delta\phi_i+\mathcal{L}\delta x_i^\nu. \tag{2.66}$$

The Lagrangian (2.61) is invariant under global $U(1)$ transformations

$$\Phi:\Phi\to e^{i\theta}\Phi,\ \text{with}\ \theta\in\mathbb{R}. \tag{2.67}$$

Noether current corresponding to this symmetry

$$j^\nu=j_1^\nu+j_2^\nu=i\left((\phi_1^*\partial^\nu\phi_1-\phi_1\partial^\nu\phi_1^*)+(\phi_2^*\partial^\nu\phi_2-\phi_2\partial^\nu\phi_2^*)\right) \tag{2.68}$$

is no longer conserved

$$\partial_\nu j^\nu = 2im_5^2(\phi_2^*\phi_1 - \phi_1^*\phi_2) \neq 0. \tag{2.69}$$

Authors notice that instead the current

$$j^\nu = j_1^\nu - j_2^\nu, \tag{2.70}$$

corresponding to the transformation

$$\Phi : \begin{pmatrix} \phi_1 \\ \phi_2 \end{pmatrix} \to \begin{pmatrix} e^{-i\theta}\phi_1 \\ e^{i\theta}\phi_2 \end{pmatrix}, \tag{2.71}$$

under which Lagrangian is not invariant, is conserved.

Transformation (2.71) yields Lagrangian

$$\mathcal{L}' = \partial_\nu\phi_1^*\partial^\nu\phi_1 + \partial_\nu\phi_2^*\partial^\nu\phi_2 - m_1^2\left|\phi_1\right|^2 - m_2^2\left|\phi_2\right|^2 - m_5^2e^{2i\theta}\phi_1^*\phi_2 - m_5^2e^{-2i\theta}\phi_1\phi_2^*. \tag{2.72}$$

Although the Lagrangian (2.72) is not equal to the original Lagrangian, their spectra are identical. So, the physical quantities are invariant under the transformation (2.71) and we can interpret $\mathcal{L}'$ as a family of physically equivalent Lagrangians.

Thus in non-Hermitian theories, Noether's theorem is violated and currents corresponding to symmetry are not conserved.

2.5 Spontaneous global symmetry breaking at U(1). Goldstone boson

Another pretty important theorem in quantum field theory is the Goldstone theorem. It states that if there is an exact continuous symmetry of the Hamiltonian or Lagrangian defining the system, and this is no symmetry of the vacuum state (i.e. there is broken symmetry), then there must be at least one spin-zero massless particle called a Goldstone boson.

The observation of the non-Hermitian analogue of the Noether theorem raises the question about existing of $\mathcal{PT}$-symmetric analogue of the Goldstone theorem. To answer this question, first let us consider a simple Hermitian example, that was described in the book of V. Rubakov [59].

We will consider the Lagrangian, that is the simplest example of continuous U(1) symmetry

$$\mathcal{L} = \frac{1}{2}\partial_\mu\phi^*\partial_\mu\phi - m^2\phi^*\phi - \lambda(\phi^*\phi)^2 - c. \tag{2.73}$$

The complex scalar field ϕ can be expressed as a sum of two real scalar fields

$$\phi = \frac{1}{\sqrt{2}}(\phi_1 + i\phi_2). \tag{2.74}$$

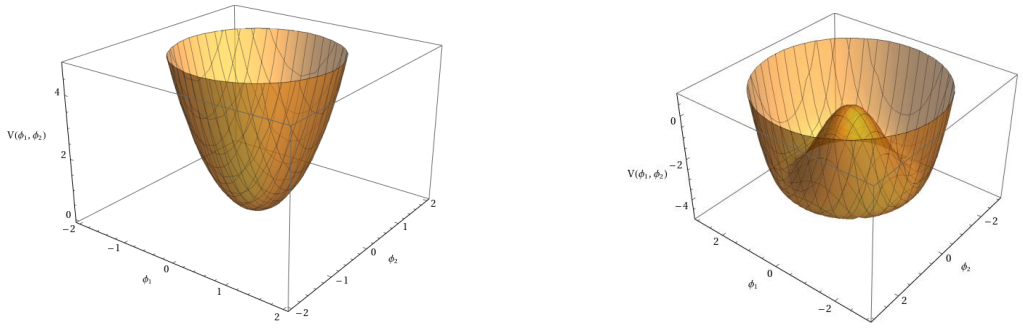

a) b)

Figure 2.2: Form of potential $V(\phi)$. Panel a) stands for case of $m^2 \geq 0$, panel b) for $m^2 < 0$

In terms of this two fields, Lagrangian (2.73) can be rewritten in the next form

$$\mathcal{L} = \frac{1}{2}\partial_\mu \phi_i \partial_\mu \phi_i - \frac{m^2}{2}\phi_i \phi_i - \frac{\lambda}{4}(\phi_i \phi_i)^2 - c, \tag{2.75}$$

where the summation by $i = 1, 2$ is implied.

Global $U(1)$-transformations

$$\phi(x) \to \phi'(x) = e^{i\alpha}\phi(x) \tag{2.76}$$

can be represented in terms of $\phi_{1,2}$ fields,

$$\phi_1 \to \phi_1 \cos\alpha - \phi_2 \sin\alpha, \tag{2.77}$$

$$\phi_2 \to \phi_1 \sin\alpha - \phi_2 \cos\alpha. \tag{2.78}$$

It is easy to see that the Lagrangian of the considered theory is invariant under them.

Consider the energy of the field ϕ

$$E = \int d^3x (\partial_0 \phi^* \partial_0 \phi + \partial_i \phi^* \partial_i \phi + V(\phi^*, \phi)), \tag{2.79}$$

where

$$V(\phi^*, \phi) = m^2 \phi^* \phi + \lambda(\phi^* \phi)^2 + c. \tag{2.80}$$

Ground state is $\phi = 0$ in case of $m^2 \geq 0$. Fluctuations are represented by two real fields ϕ_1 and ϕ_2 of equal mass. $U(1)$ symmetry is not broken.

If $m^2 = -\mu^2 < 0$, potential $V(\phi)$ looks a little more complicated and has a form of the rotational figure shown in Fig.2.2 b). Potential has a continuous set of minima, represented as the circle of radius $\phi_0/\sqrt{2}$

$$\phi = e^{i\alpha}\frac{\phi_0}{\sqrt{2}}, \tag{2.81}$$

where ϕ_0 can be found from the condition of minimum value of potential and equal to

$$\phi_0 = \frac{\mu}{\sqrt{\lambda}}. \tag{2.82}$$

We need to choose one of these minima as the ground state and consider the fluctuations around it.

Let us choose the ground state in the most convenient form for further discussion, as $\phi_1 = \phi_0$, $\phi_2 = 0$, and the fluctuations around it

$$\phi_1(x) = \phi_0 + \chi(x), \tag{2.83}$$

$$\phi_2(x) = \theta(x). \tag{2.84}$$

Taking into account

$$\partial_\mu \phi_1 = \partial_\mu \chi, \tag{2.85}$$

$$\partial_\mu \phi_2 = \partial_\mu \theta \tag{2.86}$$

and choosing $c = \frac{\mu^4}{4\lambda}$ in (2.73) in such way to get zero energy of the ground state, we obtain

$$V = -\frac{\mu^2}{2}[(\phi_0 + \chi)^2 + \theta^2] + \frac{\lambda}{4}[(\phi_0 + \chi)^2 + \theta^2]^2 + \frac{\mu^4}{4\lambda} \tag{2.87}$$

In quadratic order by fields χ and θ we get

$$V = \mu^2 \chi^2. \tag{2.88}$$

There is only one quadratic term in the expression (2.88) and the potential does not depend on θ^2 or $\chi\theta$. The same conclusion can be done from the Fig.2.2, as χ^2 and θ^2 are the curvatures of the potentials in the directions ϕ_1 and ϕ_2, and in the point of the chosen ground state the curvature of the potential in the ϕ_2 direction is equal to zero due to the U(1)-symmetry.

Thus, the quadratic Lagrangian has the form

$$\mathcal{L}^{(2)}_{\chi,\theta} = \frac{1}{2}(\partial_\mu \chi)^2 + \frac{1}{2}(\partial_\mu \theta)^2 - \mu^2 \chi^2. \tag{2.89}$$

According to the Lagrangian (2.89) the field θ is massles, while the field χ has a mass $m_\chi = \sqrt{2}\mu$. This massless mode occurs as a consequence of U(1) symmetry breaking of the ground state [60–62]. This massless field is called the Nambu-Goldstone field, and the corresponding particle is called the Nambu-Goldstone boson.

We have proved the Goldstone theorem using the invariance of Lagrangian. Also, there are several articles, where the proof of this theorem based on the existence of conserved current can be found [63, 64]. For Hermitian theories, both conserving current and symmetry of Lagrangian are equivalent by Noether's theorem.

2.5.1 Non-Hermitian Goldstone theorem

In non-Hermitian theories, where, as we said before, the symmetry of Lagrangian doesn't provide conserving current, Goldstone theorem should be reformulated.

In their paper [50] Alexandre et al. emphasise that in non-Hermitian theories existence of Goldstone mode is connected with a conserved current but not with Lagrangian symmetry. They proved that the Goldstone theorem is applicable to non-Hermitian theories too.

The authors give a general proof of Goldsone's theorem in non-Hermitian theories and, in addition, consider it using a specific example of a non-Hermitian theory of two scalar fields with $U(1)$ symmetry. Considered Lagrangian

$$\mathcal{L} = \partial_\nu \phi_1^* \partial^\nu \phi_1 + \partial_\nu \phi_2^* \partial^\nu \phi_2 + m_1^2 |\phi_1|^2 - m_2^2 |\phi_2|^2 - \mu^2(\phi_1^* \phi_2 - \phi_2^* \phi_1) - \frac{g}{4} |\phi_1|^4 , \quad (2.90)$$

possesses a nontrivial vacuum structure.

This Lagrangian provides equations of motion in the next form:

$$\Box\phi_1 - m_1^2\phi_1 + \mu^2\phi_2 + \frac{g}{2} |\phi_1|^2 \phi_1 = 0, \quad (2.91)$$

$$\Box\phi_1 + m_2^2\phi_2 - \mu^2\phi_1 = 0. \quad (2.92)$$

To obtain the vacuum expectation values, one needs to solve the Euler-Lagrange equations with the condition of coordinate-independent fields

$$m_1^2\phi_1 - \mu^2\phi_2 - \frac{g}{2} |\phi_1|^2 \phi_1 = 0, \quad (2.93)$$

$$m_2^2\phi_2 - \mu^2\phi_1 = 0. \quad (2.94)$$

The solutions of these equations are

$$v_1 = \sqrt{2\frac{m_1^2 m_2^2 - \mu^4}{g m_2^2}}, \quad (2.95)$$

$$v_2 = \frac{\mu^2}{m_2^2}\sqrt{2\frac{m_1^2 m_2^2 - \mu^4}{g m_2^2}}. \quad (2.96)$$

The authors expand the fields by vacuum values v_1, v_2 and fluctuations $\hat{\phi}_1, \hat{\phi}_2$

$$\phi_1 = v_1 + \hat{\phi}_1, \quad (2.97)$$

$$\phi_2 = v_2 + \hat{\phi}_2. \quad (2.98)$$

Using these expressions one can rewrite the equations of motion (2.92) in terms of field fluctuations

$$\Box \begin{pmatrix} \hat{\phi}_1 \\ \hat{\phi}_1^* \\ \hat{\phi}_2 \\ \hat{\phi}_2^* \end{pmatrix} = \begin{pmatrix} \frac{m_1^2 m_2^2 - 2\mu^4}{m_2^2} & \frac{m_1^2 m_2^2 - \mu^4}{m_2^2} & \mu^2 & 0 \\ \frac{m_1^2 m_2^2 - \mu^4}{m_2^2} & \frac{m_1^2 m_2^2 - 2\mu^4}{m_2^2} & 0 & \mu^2 \\ -\mu^2 & 0 & m_2^2 & 0 \\ 0 & -\mu^2 & 0 & m_2^2 \end{pmatrix} \begin{pmatrix} \hat{\phi}_1 \\ \hat{\phi}_1^* \\ \hat{\phi}_2 \\ \hat{\phi}_2^* \end{pmatrix}, \quad (2.99)$$

where terms of higher order were neglected.

Alexandre list all eigenvalues of this mass matrix

$$\lambda_1 = 0, \tag{2.100}$$

$$\lambda_2 = m_2^2 - \frac{\mu^4}{m_2^2}, \tag{2.101}$$

$$\lambda_3 = \frac{2m_1^2m_2^2 - 3\mu^4 + m_2^4 + \sqrt{(2m_1^2m_2^2 - 3\mu^4 + m_2^4)^2 - 4\mu^4 m_2^4}}{2m_2^2}, \tag{2.102}$$

$$\lambda_4 = \frac{2m_1^2m_2^2 - 3\mu^4 + m_2^4 - \sqrt{(2m_1^2m_2^2 - 3\mu^4 + m_2^4)^2 - 4\mu^4 m_2^4}}{2m_2^2}, \tag{2.103}$$

and the corresponding eigenmodes:

$$G_1 = \sqrt{\frac{2m_2^4}{m_2^4 - \mu^4}} \left(\mathrm{Im}\hat{\phi}_1 - \frac{\mu^2}{m_2^2} \mathrm{Im}\hat{\phi}_2 \right), \tag{2.104}$$

which is the Goldstone mode, and

$$G_2 = \sqrt{\frac{2m_2^4}{m_2^4 - \mu^4}} \left(\mathrm{Im}\hat{\phi}_2 - \frac{\mu^2}{m_2^2} \mathrm{Im}\hat{\phi}_1 \right), \tag{2.105}$$

$$G_3 = \sqrt{2} \left[1 - \left(\frac{\mu^2}{\lambda_3^2 - m_2^2} \right)^2 \right]^{-\frac{1}{2}} \left[\mathrm{Re}\hat{\phi}_1 + \frac{\mu^2}{\lambda_3 - m_2^2} \mathrm{Re}\hat{\phi}_2 \right], \tag{2.106}$$

$$G_4 = \sqrt{2} \left[1 - \left(\frac{\mu^2}{\lambda_4^2 - m_2^2} \right)^2 \right]^{-\frac{1}{2}} \left[\mathrm{Re}\hat{\phi}_1 + \frac{\mu^2}{\lambda_4 - m_2^2} \mathrm{Re}\hat{\phi}_2 \right]. \tag{2.107}$$

These Goldstone modes correspond to the conserved current in the non-Hermitian system (2.70). It proved the author's initial statement about the nature of the massless Goldstone mode.

An interesting feature of considered model is providing the exceptional points, where the eigenvalues of the mass matrix become zero. These points were mentioned in the article by P. Mannheim [65], in the articles by A. Fring and T. Taira [51, 66, 67], and by J. Alexandre et. al. [68].

The mass matrix of considered Lagrangian

$$M = \begin{pmatrix} m_1^2 & \mu^2 \\ -\mu^2 & m_2^2 \end{pmatrix} \tag{2.108}$$

possesses following eigenvalues:

$$M_\pm = \frac{m_1^2 + m_2^2}{2} \pm \frac{1}{2}\sqrt{(m_1^2 - m_2^2)^2 - 4\mu^4}. \tag{2.109}$$

Thus, the theory provides two types of exceptional points. First type stands for degenerating of mass matrix eigenvalues at $|\mu| = \frac{|m_1^2 - m_2^2|}{2}$. The second one (zero-exceptional point) $\mu^2 = \pm m_2^2$ stands for the diverging of the Goldstone modes (2.104), (2.105).

J. Alexandre and co-authors in their article [68] state that the Goldstone boson mass remains non-zero at exceptional points, while P. Mannheim [65] obtain opposite results. The difference in results is connected to the different definition of complex conjugation operator, J. Alexandre takes it to be linear, while P. Mannheim uses antilinear interpretation of it.

J. Alexandre concludes that even at the exceptional point the Goldstone boson can obtain mass through spontaneous symmetry breaking in non-Hermitian theories.

2.6 Vortices in scalar field theory

As we will deal with vortex topological defects in a bosonic non-Hermitian model we want to consider the simplest example of vortices in scalar field theory initially. In our presentation, we will closely follow the presentation given in the book of V. Rubakov [59].

A vortex is the simplest soliton in theory with scalars [69]. It arises in the model with the gauge group $U(1)$. We will deal with the model that has only a complex scalar field $\phi(x)$, which is transformed under gauge transformations as follows:

$$\phi(x) \to \phi'(x) = e^{i\alpha(x)}\phi(x). \tag{2.110}$$

Lagrangian of the model has a form

$$\mathcal{L} = \partial_\mu \phi^* \partial^\mu \phi - V(\phi). \tag{2.111}$$

We choose the potential in the form that ensures the emergence of the Higgs mechanism:

$$V(\phi) = -\mu^2 \phi^* \phi + \frac{\lambda}{2}(\phi^* \phi)^2 + \frac{\mu^2}{2\lambda}, \tag{2.112}$$

or, which is equivalent,

$$V(\phi) = \frac{\lambda}{2}(\phi^* \phi - v^2)^2, \tag{2.113}$$

where $v = \frac{\mu}{\sqrt{\lambda}}$.

The scalar field in the unitary gauge can be represented as the sum of the vacuum value and the real field η above it

$$\phi = v + \frac{\eta(x)}{2}, \tag{2.114}$$

where the field $\eta(x)$ has the mass

$$m = \sqrt{2\lambda} v = \sqrt{2}\mu. \tag{2.115}$$

Formula (2.115 is applicable to small fluctuations around vacuum value $\phi = v$.

To find a soliton in this model, we first consider all possible nonsingular field configurations that do not depend on time. We require that the field energy be finite. For the configurations of interest to us, the energy functional has the form

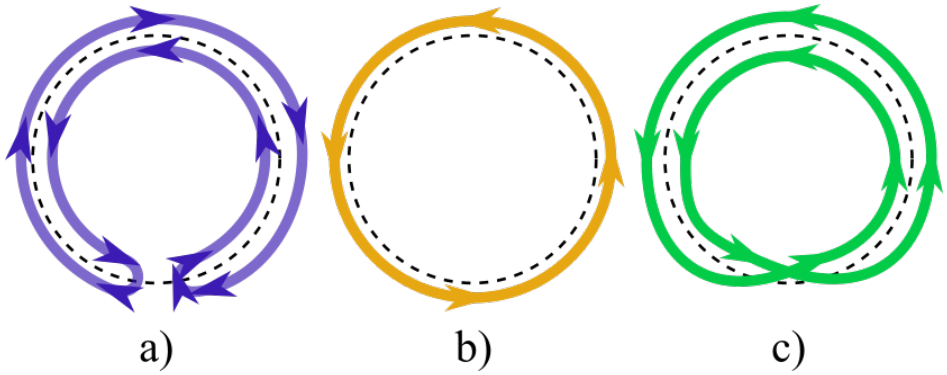

Figure 2.3: Illustration of number of windings n. a) $n = 0$, b) $n = 1$, c) $n = 2$.

$$E[\phi(x)] = \int \left[\partial_i \phi^* \partial^i \phi + V(\phi)\right] d^2x. \tag{2.116}$$

For the energy to be finite, it is necessary that $V(\phi)$ vanish at $|x| \to \infty$, it means that on infinitely large distances scalar field is required to be equal to v.

$$|\phi| \to v \; at \; |x| \to \infty. \tag{2.117}$$

On a centered in the origin circle large enough radius for modulus of ϕ to be equal to vacuum value v, magnitude of the field remains constant ($|\phi| = v$), but the phase may depend on the polar angle on the plane. This dependence can be expressed as the real-valued function $f(\theta)$

$$\phi = e^{if(\theta)}v. \tag{2.118}$$

The function $e^{if(\theta)}v$ specifies the mapping of a circle of radius R in space to a circle of radius v in the plane of complex ϕ. Mappings of a circle into a circle is characterized by an integer $n = 0, \pm 1, \pm 2, ...$ - number of windings. That is the total number of times that curve travels counterclockwise around the point. This can be visualized as placing a rubber ring and on a rigid hoop. The method corresponding to $n = 0$ is to pull the entire ring to one point on the hoop, or to put the ring as shown in Figure 2.3 (a). The mapping with $n = 1$ is the putting of the hoop inside the ring or vice versa (Figure 2.3 (b)); $n = -1$ corresponds to opposite direction of the ring. A mapping with $n = 2$ will turn out if we wrap the ring around the hoop twice, as shown in Figure 2.3(c). The mappings with higher n are obvious and consist of wrapping more and more times. Analytically, mappings with different n can be selected as

$$\phi(\theta) = e^{in\theta}v. \tag{2.119}$$

Even if the phase of the field ϕ is not a gauge invariant, the number of windings is invariant under smooth in the whole space gauge transformations.

As the number of windings is discrete and cannot be changed with a continuous change in the curve, the winding number does not depend on the shape of the curve around the origin if the curve is located in a distant region. From the similar considerations, we can conclude that it also doesn't depend on time evolution of the system if it is smooth in time and doesn't affect on the vacuum value of the field. The set of all fields with finite energy is divided into infinitely many disjoint subsets (sectors) characterized by an integer n.

In fact, formula (2.119) provides all possible asymptotics of the field up to smooth in the whole space gauge transformations. In order to verify this, we note that the number of windings can be written explicitly as

$$n = \frac{1}{2\pi i v^2} \oint dx^i \phi^* \partial_i \phi, \tag{2.120}$$

where the integral is taken over the outer circle. By substituting ϕ in the form of (2.118), we obtain

$$n = \frac{1}{2\pi} \left[f(2\pi) - f(0) \right]. \tag{2.121}$$

Therefore, two fields with the same number of windings differ asymptotically by the phase factor with zero number of windings. If asymptotically

$$\phi_1(x) = e^{i f_1(\theta)} v, \tag{2.122}$$

$$\phi_2(x) = e^{i f_2(\theta)} v, \tag{2.123}$$

and $f_1(2\pi) - f_1(0) = f_2(2\pi) - f_2(0)$, then

$$\phi_2(x) = e^{i f_{21}(x)} \phi_1(x), \tag{2.124}$$

where $f_{21} = f_2 - f_1$ and $f_{21}(2\pi) - f_{21}(0) = 0$. Since f_{21} is a single-valued function of θ, one can construct a smooth gauge function

$$\alpha(r, \theta) = g(r) f_{21}(\theta), \tag{2.125}$$

where $g(r)$ some arbitrarily chosen smooth function satisfying $g(r \to 0) = 0$, $g(r \to \infty) = 1$. Under a gauge transformation with gauge function (2.125, the field ϕ_1 goes into

$$\phi_1'(x) = e^{i\alpha(r,\theta)} \phi_1(x), \tag{2.126}$$

and asymptotics of the fields ϕ_1' and ϕ_2 are the same.

Thus, with the help of gauge transformations that are smooth in the entire space, it is possible to lead the fields to the same asymptotics for each n; the most convenient way is to fix them by the formula 2.119. In each of the sectors of the field space, we now know the asymptotic form of the scalar field.

We will look for a soliton in the sector with $n = 1$. Asymptotically, for $|x| \to \infty$, the scalar field has the form

$$\phi = e^{i\theta} v. \tag{2.127}$$

To obtain a soliton configuration, it is necessary to find a smooth solution of the field equations with asymptotic (2.127). To find the corresponding substitution, we will use a technique that also works in the case of more complex systems. Note that the asymptotic of (2.127) is invariant with respect to spatial rotations supplemented by global phase transformations of the field ϕ, that is,

$$\phi(\theta) = e^{-i\alpha}\phi(\theta + \alpha). \tag{2.128}$$

Write down the most general form of the field invariant under these generalized spatial rotations

$$\phi(r, \theta) = ve^{i\theta}F(r), \tag{2.129}$$

where $F(r)$ is function of the radius, which is needed to be found from field equations.

A not completely trivial property of this substitution is that it passes through the field equations, that is, all the field equations are reduced to one equation for $F(r)$.

Indeed, substituting expression (2.129) into the field equations following from the Lagrangian (2.111), we obtain an ordinary differential equation for function $F(r)$,

$$-\frac{d}{dr}\left(r\frac{dF}{dr}\right) + \lambda v^2 rF(F^2 - 1) + \frac{F}{r} = 0. \tag{2.130}$$

From (2.127) it follows that the function $F(r)$ has the following asymptotic:

$$F(r) \to 1 \text{ with } r \to \infty. \tag{2.131}$$

In addition, the requirement for the smoothness of the field at $r = 0$ imposes the condition

$$F(r) \to 0 \text{ with } r \to 0. \tag{2.132}$$

For large r, we will look for the family of solutions in the form $F(r) = 1 - f(r)$, and we require $f(r) \to 0$ at $r \to \infty$. By linearizing the equation (2.130) we get

$$\frac{1}{r}\frac{d}{dr}\left(r\frac{df}{dr}\right) - m^2 f = 0, \tag{2.133}$$

and obtain a family of solutions decreasing at $r \to \infty$,

$$f(r) = C\frac{e^{-mr}}{\sqrt{r}}, \tag{2.134}$$

where C is a free constant.

Let's consider the family of solutions in the region of $r \to 0$. At small r we have

$$F(r) = \alpha r + \beta r^3 + ..., \tag{2.135}$$

where α, β are unknown constants. Substituting this expression in (2.130) and equating the terms at the same powers of r, we obtain that α and β are connected with

$$\beta = -\frac{m^2}{16}\alpha. \tag{2.136}$$

The solution of interest to us satisfies both conditions (2.132) and 2.131. In other words, a solution from the first family, characterized by a value of C, must be matched with one of the solutions of the second family with some α and β. The conditions for joining two solutions at some point r_0 is the equalities of the function $F(r_0)$ and its derivative $F'(r_0)$ at this point. This requirement gives two equations for two unknown parameters C and α, i.e., the number of parameters coincides with the number of equations for them. Such a system, as a rule, has a solution (one or a discrete set), which serves as a serious argument in favour of the existence of solutions of interest to us.

2.7 Gross-Pitaevskii equation

Now, let us discuss the non-relativistic limit of the previously considered scalar field theory. In this limit, the model describes a rarefied Bose gas that provides the superfluidity. The dynamics of such superfluid can be described by the Gross-Pitaevskii equation [70]. This equation possesses the appearance of vortices in Bose condensate.

The foundations of the theoretical description of a rarefied Bose gas were formulated by N.N. Bogolyubov in 1947. The main point of its approximation consists in separating from the second-quantized operator of annihilation ψ the elements of its classical part, which describes the condensate:

$$\hat{\psi}(\mathbf{r},t) \approx \sqrt{n_0} + \hat{\theta}(\mathbf{r},t), \tag{2.137}$$

where $\sqrt{n_0} = \text{const}$. In a rarefied gas $\theta \ll \sqrt{n_0}$. Here, the density of the condensate is $n_0 = N_0/V$, which is the number of atoms in the unit volume of the condensate. Considering the quantum part of the ψ-operator θ as a small perturbation, Bogolyubov constructed a theory of the "first-order" (with respect to quantum effects) of a spatially homogeneous Bose gas.

The same idea can be used in the case of an inhomogeneous gas. The difference is that in this case there is a nontrivial theory of "zero" order, in which the operator properties of $\hat{\psi}$ can be completely neglected. The fact is that the interaction is not a small correction, but has a great influence on the behaviour of condensed atoms.

L. P. Pitaevskii gives a detailed description of this phenomenon in his review [71].

A generalization of Bogolyubov's prescription for ψ operator to the case of a spatially inhomogeneous gas has the form:

$$\hat{\psi}(\mathbf{r},t) \approx \psi_0(\mathbf{r},t) + \hat{\theta}(\mathbf{r},t). \tag{2.138}$$

The task is to obtain an equation for the classical wave function of the condensate ψ_0. Consider the exact operator equation for the ψ operator in the Heisenberg

representation:

$$i\hbar\frac{\partial}{\partial t}\hat{\psi}(\mathbf{r},t)=\left[-\frac{\hbar^2\nabla^2}{2m}+V_{ext}(\mathbf{r})+\int\hat{\psi}^\dagger(\mathbf{r}',t)V(\mathbf{r}'-\mathbf{r})\hat{\psi}(\mathbf{r}',t)d\mathbf{r}'\right]\hat{\psi}(\mathbf{r},t), \quad (2.139)$$

where $V_{ext}(\mathbf{r})$ - trap holding potential, $V(\mathbf{r}'-\mathbf{r})$ - potential of pair interaction between atoms. The difficulty lies in the fact that neglecting the letter in (2.139) means neglecting all correlations between atoms, which is impossible at distances of the order of the radius r_0 of action of the interatomic potential V. This difficulty does not exist, however, if the potential V satisfies the conditions of applicability of the Born approximation. In this case, we can safely replace $\hat{\psi}$ by ψ_0 and take out the function ψ, which is slowly varying at distances r_0, out of the integral. As a result, we have:

$$i\hbar\frac{\partial}{\partial t}\hat{\psi}_0(\mathbf{r},t)=\left[-\frac{\hbar^2\nabla^2}{2m}+V_{ext}(\mathbf{r})+g\left|\psi_0(\mathbf{r},t)\right|^2\right]\psi_0(\mathbf{r},t), \quad (2.140)$$

where

$$g=\int V(\mathbf{r})d\mathbf{r}. \quad (2.141)$$

Formula (2.141) can be rewritten as

$$g=\frac{4\pi\hbar^2 a}{m}, \quad (2.142)$$

where a is the amplitude of scattering of slow atoms by each other in the Born approximation (the condition for the applicability of this approximation can be written as $a\ll r_0$). We now use the circumstance that, as follows from general considerations, the properties of a rarefied gas at low temperature are completely determined by the scattering amplitude regardless of the properties of the potential V. This means that (2.140) is valid regardless of the applicability of the Born approximation if under the quantity a in (2.142) is to understand the exact scattering amplitude.

Note that the neglect of correlations made in the derivation of (2.140) is often called the "mean field approximation."

Equation (2.140) was found independently in 1961 by E.P. Gross [72] and L.P. Pitaevskii [73].

Equation (2.140) describes the dynamics of an inhomogeneous rarefied Bose gas at zero temperature, $T=0$. This equation is classical in the sense that the function ψ_0 is not an operator and determines not the probability density, but the real distribution of condensate atoms in space. The modulus ψ_0 and the gradient of its phase have a clear classical meaning:

$$\psi_0 = |\psi_0|\,e^{i\Phi}, \quad (2.143a)$$

$$n(\mathbf{r},\mathbf{t}) \approx n_0(\mathbf{r},t)=|\psi_0|^2, \quad (2.143b)$$

$$\mathbf{v}(\mathbf{r},t) = \frac{\hbar}{m}\nabla\Phi, \quad (2.143c)$$

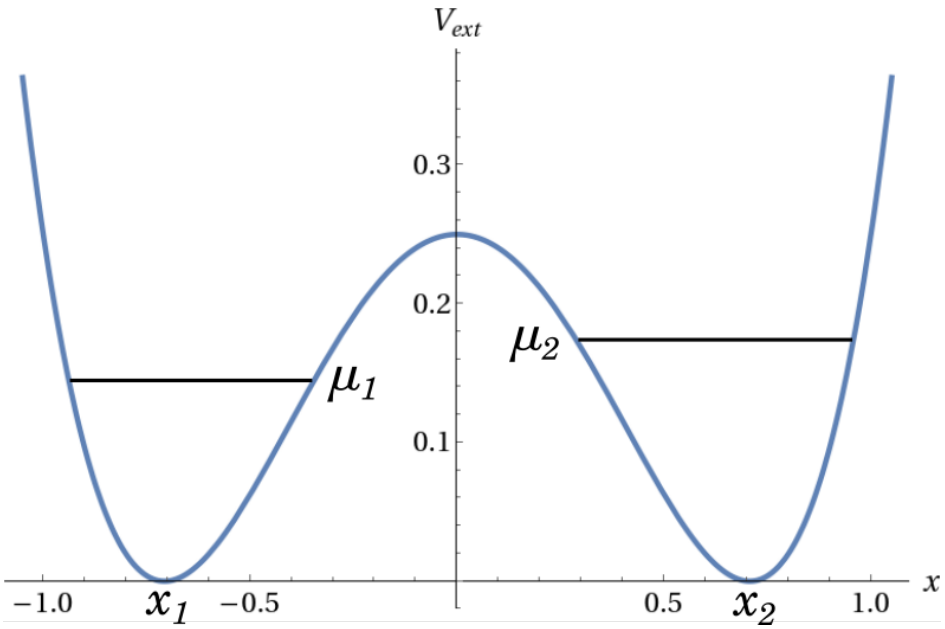

Figure 2.4: Scheme of potential trap

where n and $\mathbf{v}$ are number of atoms per unit volume and their velocity correspondingly.

With respect to equations (2.143) Gross-Pitaevskii equation (2.140) can be rewritten as a system of equations for n and Φ. The first equation has the form of the usual hydrodynamic equation of continuity:

$$\frac{\partial}{\partial t}n + \nabla \cdot (\mathbf{v}n) = 0. \tag{2.144}$$

The second is similar to the Josephson equation in the theory of superconductivity:

$$\hbar\frac{\partial}{\partial t}\Phi + \left(\frac{1}{2}m\mathbf{v}^2 + V_{ext} + gn - \frac{\hbar^2}{2m\sqrt{n}}\nabla^2\sqrt{n}\right) = 0. \tag{2.145}$$

If the gas is in the ground state, the wave function ψ_0 depends on time according to the law $\psi_0 \sim e^{-i\mu t/\hbar}$, where μ is the chemical potential of the gas. Thus, the density distribution in the ground state is determined by the equation:

$$\left(-\frac{\hbar^2\nabla^2}{2m} + V_{ext}(\mathbf{r}) - \mu + g\left|\psi_0(\mathbf{r},t)\right|^2\right)\psi_0(\mathbf{r},t) = 0. \tag{2.146}$$

2.7.1 Vortices in Gross-Pitaevskii formalism

Consider the simplest one-dimensional symmetric trap shown schematically in Figure 2.4. Let the magnetic trap consist of two potential wells separated by a potential barrier. If the chemical potentials of the atoms in these two wells are different, an oscillating stream of atoms will flow between them.

If the numbers of atoms in the wells are different, their chemical potentials μ_1 and μ_2 will also be different. We will assume that the barrier between the two pits is

high enough. Equation (2.146) then has solutions of two types. The first, which we will denote $\psi_1(x)$, corresponds to the chemical potential μ_1 and is localized in well 1. The second solution $\psi_2(X)$ with chemical potential μ_2 is localized in well 2. These two functions overlap only in the classically forbidden region barrier, where they are small, and the nonlinear term in the equation can be neglected. As a result, a linear combination of the form

$$\psi(x,t) = \psi_1(x)e^{-i\frac{\mu_1 t}{\hbar}} + \psi_2(x)e^{-i\frac{\mu_2 t}{\hbar}} \tag{2.147}$$

is a time-dependent solution to the Gross-Pitaevskii equation (2.140). Now it is easy to calculate the flux of atoms corresponding to the wave function (2.147):

$$\begin{aligned} I &= \frac{i\hbar}{2m}\left[\psi(x,t)\frac{\partial}{\partial x}\psi^*(x,t) - \psi^*(x,t)\frac{\partial}{\partial x}\psi(x,t)\right] \\ &= I_0 \sin\left[\Phi_2(t) - \Phi_1(t)\right] = I_0 \sin\frac{(\mu_1-\mu_2)t}{\hbar}, \end{aligned} \tag{2.148}$$

where $I_0 = (\hbar/m)(\psi_1\psi_2' - \psi_2\psi_1')$.

One of the most characteristic features of superfluid systems is the existence of quantized Onsager-Feynman vortices in them. Such a vortex is a special line, around which the phase Φ of the wave function of the condensate changes by $2\pi\varkappa$, where $\varkappa$ is an integer. Accordingly, the circulation of the velocity around the vortex is equal to $2\pi\hbar\varkappa/m$. Equation (2.146) can be used to construct the wave function of the condensate in the trap in the presence of vortices (note that it was the study of vortices in a rarefied Bose gas that was the initial goal of [72, 73]).

Consider a vortex line coinciding with the axis of symmetry of the trap z. The wave function can be searched in the form:

$$\psi(\mathbf{r}) = \sqrt{n(r_\perp, z)}e^{i\varkappa\phi}, \tag{2.149}$$

where $r_\perp^2 = x^2 + y^2$, ϕ is an angle int the (x, y) plane. This function corresponds to the vortex that possesses angular velocity

$$v = \frac{\hbar\varkappa}{mr_\perp}. \tag{2.150}$$

Equation (2.146) for the wave function of the form (2.150) was solved in [74]. Figure 2.5 shows the calculation results for a vortex with $\varkappa = 1$ in a trap with the parameters of [75]. It is seen that the vortex pushes atoms out of the vicinity of the axis, so that the density distribution turns out to be toroidal.

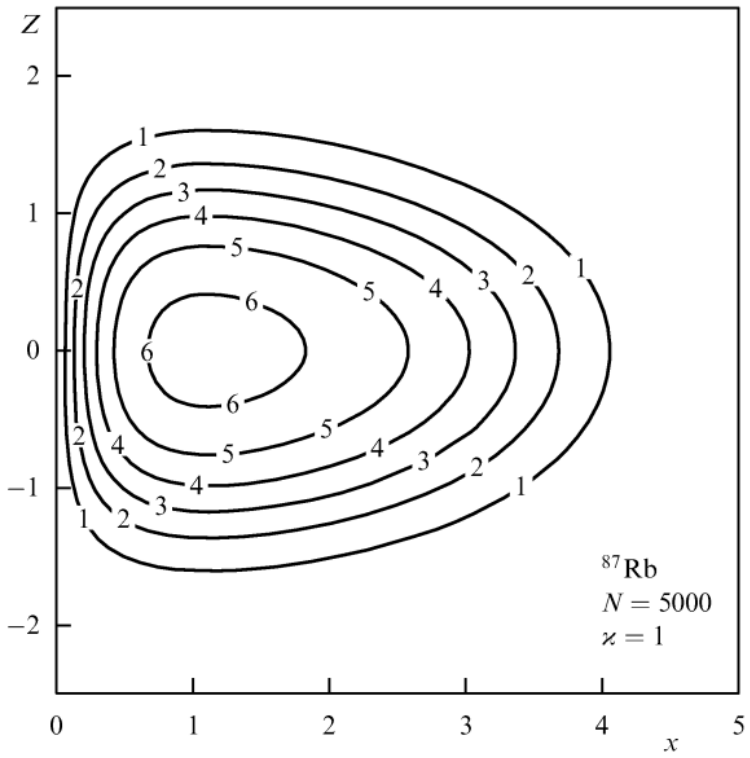

Figure 2.5: Wave function modulus of 5000 atoms ^{87}Rb of vortex with $\varkappa = 1$. Unit of length is $a = \sqrt{\hbar/m\omega_\perp}$. x and z axes represent x and z coordinates respectively. This figure has been taken from the work from Lev P. Pitaevskii, Bose-Einstein condensation in magnetic traps. Introduction to the theory, Uspekhi Fizicheskih Nauk 168 nr.6, (1998): 641-653. [71]

Chapter 3

The phase diagram and vortex properties of $\mathcal{PT}$-symmetric non-Hermitian two-component superfluid

On the condensed matter side, the many-condensate systems possess richer dynamics than their one-condensate counterparts. For example, the standard classification of superconductivity into types I and II fails to describe the phases of multiband condensates so that a proposal to adopt a new terminology, type-1.5 superconductivity, appeared in the theoretical community [76]. Experimentally, the existence of the type-1.5 superconductivity has been demonstrated shortly afterwards [77]. The semi-Meissner state of a type-1.5 superconductor demonstrates non-pairwise interaction between the vortices which leads to the formation of a multitude of complicated vortex states [78]. We discuss the non-Hermitian extension of the two-component model possessing a global, rather than local, continuous symmetry, appropriate for the two-component superfluidity. We concentrate on the stability of the ground state, the fate of the $\mathcal{PT}$ symmetry in the interacting model, and the properties of the vortex configurations. In a different context, the vortices in the weakly interacting superfluid Bose-Einstein condensates with complex-valued $\mathcal{PT}$-symmetric potentials have been investigated in Ref. [79]. As for the realistic model, one could expect the model can apply to the non-Hermitian version of two-component Bose-Einstein condensates in different hyperfine spin states similarly to the Hermitian analogues [80].

3.1 (Non-)Hermitian scalar theory

3.1.1 Lagrangians

We consider the simplest example of a scalar non-Hermitian theory. Its degrees of freedom should possess $\mathcal{P}$ and $\mathcal{T}$ transformations under which the Hamiltonian stays invariant. It means that the simplest scalar field theory should contain two complex scalar fields ϕ_1 and ϕ_2 coupled by a mass matrix M that will provide non-Hermiticity. For convenience, these two fields can be grouped into the single doublet field,

$$\Phi = \begin{pmatrix} \phi_1 \\ \phi_2 \end{pmatrix} . \tag{3.1}$$

The Lagrangian of the theory [58],

$$\mathcal{L} \;=\; \partial_\mu \Phi^\dagger \partial^\mu \Phi - \Phi^\dagger \hat{M}^2 \Phi - V(\Phi), \tag{3.2}$$

includes the classical Hermitian self-interaction potential for the scalar fields:

$$V(\Phi) \equiv V(\phi_1, \phi_2) = \lambda_1 |\phi_1|^4 + \lambda_2 |\phi_2|^4 . \tag{3.3}$$

The Lagrangian describes two types of spin-0 bosons with masses $m_{1,2}$ which interact attractively with itself with a coupling constant $\lambda_{1,2}$ and with each other via mass matrix. We consider a attractive selfinteraction $\lambda_{1,2} \geq 0$ for which the potential is bounded from below, otherwise, the system would be unstable. It represents two relativistic superfluids that interact with each other via the off-diagonal non-Hermitian coupling. We consider the potential (3.3) in the form which explicitly breaks the $U(2)$ symmetry, $\Phi \to \Omega\Phi$ with the 2×2 matrix $\Omega \in U(2)$, down to its Cartan $[U(1)]^2$ subgroup since the $U(2)$ group is explicitly broken by the mass matrix (3.4) anyway provided $\hat{M}^2_{\rm NH} \not\propto \mathbb{1}$.

Hermiticity of this theory depends on relative sign of the off-diagonal elements of mass matrix $\hat{M}^2$ of the Lagrangian (3.2). Opposite signs of nonzero value of $m_5^2 \neq 0$ correspond to non-Hermitian theory:

$$\hat{M}^2 = \hat{M}^2_{\rm NH} = \begin{pmatrix} m_1^2 & m_5^2 \\ -m_5^2 & m_2^2 \end{pmatrix} , \tag{3.4}$$

To see how the non-Hermiticity enters the theory, it is instructive to write the Lagrangian in terms of the individual fields ϕ_1 and ϕ_2:

$$\mathcal{L}_{\rm NH} = \partial_\nu \phi_1^* \partial^\nu \phi_1 + \partial_\nu \phi_2^* \partial^\nu \phi_2 - m_1^2 |\phi_1|^2 - m_2^2 |\phi_2|^2 - m_5^2 (\phi_1^* \phi_2 - \phi_2^* \phi_1) - \lambda_1 |\phi_1|^4 - \lambda_2 |\phi_2|^4 . \tag{3.5}$$

The first term of the second line in Eq. (3.5) takes a purely complex value: $-2im_5^2 \,\mathrm{Im}\,(\phi_1^* \phi_2)$ if the off-diagonal component of the mass matrix (3.4) is a real-valued nonzero quantity.

The complex valuedness of the Lagrangian (3.5) is consistent with the non-Hermiticity of the mass matrix in Eq. (3.2): $\hat{M}^{2,\dagger}_{\rm NH} \neq \hat{M}^{2}_{\rm NH}$. The off-diagonal mass with $m_5^2 \neq 0$ sets up the non-Hermitian regime in (3.4), while the point $m_5^2 = 0$ corresponds to a Hermitian theory (with $\hat{M}^{2,\dagger}_{\rm NH} = \hat{M}^{2}_{\rm NH}$) which describes two non-interacting scalar fields ϕ_1 and ϕ_2.

In order to highlight the features of non-Hermiticity, we briefly discuss the Hermitian version of the model with the following mass matrix in the Lagrangian (3.2):

$$\hat{M}^2_{\rm H} = \begin{pmatrix} m_1^2 & m_5^2 \\ m_5^2 & m_2^2 \end{pmatrix}. \tag{3.6}$$

Notice that $\hat{M}^{2,\dagger}_{\rm H} = \hat{M}^{2}_{\rm H}$ as expected and the Hermitian Lagrangian is a real-valued expression for all values of the parameter m_5:

$$\mathcal{L}_{\rm H} = \partial_\nu \phi_1^* \partial^\nu \phi_1 + \partial_\nu \phi_2^* \partial^\nu \phi_2 - m_1^2 |\phi_1|^2 - m_2^2 |\phi_2|^2 - m_5^2 (\phi_1^* \phi_2 + \phi_2^* \phi_1) - \lambda_1 |\phi_1|^4 - \lambda_2 |\phi_2|^4 . \tag{3.7}$$

The Hermitian counterpart (3.7) of the non-Hermitian system (3.5) has some parallels with effective models of the QCD strings in high-density quark matter, relevant to the physics of neutron stars, and the global cosmological strings, which reveal itself in the cosmological context [81, 82].

Below, we will consider the classical equations of motion concentrating on the non-Hermitian theory described by Lagrangian (3.2). While we work with the classical solutions, we would like to notice that on the quantum level, the non-Hermiticity propagates into the loops of perturbation theory. The quantum corrections could, therefore, induce a complex term in the interaction potential (3.3) and literally complexify the phase diagram of the theory. Leaving aside the quantum corrections, which were discussed in Ref. [49], in our work we concentrate on classical properties of the Lagrangian (3.2) and compare it with the classical properties of its Hermitian counterpart (3.7).

3.1.2 Symmetries

We consider the non-degenerate model (3.2) with a nonzero off-diagonal mass $m_5 \neq 0$ which possesses a couple of continuous and discrete symmetries. Both Hermitian and non-Hermitian versions of the model are invariant under the global U(1) transformation

$$U(1): \qquad \Phi(t, \boldsymbol{x}) \to \Phi'(t, \boldsymbol{x}) = e^{i\omega} \Phi(t, \boldsymbol{x}), \tag{3.8}$$

in which the single phase factor (with a real-valued parameter ω) is shared by both complex scalar fields ϕ_1 and ϕ_2. If $m_5 = 0$, both components of the doublet field Φ can be transformed independently so that the symmetry is enlarged to the global $[\mathrm{U}(1)]^2$. We do not consider this trivial case.

The non-Hermitian theory (3.4) is also invariant under a discrete transformation corresponding to the product of the parity inversion $\mathcal{P}$ and the time conjugation $\mathcal{T}$ operators, respectively:

$$\text{NH}: \quad \begin{cases} \mathcal{P}: & \Phi(t,\boldsymbol{x}) \to \Phi'(t,-\boldsymbol{x}) = \sigma_3 \Phi(t,\boldsymbol{x}), \\ \mathcal{T}: & \Phi(t,\boldsymbol{x}) \to \Phi'(-t,\boldsymbol{x}) = \Phi^*(t,\boldsymbol{x}). \end{cases} \tag{3.9}$$

Due to the presence of the Pauli matrix σ_3, the upper ϕ_1 component transforms under the parity inversion $\mathcal{P}$ as a genuine scalar while the lower component ϕ_2 transforms as a pseudoscalar field.

The $\mathcal{P}$ and $\mathcal{T}$ operations whose product leaves invariant the Hermitian theory (3.6),

$$\text{H}: \quad \begin{cases} \mathcal{P}: & \Phi(t,\boldsymbol{x}) \to \Phi'(t,-\boldsymbol{x}) = \Phi(t,\boldsymbol{x}), \\ \mathcal{T}: & \Phi(t,\boldsymbol{x}) \to \Phi'(-t,\boldsymbol{x}) = \Phi^*(t,\boldsymbol{x}), \end{cases} \tag{3.10}$$

indicate that both fields ϕ_1 and ϕ_2 behave as true scalars under the parity inversion.

The model (3.2), along with its extensions, possesses interesting features of the Goldstone modes associated with the spontaneous breaking of the continuous symmetry (3.8) as well as the unusual properties of the conserved currents [51, 58, 65]. Below we consider the ground state and the vortex solutions of the model.

3.1.3 Ground states

Non-Hermitian ground state

The analysis of the ground state of the two-field model (3.2) has already been done analytically in Ref. [50] for the special case of the potential (3.3) in which one of the fields was not self-interacting ($\lambda_1 \neq 0$ and $\lambda_2 = 0$). In our work, we complement this paper with the numerical analysis of the system in which both fields experience the self-interaction, $\lambda_{1,2} \neq 0$. We show that the simple extension (or, better to say, completion) of the model makes the analysis of the phase diagram very complicated.

Let us start from the simplest case when the quartic interaction is absent:

$$\lambda_1 = \lambda_2 = 0. \tag{3.11}$$

The Hermitian (3.6) and non-Hermitian (3.4) mass-squared matrices have the following eigenvalues, respectively:

$$M^2_{\text{H},\pm} = \frac{1}{2}\left(m_1^2 + m_2^2 \pm \sqrt{\left(m_1^2 - m_2^2\right)^2 + 4m_5^4}\right), \tag{3.12a}$$

$$M^2_{\text{NH},\pm} = \frac{1}{2}\left(m_1^2 + m_2^2 \pm \sqrt{\left(m_1^2 - m_2^2\right)^2 - 4m_5^4}\right). \tag{3.12b}$$

The vaccua in these models are stable provided the eigenmasses have no imaginary

parts. For the Hermitian model with the mass matrix (3.6), this requirement implies $M^2_{\mathrm{H},-} \geqslant 0$ or, naturally,

$$\mathrm{H}: \quad \begin{cases} m_1^2 + m_2^2 > 0, \\ m_1^2 m_2^2 - m_5^4 \geqslant 0. \end{cases} \tag{3.13}$$

These equations determine the region in the parameter space where the instability due to a negative mode (or modes) at the trivial minimum,

$$\phi_1 = \phi_2 = 0, \tag{3.14}$$

does not occur. In an interacting theory with $\lambda_{1,2} \neq 0$, this instability corresponds to the spontaneous symmetry breaking.

In the non-Hermitian model (3.4), the spectrum of the free (i.e., with $\lambda_1 = \lambda_2 = 0$) theory does not contain complex energy eigenvalues provided

$$\mathrm{NH}: \quad \begin{cases} m_1^2 + m_2^2 > 0, \\ m_1^2 m_2^2 + m_5^4 \geqslant 0, \\ \left(m_1^2 - m_2^2\right)^2 - 4m_5^4 \geqslant 0, \end{cases} \tag{3.15}$$

where we also took into account a possibility that the squared masses m_1^2 and m_2^2 can take negative values. The first two requirements in Eq. (3.15) correspond to the instability related to the spontaneous symmetry breaking rather than to the non-Hermiticity of the model. The last condition in Eq. (3.15) highlights the region of the parameter space where the $\mathcal{PT}$ symmetry is said to be unbroken [51, 58, 65]. Together, these conditions guarantee the stability of the ground state.

The classical equations of motion of the model (3.2) are obtained by the variation of the Lagrangian (3.5) with respect to the independent fields ϕ_1^* and ϕ_2^*, respectively:

$$\Box\phi_1 + m_1^2\phi_1 + m_5^2\phi_2 + \frac{\partial V}{\partial \phi_1^*} = 0\,, \tag{3.16a}$$

$$\Box\phi_2 + m_2^2\phi_2 - m_5^2\phi_1 + \frac{\partial V}{\partial \phi_2^*} = 0\,. \tag{3.16b}$$

A variation with respect to the fields ϕ_1 and ϕ_2 gives us an inequivalent set of equations:

$$\Box\phi_1^* + m_1^2\phi_1^* - m_5^2\phi_2^* + \frac{\partial V}{\partial \phi_1} = 0\,, \tag{3.17a}$$

$$\Box\phi_2^* + m_2^2\phi_2^* + m_5^2\phi_1^* + \frac{\partial V}{\partial \phi_2} = 0\,, \tag{3.17b}$$

which differs from Eq. (3.16) by the sign flip of the off-diagonal mass term, $m_5^2 \to -m_5^2$.

The striking inconsistency of the two pairs of equations of motion, (3.16) and (3.17), poses the natural question of how to treat this non-Hermitian system at the classical level. One of the earlier proposals [58] suggests to use only one set of equations of motion, either (3.16) or (3.17), and omit the complementary set. Indeed, the choice of the set flips the sign of the off-diagonal mass, $m_5^2 \to -m_5^2$, which affect the physical spectrum neither in free model (3.12) nor in the interacting model, as we will see below. Moreover, the non-Hermitian system must be open via coupling to an external source which equilibrates non-vanishing surface terms in the variation of the action. When the off-diagonal mass vanishes, the system becomes Hermitian, and the single set of equations is enough to describe the solutions consistently.

The next proposal was to resolve the apparent problem with the inconsistency of the classical equations of motion was put forward in Ref. [65] where a similarity transformation for the action has been used to achieve harmony between the two sets of equations of motion. This elegant idea initially required an extension of the field space using two complex components (with four degrees of freedom) for every original complex field (which hosts two degrees of freedom).

The same mapping strategy has later been adapted and extended to many-field theories in Ref. [51] where two real-valued fields were used to represent one complex field. However, this procedure, used for the mapping of the non-Hermitian theory to the Hermitian one via the similarity transformation, leads to the appearance of a negative kinetic energy term for one of the fields. While it was argued that this artefact does not change the signature of the appropriate Hilbert space [65], the appearance of the negative kinetic action leads to a negative contribution to the energy-momentum tensor so that the energy of a classical configuration (which is not necessarily a classical solution) would become unbounded from below. This pseudo-Hermitian method can be adapted, in specifying the appropriate physical regions, to give the classical solutions for non-Abelian monopoles in a spontaneously broken theory [52] (we refer the Reader to Refs. [67, 68] for complementary discussions of a non-Hermitian non-Abelian gauge theory).

In our work we follow the approach of Ref. [58] where only one set of equations of motion – either (3.16) or (3.17), but not the both of them – is considered.

While this approach may seem restrictive, it still gives the complete description of classical and quantized theories [12]. In addition to the invariance of the physical solutions with respect to the flip $m_5^2 \to -m_5^2$, the choice of the equations of motion coincides with the choice of the Hamiltonian operator in the quantum theory since both $\hat{H}(m_5^2)$ and $\hat{H}^\dagger(m_5^2) = \hat{H}(-m_5^2)$ can be used to promote the time evolution of the system. Moreover, the choice does not affect the non-Hermitian physics: the $\pm m_5^2$ versions of the classical equations of motion give the physically equivalent classical solutions of the theory and, in parallel, both original and Hermitian-conjugated Hamiltonians

determine the very same evolution of the quantum theory [12].

The classical non-Hermitian theory becomes self-consistent if one supplements the Hermitian conjugation with the subsequent $\mathcal{PT}$ symmetric operation. Then the complex conjugation along with the $\mathcal{PT}$ flip $m_5^2 \to -m_5^2$ leaves the classical equations intact [12]. The new combined operation is also important at the quantum level since the Hermitian-conjugated conversion between the bra and ket states should now be supplemented by the additional $\mathcal{PT}$ invariance operation in order to maintain the orthonormality of the eigenvectors of the non-Hermitian Hamiltonian [58]. Thus, the would-be apparent non-equivalence of the original (3.16) and conjugated (3.17) equations does not lead to an inconsistency of the non-Hermitian theory. It gives the opposite: both formulations are consistent with each other and lead to the same result both at classical and quantum levels.

At a certain stage, we use a numerical method to find the classical solutions using the criteria of the energy minimization as a selection principle of the right, "minimal energy" solution among all other available solutions. In our approach, the energy of the classical configuration in the non-Hermitian theory is bounded from below so that the numerical approach is self-consistent in finding the correct configuration. If we would otherwise employ the pseudo-Hermitian procedure of mapping the non-Hermitian theory to the Hermitian one, then the classical energy becomes unbounded due to the negative sign in the kinetic terms, and the numerical procedure fails to converge to a reasonable solution.

In the ground state the condensates are coordinate-independent quantities, and Eqs. (3.16) reduce to the non-linear algebraic relations:

$$m_1^2\phi_1 + m_5^2\phi_2 + 2\lambda_1\phi_1^2\phi_1^* = 0\,, \tag{3.18a}$$

$$m_2^2\phi_2 - m_5^2\phi_1 + 2\lambda_2\phi_2^2\phi_2^* = 0\,. \tag{3.18b}$$

The use of the complementary set of equations (3.17) instead of Eqs. (3.16) would lead to an equivalent physical solutions. Indeed, the swap of equations leads to the sign flip in Eq. (3.18) which corresponds to a simple swap of the fields ϕ_1 and ϕ_2.

It is convenient to represent the fields ϕ_a in the radial form

$$\phi_a = v_a e^{i\theta_a} \tag{3.19}$$

for $a = 1, 2$. Equations (3.18) can possess nontrivial solutions provided the phases θ_a satisfy one of the following relations:

$$\theta_1 = \theta_2, \qquad \theta_1 = \theta_2 + \pi\,. \tag{3.20}$$

One can cover both these cases assuming $\theta_1 = \theta_2$ and, simultaneously, allowing the amplitudes v_a to take both positive and negative values, $v_a \in \mathbb{R}$. The classical equa-

tions (3.18) then determine the amplitudes:

$$m_1^2 v_1 + m_5^2 v_2 + 2\lambda_1 v_1^3 = 0\,, \tag{3.21a}$$

$$m_2^2 v_2 - m_5^2 v_1 + 2\lambda_2 v_2^3 = 0\,. \tag{3.21b}$$

The canonical energy-momentum of the model (3.2) can be calculated by endowing the model with the gravitational background $g_{\mu\nu}$, considering the variation of the theory action, $S = \int d^4\mathcal{L}$ with respect to the metric,

$$T^{\mu\nu} = -\frac{2}{\sqrt{-g}}\frac{\delta S}{\delta g_{\mu\nu}(x)}\,, \tag{3.22}$$

and then setting the metric to its Minkowski values back again,

$$g_{\mu\nu} \to \eta_{\mu\nu} \equiv \mathrm{diag}(+1,-1,-1,-1). \tag{3.23}$$

The energy density of the model (3.5) is given by the $\mu = \nu = 0$ component of the energy-momentum tensor (3.22):

$$\begin{aligned} T^{00} &= \partial_0\phi_1^*\partial_0\phi_1 + \boldsymbol{\nabla}\phi_1^*\boldsymbol{\nabla}\phi_1 + \partial_0\phi_2^*\partial_0\phi_2 + \boldsymbol{\nabla}\phi_2^*\boldsymbol{\nabla}\phi_2 \\ &\quad + m_1^2|\phi_1|^2 + m_2^2|\phi_2|^2 + m_5^2(\phi_1^*\phi_2 - \phi_2^*\phi_1) + \lambda_1|\phi_1|^4 + \lambda_2|\phi_2|^4\,. \end{aligned} \tag{3.24}$$

One gets the following simple expression for the energy density of a uniform time-independent (ground) state:

$$E_{\mathrm{NH},0} \equiv T^{00} = m_1^2 v_1^2 + m_2^2 v_2^2 + \lambda_1 v_1^4 + \lambda_2 \phi_2^4\,. \tag{3.25}$$

Both solutions (3.20) for the phases $\theta_a \equiv \arg\phi_a$ of the condensates ϕ_a lead to the vanishing non-Hermitian term

$$\delta\mathcal{L}_{\mathrm{NH}} = -2im_5^2\,\mathrm{Im}\,(\phi_1^*\phi_2) \equiv -2im_5^2 v_1 v_2 \sin(\theta_1 - \theta_2) \tag{3.26}$$

in the energy density (3.25). Thus, the inconvenient imaginary terms do not enter the ground state of the model (we will see below that any solution of the single set of the classical equations of motion (3.16) has a real-valued energy density). However, despite the non-Hermitian mass m_5 not explicitly appearing in the vacuum energy (3.25), it affects the ground state indirectly via the solutions of the equations of motion (3.21).

Hermitian ground state

The equations of motion of the Hermitian model (3.7) take the following form:

$$\Box\phi_1 + m_1^2\phi_1 + m_5^2\phi_2 + \frac{\partial V}{\partial\phi_1^*} = 0\,, \tag{3.27a}$$

$$\Box\phi_2 + m_2^2\phi_2 + m_5^2\phi_1 + \frac{\partial V}{\partial\phi_2^*} = 0\,, \tag{3.27b}$$

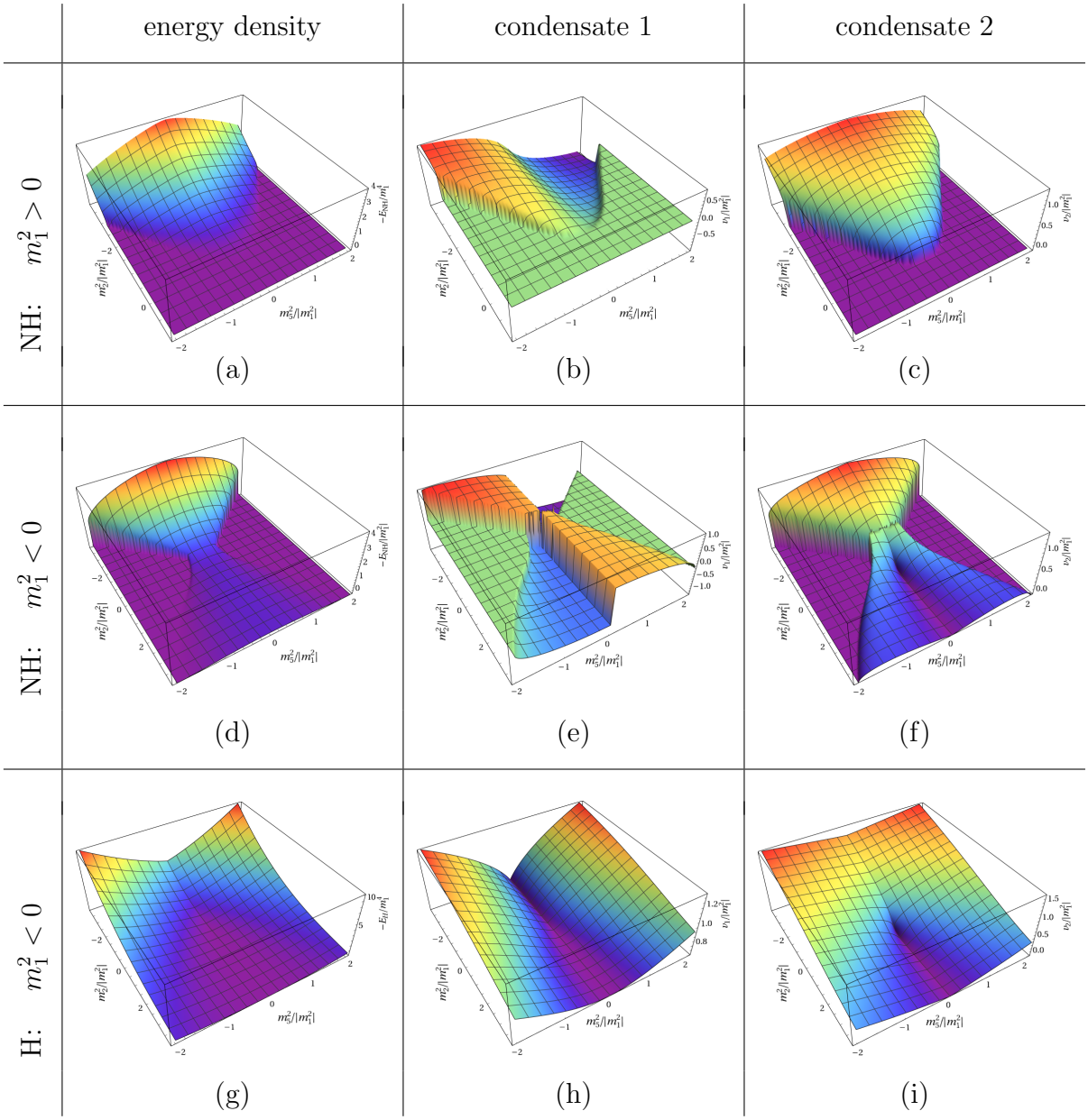

Figure 3.1: The upper panel: (a) the (minus) energy density (3.25) and the condensates (b) v_1 and (c) v_2 in the ground state of the non-Hermitian model (3.5) are shown in the plane of the mass parameter squared m_2^2 and the non-Hermitian mass squared m_5^2. The mass (squared) of the first field ϕ_1 is taken positive, $m_1^2 > 0$, and the quartic couplings for both scalar fields are fixed: $\lambda_1 = \lambda_2 = 1$. The middle panel, with the plots (d), (e) and (f), corresponds to the same quantities obtained for the negative diagonal mass $m_1^2 < 0$. The lower panel, with the plots (g), (h) and (i), depicts the Hermitian case (3.7). All dimensionful quantities are shown in the units of the absolute value of the first mass parameter, $|m_1|$. This figure has been taken from the work from A. Begun et. al, Phase diagram and vortex properties of a $\mathcal{PT}$-symmetric non-Hermitian two-component superfluid, Phys.Rev.D 104 (2021), 056024.

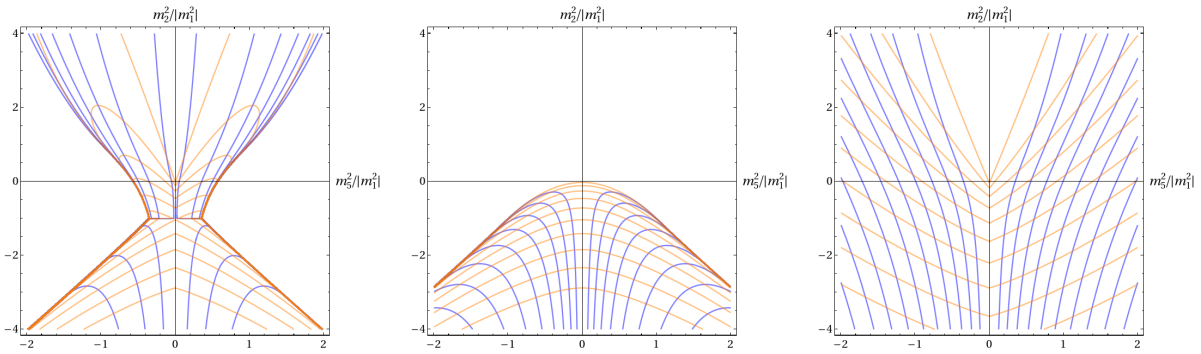

(a) (b) (c)

Figure 3.2: The contour plots of of the condensates of the non-Hermitian (panels (a) and (b)) and Hermitian (panel (c)) models. Panel (a) corresponds to the mass of first field ϕ_1 is taken negative, and (b) to taken positive.

which differ from Eq. (3.16) of the non-Hermitian model (3.5) as the both signs in front of the off-diagonal mass terms m_5^2 are the same in the Hermitian case (3.27). This small difference naturally propagates into the equations for the amplitudes in the ground state,

$$m_1^2 v_1 + m_5^2 v_2 + 2\lambda_1 v_1^3 = 0\,, \tag{3.28a}$$

$$m_2^2 v_2 + m_5^2 v_1 + 2\lambda_2 v_2^3 = 0\,, \tag{3.28b}$$

as compared to its non-Hermitian analogue (3.21). However, in the striking dissimilarity with non-Hermitian case, the variations over the fields and their complex conjugates are obviously consistent with each other in the Hermitian model. Moreover, the energy density of the ground state of the Hermitian model,

$$E_{\text{H},0} = m_1^2 v_1^2 + m_2^2 v_2^2 + 2m_5^2 v_1 v_2 + \lambda_1 v_1^4 + \lambda_2 v_2^4\,, \tag{3.29}$$

explicitly includes the m_5^2 coupling between the amplitudes of the different condensates. We remind that this coupling does not enter the non-Hermitian energy density (3.25).

Hermitian model vs. non-Hermitian model

In the Hermitian model, a negative diagonal mass can trigger a natural spontaneous symmetry breaking of the global U(1) symmetry (3.8) which leads to a non-zero expectation value of the doublet field, $\Phi_0 \neq 0$. The runaway of the scalar field from the symmetric state is balanced by quartic (self)-interactions so that the symmetry-broken ground state of the system is stable. In an interacting model, the stability of the symmetric, $\Phi = 0$, the state is determined by Eq. (3.13).

The interacting non-Hermitian theory possesses two types of instabilities. In addition to the mentioned spontaneous symmetry breaking stipulated by the first two

relations in Eq. (3.15), the symmetric ground state can also experience the U(1) symmetry breaking which could be caused, in turn, by the broken discrete $\mathcal{PT}$ symmetry. This purely non-Hermitian effect is dictated by the third relation in Eq. (3.15), the violation of which leads to the complex mass spectrum and, consequently, to the instability. The $\mathcal{PT}$-induced instability could be well seen when both diagonal masses are positive so that the first two relations in Eq. (3.15) are satisfied. As in the purely Hermitian case, the symmetry-broken ground state of the non-Hermitian system is expected to be stabilized by the quartic (self)-interactions.

In Fig. 3.1 we compare the U(1) symmetry breaking patterns in the non-Hermitian model with $m_1^2 > 0$ (the upper panel) and $m_1^2 < 0$ (the middle panel) as well as the Hermitian model with $m_1^2 < 0$ (the lower panel). We show the total energy density E determined by Eqs. (3.25) and (3.29), and the condensates v_1 and v_2. Notice that the non-Hermitian (3.21) and Hermitian (3.28) equations on the ground state imply that the relative sign of the condensates is determined by the ground state while the overall sign is not fixed. To remove this arbitrariness, we require the condensate v_2 to be positive.

If both diagonal squared masses are positive, $m_1^2 > 0$ and $m_2^2 > 0$, and the off-diagonal mass is zero, $m_5 = 0$, then the ground state resides in the symmetric phase with vanishing condensates. As the off-diagonal mass increases in its absolute value, the theory should experience the $\mathcal{PT}$-symmetric instability and we expect the appearance of the condensates in the $(m_1^2 > 0, m_2^2 > 0)$ plane. However, this does not happen, as one can see in Figs. (3.1)(b) and (c). The presence of the "$\mathcal{PT}$-induced" condensates is forbidden by the requirement of the minimization of the energy density (3.25) as these condensates would have made the energy density positive while the trivial ground state with $v_1 = v_2 = 0$ has zero energy. This conclusion appears to be the consequence of the fact that the expression for the non-Hermitian energy density (3.25) does not contain a "compensating" m_5^2 term which is present, on the contrary, in the expression of the Hermitian energy density (3.29). Therefore, the U(1) symmetric ground state with vanishing energy is preferred over the U(1) broken state with the nonvanishing condensates. We will see below that some of these symmetric states belong to the $\mathcal{PT}$-broken phases of the interacting model and, therefore, are physically meaningless.

In the symmetry-broken phase with $m_2^2 < 0$ (while we still keep $m_1^2 > 0$), the conventional U(1) symmetry breaking does occur. The upper panel of Fig. 3.1 shows that the non-Hermitian mass influences the conventional symmetry breaking in a somewhat controversial way: at sufficiently large m_5^4, the third requirement of Eq. (3.15) is violated, the $\mathcal{PT}$ symmetry gets broken and the U(1) symmetry gets restored because the ground-state condensates v_1 and v_2 vanish. In the symmetry-broken region, the flip of the sign in the m_5^2 mass flips the sign of the v_1 condensate (we remind that we always keep the v_2 condensate non-negative).

A rather similar picture occurs when one of the diagonal mass squared is taken to be negative, $m_1^2 < 0$, as shown in the middle panel of Fig. 3.1. The spontaneous symmetry breaking occurs at both signs of the remaining mass squared, m_2^2, while the increase of the absolute value of the off-diagonal mass m_5^2 leads to the restoration of the U(1) symmetry. We would like to stress again that this particular picture is enforced by the requirement of minimization of the non-Hermitian energy density (3.25) which allows us to choose the correct ground state from the multitude of the solutions of the non-Hermitian equations of motion (3.21).

Finally, the ground state of the Hermitian two-scalar model with $m_1^2 < 0$ is shown in the lower panel of Fig. 3.1. The condensates appear almost at every point of the phase diagram except for the line $m_5 = 0$, where the condensates decouple and the v_2 condensate ceases to exist at $m_2^2 > 0$. At this semi-infinite line, the condensate v_1 takes its minimum.

Stability of the ground state and the $\mathcal{PT}$ symmetry in the non-Hermitian model

Before proceeding to the discussion of the vortex solutions, let us address the formal stability issues of the ground state. Usually, the local stability of a classical configuration is probed by expanding the scalar fields in the vicinity of the configuration,

$$\phi_a = v_a + \hat{\phi}_a \tag{3.30}$$

with $|\hat{\phi}_a| \ll |v_a|$. The configuration is unstable if the fluctuation matrix corresponding to the variation of the action with respect to the fluctuation of the fields contains negative modes.

In the Hermitian theory, the global minimum in the total energy of the solution corresponds to an absolutely stable state. In the non-Hermitian theory, this criterion may not work since even in the classical theory, the ground state is determined by a single set of classical equations of motion out of the existing two sets. Therefore, mathematically, one could expect the emergence of negative directions in the space of fields. This expectation is coherent with our physical intuition since the non-Hermitian system resides in the steady-state which is generally not a thermodynamic equilibrium. In the remaining part of this section, we argue that the formal stability criteria can still be applied to the interacting non-Hermitian systems. These criteria give us the generalization of the $\mathcal{PT}$-symmetric and $\mathcal{PT}$-broken regions for the interacting theory.

From the classical equations of motion (3.18), we obtain that the field fluctuations

around the condensates are governed by the following equation:

$$\Box \begin{pmatrix} \hat{\phi}_1 \\ \hat{\phi}_1^* \\ \hat{\phi}_2 \\ \hat{\phi}_2^* \end{pmatrix} + \mathcal{M}^2 \begin{pmatrix} \hat{\phi}_1 \\ \hat{\phi}_1^* \\ \hat{\phi}_2 \\ \hat{\phi}_2^* \end{pmatrix} = 0, \tag{3.31}$$

where the fluctuation matrix $\mathcal{M}^2_{\text{NH}}$ of the non-Hermitian model is as follows:

$$\mathcal{M}^2_{\text{NH}} = \begin{pmatrix} 4\lambda_1 v_1^2 + m_1^2 & 2v_1^2\lambda_1 & m_5^2 & 0 \\ 2v_1^2\lambda_1 & 4\lambda_1 v_1^2 + m_1^2 & 0 & m_5^2 \\ -m_5^2 & 0 & 4\lambda_2 v_2^2 + m_2^2 & 2v_2^2\lambda_2 \\ 0 & -m_5^2 & 2v_2^2\lambda_2 & 4\lambda_2 v_2^2 + m_2^2 \end{pmatrix}.$$

In the U(1) broken phase, this matrix has one zero eigenvalue which corresponds to the Goldstone mode. In the symmetric U(1) phase, all eigenvalues are generally nonzero.

For the ground state to be stable, one expects that all eigenvalues of the fluctuation matrix are non-negative. In the non-Hermitian model, this requirement is not always satisfied. In Fig. 3.4 we show the (in)stability phases for various quartic couplings λ_1 and λ_2.

The (in)stability phase diagram has a rather curious form. One notices that the borderlines between the stable and unstable areas involve both U(1) symmetric and broken regions which possess, on the contrary, rather featureless, smooth behaviour of the condensates as shown in Fig. 3.1. In order to understand the appearance of the negative modes, let us consider any unstable point in the symmetry-restored region with masses $m_1^2 > 0$, $m_2^2 > 0$ (these regions are marked by the white colour in the upper panel of Fig. 3.4). Since both condensates are zero and both diagonal masses as well as the couplings are positive, the energy density (3.25) takes an absolute minimum. On the other hand, in these regions, the third criterion of Eq. (3.15) is not satisfied, indicating that the symmetric state resides in the $\mathcal{PT}$-broken region and is thus unstable. The instability is not captured by the minimization of the energy density (3.25) since this particular expression is derived for the classical solutions while the instability can drive the configuration out of the classical subspace of configurations. The non-classical configuration can acquire even a complex value thus invalidating the criterion of the energy minimization outside of the classical subspace of field configurations.

Thus, we arrive to the conclusion that the ground state of the non-Hermitian model is formally not stable in certain regions of the parameter space. One can easily check that these unstable regions become the $\mathcal{PT}$-broken regions when the quartic interaction couplings are set to zero, $\lambda_{1,2} \to 0$. Therefore, similarly to the free non-interacting model, the unstable regions indicated in Fig. 3.4 can be interpreted as the $\mathcal{PT}$-broken regions in the interacting case where the model cannot be used as an invalid prescription

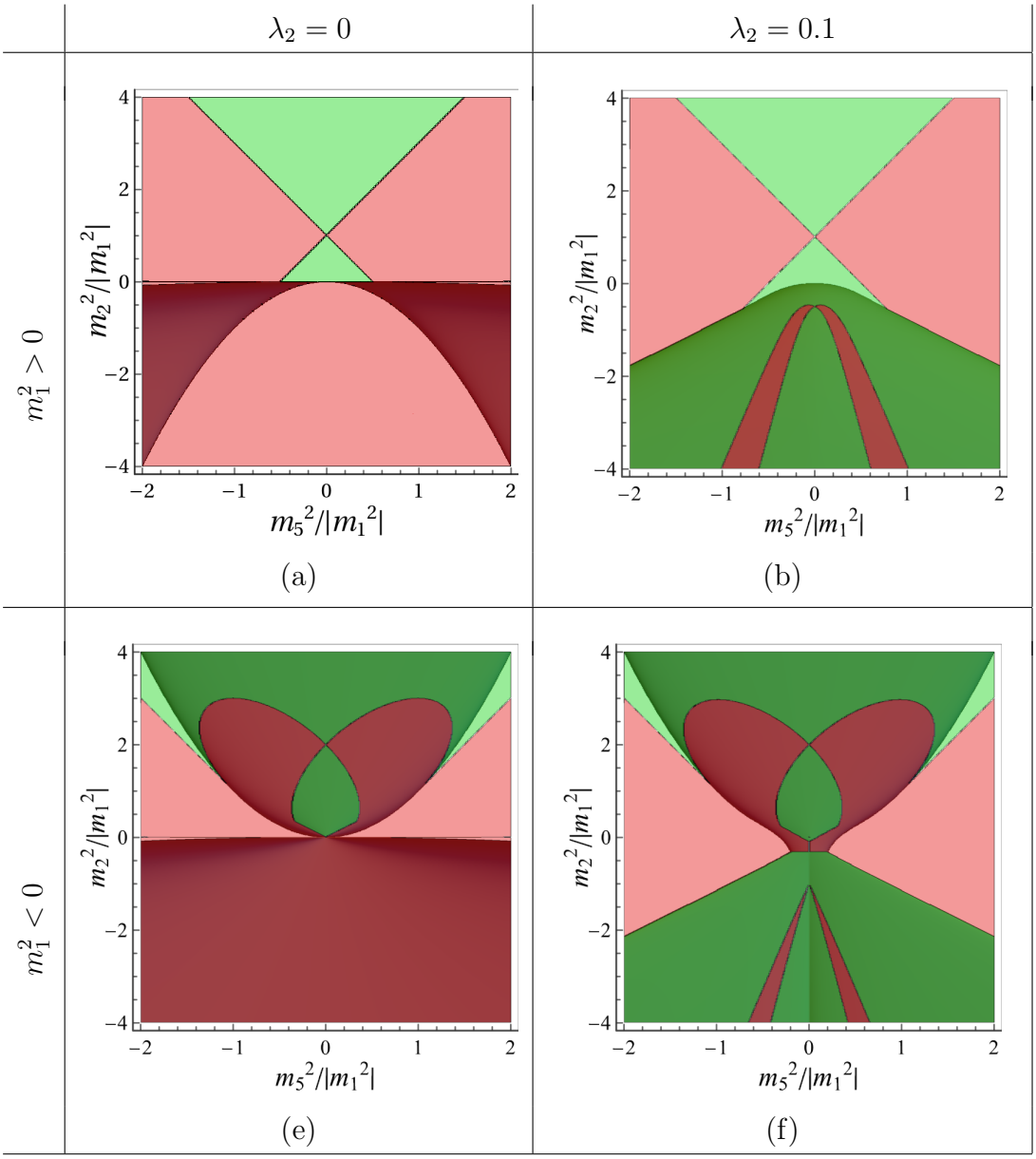

Figure 3.3: The stable ($\mathcal{PT}$-symmetric, marked by the green colour) region and the unstable (spontaneously $\mathcal{PT}$-broken, marked by the red colour) regions in the interacting non-Hermitian theory in the (m_5^2, m_2^2) plane. The mass squared of the first scalar field takes positive values ($m_1^2 > 0$) at the upper panel and negative values ($m_1^2 < 0$) at the lower panel. The dark green and light green colours denote regions with stable $\mathcal{PT}$-symmetric ground states with non-vanishing and vanishing condensates, respectively. The dark red and light red areas are unstable $\mathcal{PT}$-broken regions with, respectively, nontrivial and vanishing solutions of the classical equations of motion (3.27). This figure has been taken from the work from A. Begun et. al, Phase diagram and vortex properties of a $\mathcal{PT}$-symmetric non-Hermitian two-component superfluid, Phys.Rev.D 104 (2021), 056024.

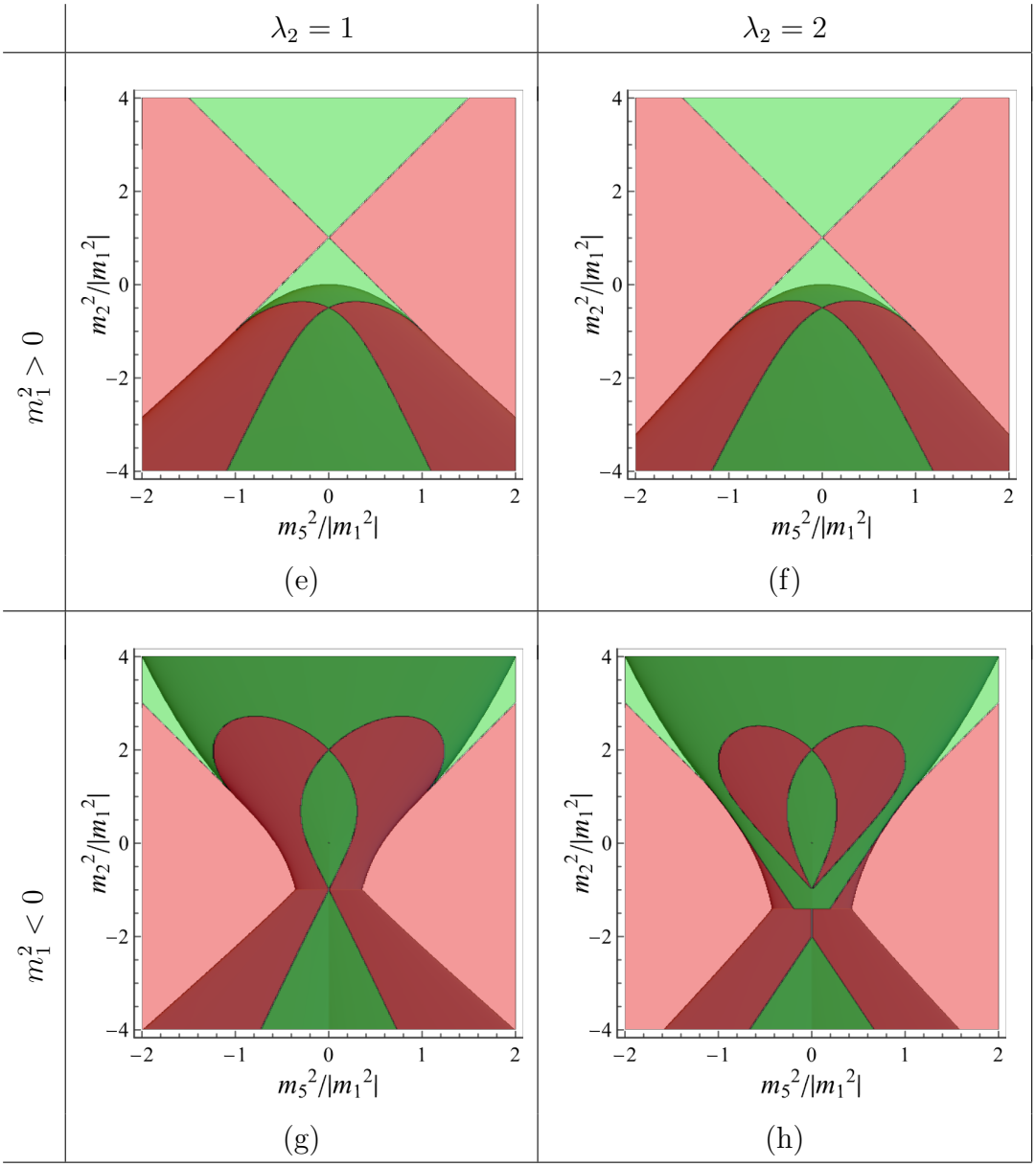

Figure 3.4: The stable ($\mathcal{PT}$-symmetric, marked by the green color) region and the unstable (spontaneously $\mathcal{PT}$-broken, marked by the red color) regions in the interacting non-Hermitian theory in the (m_5^2, m_2^2) plane. The mass squared of the first scalar field takes positive values ($m_1^2 > 0$) at the upper panel and negative values ($m_1^2 < 0$) at the lower panel. The dark green and light green colors denote regions with stable $\mathcal{PT}$-symmetric ground states with non-vanishing and vanishing condensates, respectively. The dark red and light red areas are unstable $\mathcal{PT}$-broken regions with, respectively, nontrivial and vanishing solutions of the classical equations of motion (3.27). This figure has been taken from the work from A. Begun et. al, Phase diagram and vortex properties of a $\mathcal{PT}$-symmetric non-Hermitian two-component superfluid, Phys.Rev.D 104 (2021), 056024.

of any steady-state in a physical system. The $\mathcal{PT}$-symmetric regions, on the contrary, are valid stable zones where the steady-state physics can be realized.

The stability, now associated with the $\mathcal{PT}$-symmetric regions, is thus determined by the standard requirement that the quadratic fluctuation matrix,

$$\mathcal{M}^2_{ab} = \frac{\delta^2 S_{\rm NH}[\chi]}{\delta\chi_a(x)\delta\chi_b(x)}\,, \tag{3.32}$$

does not possess negative eigenvalues. Here the vector $\chi = (\phi_1, \phi_2, \phi_1^*, \phi_2^*)$ denotes the original fields and their conjugates.

For the sake of completeness, we show the fluctuation matrix of the Hermitian model (3.7),

$$\mathcal{M}^2_{\rm H} = \begin{pmatrix} 4\lambda_1 v_1^2 + m_1^2 & 2v_1^2\lambda_1 & m_5^2 & 0 \\ 2v_1^2\lambda_1 & 4\lambda_1 v_1^2 + m_1^2 & 0 & m_5^2 \\ m_5^2 & 0 & 4\lambda_2 v_2^2 + m_2^2 & 2v_2^2\lambda_2 \\ 0 & m_5^2 & 2v_2^2\lambda_2 & 4\lambda_2 v_2^2 + m_2^2 \end{pmatrix},$$

which has only non-negative eigenmodes, as expected. The Hermitian ground state does not have any ambiguities in the stability criteria.

3.2 Vortices in fixed-length condensates

3.2.1 Vortices in one-component superfluids: brief review

In this section, we consider in the bosonic condensates with the fixed radial (amplitude) part $|\psi|$ of the scalar condensate $\psi = |\psi|e^{i\theta}$ when the entire dynamics of the system is encoded in the condensate phase θ. We can neglect the fluctuations of the amplitude in the long-range limit for fluctuations with a wavelength longer than the appropriate healing length ξ [70].

The healing length corresponds to the wavelength at which the kinetic energy of the boson equals the chemical potential. It determines the size of vortices and plays a role similar to the one played by the correlation length in the superconductivity. On the superconductivity side, a condensate with a fixed amplitude appears naturally in the London limit which corresponds to the extreme type-II superconducting regime. In the London limit, the penetration depth of the magnetic field is much longer than the correlation length so that the latter can be neglected in many physical situations. Equivalently, this limit poses a constraint on the modulus of the superconducting condensate which can be considered as a rigidly fixed, non-fluctuating quantity. The gauge invariance implies that the phase of the superconducting condensate is not constrained by this limit, thus sharing an analogy with a superfluid. However, the phase is absorbed

by the electromagnetic gauge field, which becomes – consistent with the Meissner effect – a massive vector field via the Anderson-Higgs mechanism. [83]

In the background of the sufficiently strong magnetic field, the type-II superconductors enter the mixed (Abrikosov) phase where the magnetic flux penetrates the condensate in a form of parallel vortices which form the regular Abrikosov lattice. In the London limit, the vortex is characterized by a singularity in the phase of the condensate which reflects itself in a singular behaviour of the gauge field close to the vortex core. [84]

In our work, we consider the model with the global, rather than local/gauge, U(1) symmetry. In the global case, the condensate is associated with the electrically neutral complex scalar field which corresponds to the phenomenon of superfluidity rather than superconductivity. The Anderson-Higgs mechanism is evidently absent and the massless mode in the phase of the condensate appears to be the Goldstone boson associated with the global U(1) symmetry breaking. In the case of a non-relativistic Bose gas, one identifies the Goldstone mode with a phonon. Instead of the Abrikosov strings with magnetic flux, the superfluid condensates host the vortices characterized by singularities in the phases of the condensate. These vortices are also called the "global vortices" since they appear in theories possessing a global symmetry. Below, we will briefly review the theory of vortices for a non-relativistic one-component superfluid following Ref. [84] and then we proceed to the generalization of our approach to the long-range ("London") limit of the relativistic non-Hermitian two-field model.

Consider a superfluid condensate of a non-relativistic Bose gas of particles with the mass M. It is convenient to describe by the wave function in the radial coordinates

$$\psi = |\psi| e^{i\theta}. \tag{3.33}$$

The long-range limit corresponds to the fixed radial degree of freedom $|\psi|$ which is a good approximation at very low temperature. Then the energy of the fluctuations in the superfluid can be written in the following form (we work in units $c = \hbar = 1$):

$$E = \int d^3x \, \frac{\rho_s}{2} \boldsymbol{v}_s^2 \equiv \frac{|\psi|^2}{2M} \int d^3x (\boldsymbol{\nabla}\theta)^2 \,, \tag{3.34}$$

where the radial part $|\psi|$ of the condensate determines the superfluid density

$$\rho_s = M|\psi|^2 \tag{3.35}$$

while its phase θ provides us with the velocity of the superfluid condensate,

$$\boldsymbol{v}_s = (\boldsymbol{\nabla}\theta)/M. \tag{3.36}$$

We neglected here qualitatively inessential contributions coming from the inhomogeneity of the radial part of the condensate. An extremization of the energy (3.34) gives

us the Poisson's wave equation, $\Delta\theta = 0$ which corresponds to the incomprehensibility condition of the superfluid,

$$\boldsymbol{\nabla} \cdot \boldsymbol{v}_s = 0. \tag{3.37}$$

The superfluid theory (3.34) also incorporates singular configurations of the vortex fluid which correspond to the superfluid currents that wind around a line (called the vortex line) in three-dimensional space. Precisely at the vortex line, the superfluid condensate vanishes, $\phi = 0$, while the phase of the superfluid condensate is equal – in the vicinity to the vortex core – to a geometrical angle (times an integer) in the plane transverse to the vortex line. The integer is a topological quantity that characterizes the vortex winding number.

The vortices can be accounted in the model (3.34) despite the fact that this model describes a long-range macroscopic physics with a globally uniform, constant condensate. Consider, for simplicity, a straight static vortex line along the direction x_3 located at the center $x_1 = x_2 = 0$ in the transverse plane. The phase of the vortex is

$$\theta(x_1, x_2) = n\varphi, \tag{3.38}$$

where n is the winding number of the vortex and

$$\varphi = \arg(x_1 + ix_2) \tag{3.39}$$

is the azimuthal angle in the two-dimensional (x_1, x_2) plane. The velocity of the superfluid,

$$\boldsymbol{v}_s = \frac{n}{M}\boldsymbol{\nabla}\arg(x_1 + ix_2) = \frac{n}{Mr}\mathbf{e}_\varphi, \tag{3.40}$$

is directed along the unit vector in the azimuthal $\mathbf{e}_\varphi$, so that the fluid "winds" around the vortex center at $x_1 = x_2 = 0$. Alternatively, the location of the vortex singularity corresponds to the point in the two-dimensional plane, where the derivatives do not commute,

$$(\partial_1\partial_2 - \partial_2\partial_1)\theta(x_1, x_2) = 2\pi n\delta(x_1)\delta(x_2)\,. \tag{3.41}$$

The total energy (3.34) evaluated at this static straight vortex configuration is:

$$E = L\frac{|\psi|^2 n^2}{2M}2\pi\int_\xi^R rdr\frac{1}{r^2} = L\frac{\pi|\psi|^2 n^2}{M}\ln\frac{R}{\xi}\,, \tag{3.42}$$

where L is the length of the vortex. The infrared cutoff of this integral is the size of the system R while the size ξ of the vortex core – typically, of the interatomic distance – serves as an ultraviolet cutoff. The important message of Eq. (3.42) is that the vortex energy (mass) is proportional to the length of the vortex L. One can show that the vortex curvature provides a subleading correction. The energy density per unit length is a finite quantity since the logarithmic divergence in Eq. (3.42) is very mild.

Consider now the relativistic one-component model with the action:

$$S = \int d^4x\, \partial_\mu \phi^* \partial^\mu \phi \equiv \kappa^2 \int d^4x\, \partial_\mu \theta \partial^\mu \theta\,, \tag{3.43}$$

where we adopted the long-range limit with the constant radial condensate $\kappa = |\phi|$. The variation of the action with respect to the phase θ gives us the equation for the propagation of the massless Goldstone particle, $\Box\theta = 0$, where $\Box = \partial_t^2 - \boldsymbol{\nabla}^2$ is the d'Alembert operator.

In the non-relativistic limit, the model (3.43) possesses the energy (3.34) for static vortex configurations. It is convenient to parameterize the coordinates $\tilde{x}^\mu = \tilde{x}^\mu(\sigma)$ of the two-dimensional vortex singularities by the two component vector $\sigma = (\sigma_1, \sigma_2)$. We split the phase θ into the regular and singular parts, $\theta = \theta^r + \theta^s$. The regular part θ^r of the phase corresponds to the perturbative fluctuations while the singular part θ^s encodes the position of the vortex (3.41). In the relativistic notations,

$$\partial_{[\mu,}\partial_{\nu]}\theta^s(x,\tilde{x}) = 2\pi \cdot \frac{1}{2}\epsilon_{\mu\nu\alpha\beta}\Sigma_{\alpha\beta}(x,\tilde{x}), \tag{3.44}$$

where the singularity itself is given by the tensor current:

$$\Sigma_{\alpha\beta}(x,\tilde{x}) = \int_\Sigma d^2\sigma_{\alpha\beta}(\tilde{x})\delta^{(4)}[x - \tilde{x}(\sigma)], \tag{3.45}$$

which is expressed via the differential measure at the vortex world-sheet Σ:

$$d^2\sigma_{\alpha\beta}(\tilde{x}) = \epsilon^{ab}\frac{\partial x_\alpha}{\partial\sigma_a}\frac{\partial x_\beta}{\partial\sigma_b}d^2\sigma\,. \tag{3.46}$$

Here ϵ^{ab} is the fully anti-symmetrized tensor in two dimensions, $\epsilon^{12} = -\epsilon^{21} = +1$ and $\epsilon^{11} = \epsilon^{22} = 0$. The vortex tensor (3.45) is a two-dimensional delta-function at the surface of the vortex, with the orientation at the vortex world-sheet. For example, for a straight vortex mentioned above, one uses the parameterization $\tilde{x}_0 = \sigma_1$, $\tilde{x}_1 = \tilde{x}_2 = 0$, $\tilde{x}_3 = \sigma_2$, and obtains

$$\Sigma_{\alpha\beta}(x) = n\,(\delta_{\alpha,0}\delta_{\beta,3} - \delta_{\alpha,3}\delta_{\beta,0})\delta(x_1)\delta(x_2)\,, \tag{3.47}$$

where $n \in \mathbb{Z}$ is the vorticity. Note that the regular part of the phase does not contain any singularity by definition, $[\partial_\mu, \partial_\nu]\theta^r \equiv 0$.

Integrating out or, equivalently, solving the equations of motion for the regular component the phase, θ^r, allows us to rewrite the action (3.43) in terms of the singular part of the phase θ^s, which, in turn, depends only on the vortex world-sheet (3.45):

$$S[\Sigma] = 4\pi^2\kappa^2 \int_\Sigma d^2\sigma(\tilde{x}) \int_\Sigma d^2\sigma(\tilde{x}')D(\tilde{x} - \tilde{x}')\,. \tag{3.48}$$

This action is a nonlocal functional which features two integrals that are taken over the same vortex worldsheet. In the case of many vortices, the worldsheet Σ includes all their worldsheets: $\Sigma_{\mu\nu} = \Sigma_{1,\mu\nu} + \Sigma_{2,\mu\nu} + \ldots$.

The nonlocal action (3.48) represents the self-interaction of the vortex line as well as the interactions of the distinct vortex segments via propagation of a massless Goldstone particle between the vortex segments. In Eq. (3.48), this long-range interaction is represented by the advanced Green's function $D(x)$ of the d'Alembert operator:

$$\Box\, D(x) = -\delta^{(4)}(x)\,. \tag{3.49}$$

In the case of a static straight vortex line of large length L, the action (3.48) calculated for the time interval δt gives us $S = E\delta t$, where E is, up to parameter redefinitions, the known vortex energy (3.42). In order to demonstrate this fact, it is convenient to make a Wick transformation in the integral (3.48) to the Euclidean spacetime. In the Euclidean space, the massless propagator (3.49) is:

$$D(x) = \int \frac{d^4p}{(2\pi)^4}\frac{e^{ipx}}{p^2} = \frac{1}{8\pi^2}\frac{1}{|x|^2}\,, \tag{3.50}$$

where x is the 4-distance. For a single straight static vortex with the surface (3.47), the longitudinal (along the vortex) and temporal coordinates in the action (3.48) can be integrated out, and we get the following formal expression for the vortex energy:

$$E = 4\pi^2\kappa^2 L\, D^{(2d)}(0)\,, \tag{3.51}$$

where

$$D^{(2d)}(\rho) = -\frac{1}{2\pi}\ln\frac{\rho}{\rho_0}\,, \tag{3.52}$$

is the two-dimensional massless propagator [a solution of Eq. (3.49) in two Euclidean dimensions] as the function of the two-dimensional distance ρ. The parameter ρ_0, which has the dimension "length", is introduced for the consistency reasons. The argument "0" in Eq. (3.51) highlights the fact that the formal expression for the energy in the long-range limit is a logarithmically divergent quantity similarly to the non-relativistic expression (3.42). A more accurate derivation in a finite cylindrical box of the radius R_0 leads us to

$$E = 2\pi\kappa^2 L\log\frac{R_0}{\xi}\,, \tag{3.53}$$

where ξ is the size of the vortex core given by the healing length which does not explicitly enter the model in the long-wavelength limit.

The general expression (3.48) also gives us the interaction energy of the two straight static vortices with the vorticities n_1 and n_2 separated by the distance R:

$$V(R) = 8\pi^2\kappa^2 L D^{(2d)}(R) \equiv -4\pi n_1 n_2\kappa^2 L\log\frac{R}{\xi}. \tag{3.54}$$

The like-charged vortices repel each other while the vortices with opposite vorticities attract to each other.

Finishing this section, we notice that in order to get Eq. (3.54) it is sufficient to take in the action (3.48), instead of the single-vortex current (3.47), the following expression:

$$\Sigma_{\alpha\beta}(x) = (\delta_{\alpha,0}\delta_{\beta,3} - \delta_{\alpha,3}\delta_{\beta,0})\delta(x_1)\times[n_1\delta(x_2 - R/2) + n_2\delta(x_2 - R/2)]\,. \tag{3.55}$$

3.2.2 Two-component superfluids in long-range limit

Lagrangians in the long-range limit

The long-range limit of both Hermitian (3.7) and non-Hermitian (3.5) two-condensate models can be reached by expressing the diagonal masses

$$m_a^2 = -2\lambda_a \kappa_a^2 \tag{3.56}$$

via the condensate densities $\kappa_a^2 > 0$ and $a = 1, 2$ and then taking the limit of strong quartic interaction, $\lambda_1 = \lambda_2 \to \infty$. The parameters $\kappa_a > 0$ fix the radial amplitudes for each field,

$$\phi_a = \kappa_a e^{i\theta_a}, \tag{3.57}$$

while leaving the phases θ_a as the only dynamical variables. In the long-range limit, the Lagrangians for the Hermitian (3.7) and non-Hermitian (3.5) models reduce, respectively, to the following expressions.

$$\mathcal{L}_{\text{H}} = \kappa_1^2 \partial_\nu \theta_1 \partial^\nu \theta_1 + \kappa_2^2 \partial_\nu \theta_2 \partial^\nu \theta_2 - 2m_5^2 \kappa_1 \kappa_2 \cos(\theta_1 - \theta_2)\,, \tag{3.58}$$

$$\mathcal{L}_{\text{NH}} = \kappa_1^2 \partial_\nu \theta_1 \partial^\nu \theta_1 + \kappa_2^2 \partial_\nu \theta_2 \partial^\nu \theta_2 + 2im_5^2 \kappa_1 \kappa_2 \sin(\theta_1 - \theta_2)\,. \tag{3.59}$$

The only difference between the Hermitian and non-Hermitian cases appears in the interaction between the phases of different condensates: instead of the cosine function in the Hermitian model, its non-Hermitian model has a sine function preceded by a purely imaginary coupling.

According to the third criterion of Eq. (3.15), the non-Hermitian theory in the long-range limit at $\kappa_1 \neq \kappa_2$ would correspond to the $\mathcal{PT}$ unbroken phase if the theory were non-interacting. Below, we will see that in the interacting theory this criterion, unsurprisingly, does not work. Still, Eq. (3.59) represents a meaningful theory even if $m_5 \neq 0$.

Hermitian two-condensate model

The system described by the Hermitian Lagrangian (3.58) corresponds to a long-range description of two coupled condensates within the Gross-Pitaevskii formalism [70]. The condensates correspond to two different hyperfine spin states of (for example, of ^{87}Rb), which are driven by the Rabi frequency Ω.

In the static limit, the energy functional of the system (3.58) can be written in a suggestive non-relativistic form:

$$E[\theta_1, \theta_1] = \int d^3x \left\{ \frac{\hbar^2}{2m} \left[\rho_1 (\boldsymbol{\nabla}\theta_1)^2 + \rho_2 (\boldsymbol{\nabla}\theta_2)^2 \right] - \hbar\Omega \sqrt{\rho_1 \rho_2} \cos(\theta_1 - \theta_2) \right\}, \tag{3.60}$$

where $\rho_a \equiv 2m\kappa_a^2$ is the density of the $a = 1, 2$ condensate and the interaction term $\Omega \equiv -2m_5^2 \kappa_1 \kappa_2$ has the meaning of the Rabi frequency (here we restored for a moment the powers of $\hbar$). Below we continue to work in the notations of Eq. (3.58).

From the classical equations of motion of the Hermitian model,

$$\kappa_1 \Box\, \theta_1 - m_5^2 \kappa_2 \sin(\theta_1 - \theta_2) \;=\; 0\,, \tag{3.61}$$

$$\kappa_2 \Box\, \theta_2 + m_5^2 \kappa_1 \sin(\theta_1 - \theta_2) \;=\; 0\,, \tag{3.62}$$

one immediately determines the presence of the Goldstone massless mode

$$\chi = \theta_1 \sin^2\beta + \theta_2 \cos^2\beta\,, \tag{3.63}$$

and the massive excitation,

$$\gamma = \theta_1 - \theta_2\,. \tag{3.64}$$

These degrees of freedom satisfy, respectively, the following equations:

$$\Box\, \chi \;=\; 0\,, \tag{3.65}$$

$$\Box\, \gamma - M^2 \sin\gamma \;=\; 0\,. \tag{3.66}$$

Here

$$M^2 = \frac{2m_5^2}{\sin 2\beta} \equiv \frac{\kappa_1^2 + \kappa_2^2}{\kappa_1 \kappa_2} m_5^2\,, \tag{3.67}$$

is the mass of the mode (3.64),

$$\tan\beta = \frac{\kappa_1}{\kappa_2}\,, \tag{3.68}$$

is the angle which determines the relative strength of the condensates, and

$$\kappa^2 = \kappa_1^2 + \kappa_2^2\,, \tag{3.69}$$

is the total condensate density given by the sum of the densities of the individual components.

The mode χ corresponds to the gapless sound excitation (the density wave) while mode γ is the spin density wave which is always gapped provided the Rabi frequency is nonzero, $\Omega \neq 0$ (or, in our notations, $m_5 \neq 0$) [85].

Since $\kappa_a > 0$, the mass (3.67) can always be chosen as a positive quantity. The Hermitian Lagrangian (3.58) can therefore be rewritten as a sum of independent contributions coming from massless (3.63) and massive (3.64) fields:

$$\mathcal{L}_{\text{H}} = \kappa^2 \partial_\nu \chi \partial^\nu \chi + \mathcal{L}_{\text{H}}^{(M)}(\gamma)\,. \tag{3.70}$$

The Goldstone mode χ corresponds to the massless excitation of the one-component Bose gas superfluid (3.43). The massive mode γ is described by the sine-Gordon Lagrangian:

$$\mathcal{L}_{\text{H}}^{(M)}(\gamma) = \tilde{\kappa}^2 \left(\partial_\nu \gamma \partial^\nu \gamma - 2M^2 \cos\gamma\right)\,, \tag{3.71}$$

where the parameter

$$\tilde{\kappa} = \frac{\kappa \sin 2\beta}{2}\,, \tag{3.72}$$

plays a role of the amplitude corresponding to the massive condensate. In Eq. (3.71), the term $\cos\gamma$ appears naturally instead of the usual γ^2 mass term in agreement with the $\gamma \to \gamma + 2\pi$ periodicity coming from the symmetry of the original fields θ_1 and θ_2. It is instructive to look at the limit of a large mass, $M\xi \gg 1$, which reduces the fluctuations of the field γ and makes the last term in the model (3.71) quadratic. Then the integration over the field γ can be done explicitly taking into account the vortex singularities.

Following the analogy of the one-component model, we conclude the two-component model should contain two types of superfluid vortices associated with singularities (winding) in the phases of the fields θ_1 and θ_2. Using the decompositions (3.63) and (3.64), we identity the massless $\Sigma^{(0)}$ and massive $\Sigma^{(M)}$ combinations of the vortex worldsheets which appear as the singularities in χ and γ fields, respectively:

$$\Sigma^{(0)}_{\mu\nu} = \Sigma^{(1)}_{\mu\nu}\sin^2\beta + \Sigma^{(2)}_{\mu\nu}\cos^2\beta\,, \tag{3.73}$$

$$\Sigma^{(M)}_{\mu\nu} = \Sigma^{(1)}_{\mu\nu} - \Sigma^{(2)}_{\mu\nu}\,. \tag{3.74}$$

Here the individual phase windings are defined according to Eq. (3.44):

$$\partial_{[\mu},\partial_{\nu]}\theta^s_i(x,\tilde{x}) = 2\pi\cdot\frac{1}{2}\epsilon_{\mu\nu\alpha\beta}\Sigma^{(i)}_{\alpha\beta}(x,\tilde{x}), \quad i=1,2\,. \tag{3.75}$$

Therefore, the effective theory of vortices is written as follows:

$$\begin{aligned} S[\Sigma] = \; & 4\pi^2\kappa^2\int_{\Sigma^{(0)}} d^2\sigma(\tilde{x})\int_{\Sigma^{(0)}} d^2\sigma(\tilde{x}')D(\tilde{x}-\tilde{x}') \\ & +4\pi^2\tilde{\kappa}^2\int_{\Sigma^{(M)}} d^2\sigma(\tilde{x})\int_{\Sigma^{(M)}} d^2\sigma(\tilde{x}')D_M(\tilde{x}-\tilde{x}')\,. \end{aligned} \tag{3.76}$$

where $D_M(x)$ is the advanced Green's function corresponding to the propagator of the massive particle,

$$(\Box + M^2)\, D_M(x) = -\delta^{(4)}(x). \tag{3.77}$$

Despite its cumbersome appearance, the physical sense of the effective action (3.76) is relatively transparent: the vortex worldsheets interact with each other via the massless density waves and the massive spin-wave exchanges in the combinations $\Sigma^{(0)}$ and $\Sigma^{(M)}$. The interaction is given by combining the attractive long-range (Coulomb-like) potential and the short-range (Yukawa) interaction with the strength determined by the couplings κ and $\tilde{\kappa}$, and the angle β which determines the relative strength of the condensates.

Let us consider what the consequence of the action (3.76) for two static parallel straight vortices of the length $L \ll \xi$ is. The Coulomb interaction of the first term

in Eq. (3.76) is given by the long-range logarithmic potential (3.54). The short-range part which appears in the second term of Eq. (3.76) corresponds to the interaction (we neglect the energy of the single vortex):

$$V_M(R) = -4\pi n_1 n_2 \kappa^2 L K_0 \left(\frac{R}{\xi}\right). \tag{3.78}$$

where K_0 is the modified Bessel function of the second kind. In the limit of zero Rabi frequency, $\Omega = 0$, the coupling between the vortices in different condensates disappears, $m_5 = 0$, the mass (3.67) vanishes, and the massive spin-wave exchange (3.78) takes the logarithmic form (3.54). However, since the action (3.76) is derived in the limit of the massive spin-wave, $M\xi \ll 1$, the last term leads only to the short-range interactions. The logarithmic potential dominates the large-distance physics leading to the following potential between the vortices of the kinds $a, b = 1, 2$:

$$V_{ab}(R) = -4\pi n_a n_b \alpha_a \alpha_b \kappa^2 L \log\left(\frac{|\boldsymbol{x}_a - \boldsymbol{x}_b|}{\xi}\right), \tag{3.79}$$

where $\alpha_1 = \sin^2\beta$ and $\alpha_2 = \cos^2\beta$ gives the amplitudes of, respectively, the fields θ_1 and θ_2 in the massless density wave (3.63). The expression (3.79) is a trivial generalization of the vortex-vortex interaction in the case of a single condensate (3.54).

The two-component model possesses, however, a new object, the domain wall in the scalar condensates. [85, 86] This nontrivial topological structure has no analogue in the one-component model. Technically, its appearance can be seen from the last (cosine) term in the two-field Lagrangian (3.58) which leads to a soliton in the massive field γ, Eq. (3.64). The domain wall appears due to the coupling m_5, which, as we mentioned, corresponds to the Rabi frequency Ω that couples the two spin states. The field γ changes by 2π across the vortex, which guarantees the topological stability of the wall within the model (3.58).

The boundary of a domain wall is necessarily a vortex that carries an integer winding number. Since the domain wall possesses a nonzero tension, the vortex cannot exist as an isolated object because it would otherwise have infinite energy due to the wall attached. Therefore, the vortices from different condensates are bound by a linear potential because the domain wall possesses a constant energy per unit area. Such bounded vortex pairs are sometimes called merons [80].

According to equation (3.60), one can find the domain wall solution is a local minimum of the energy. To do that one needs to vary equation (3.60). As the result we get

$$\frac{\hbar^2}{m}\rho_1 \Box\theta_1 - \hbar\Omega\sqrt{\rho_1\rho_2}\sin(\theta_1 - \theta_2) = 0, \tag{3.80}$$

$$\frac{\hbar^2}{m}\rho_2 \Box\theta_2 + \hbar\Omega\sqrt{\rho_1\rho_2}\sin(\theta_1 - \theta_2) = 0, \tag{3.81}$$

Fields θ_1 and θ_2 are functions of coordinate $\theta_{1,2} = \theta_{1,2}(x)$ and at large enough x should rich constant values. Applying this condition find a nontrivial solution of (3.81)

$$\theta_1 = \frac{\rho_2}{\rho}\theta_A, \tag{3.82}$$

$$\theta_2 = -\frac{\rho_1}{\rho}\theta_A, \tag{3.83}$$

where

$$\theta_A = 4\arctan e^{kx}, \tag{3.84}$$

$$k^2 = \frac{m\omega}{\hbar}\frac{\rho}{\sqrt{\rho_1\rho_2}}. \tag{3.85}$$

$\theta_A = \theta_1 - \theta_2$ is the relative phase, it changes from 0 to 2π. The tension of the domain wall is

$$\sigma = 8\frac{\hbar^{\frac{3}{2}}\Omega^{\frac{1}{2}}\rho}{m^{\frac{1}{2}}}\left(\frac{\rho_1\rho_2}{\rho^2}\right)^{\frac{3}{4}}. \tag{3.86}$$

The superfluid velocity is proportional to the gradient of the phase and in two-component fluid, there are two velocities

$$\mathbf{v}_1 = \frac{\hbar}{m}\nabla\theta_1, \tag{3.87}$$

$$\mathbf{v}_2 = \frac{\hbar}{m}\nabla\theta_2. \tag{3.88}$$

According to equations (3.81) it is easy to see that the total particle current is equal to zero

$$\rho_1\mathbf{v}_1 + \rho_2\mathbf{v}_2 = 0 \tag{3.89}$$

So, the domain wall is an area where the two components move in opposite directions, and the maximum of velocity corresponds to the centre of the domain wall ($z = 0$). Outside, on distances much higher than k^{-1} flow decreases to zero.

One can conclude that there is a conversion of particles inside the wall: the second type to the first and vice versa depending on the sign of x. Thus, the energy is absorbed and released in different parts of the domain wall.

Now let us consider the domain wall of finite size, bounded by a closed contour C. The length of C is much larger than the wall width, so that the domain wall can be approximated as an infinitely thin membrane, stretched on C. Choose another contour D in such a way that it crosses the membrane once. In that case across the contour D relative phase changes by 2π, similar to ones in a vortex. So C is a vortex line. Membrane bounded by vortex line will tend to shrink to reduce its own energy of the wall tension and boundary vortex tension.

In the model of two coupled condensates, there can be two types of vortices. The first I-type vortices with condensate ϕ_1 vanishing at the centre and $\phi_2 \neq 0$, and the second II-type vice versa, vanishing ϕ_2 and nonzero ϕ_1. Both types of vortices provide θ_A changing by 2π, so both can bound the domain wall.

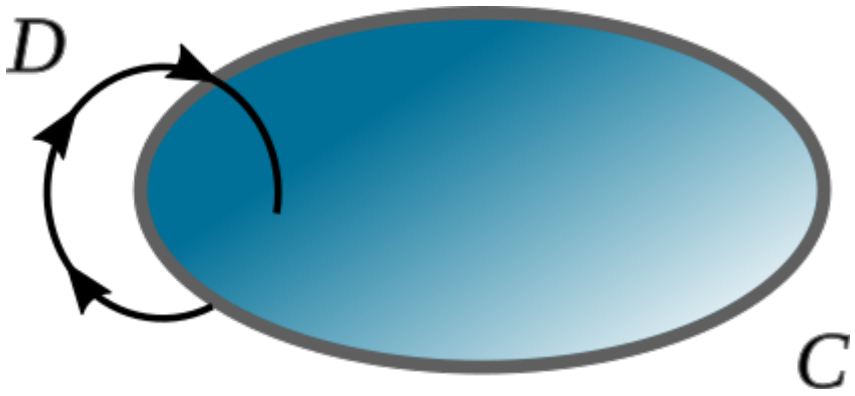

Figure 3.5: Finite domain wall with a closed boundary C

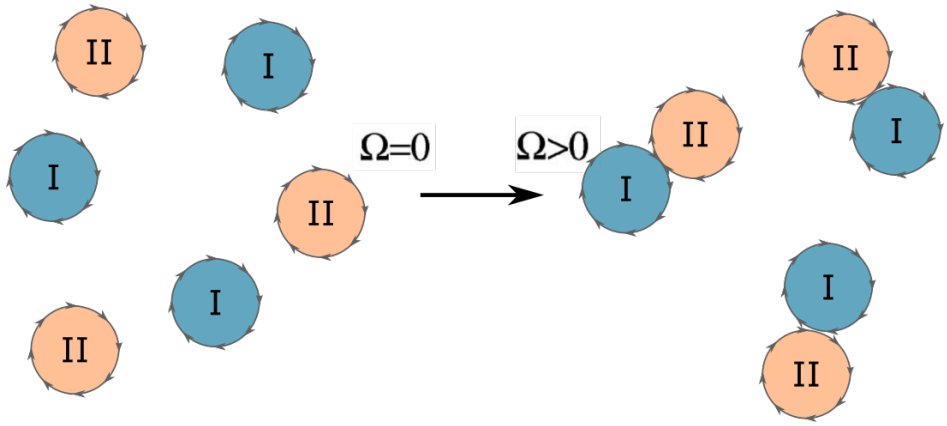

Figure 3.6: Pairs of vortices appearing at nonzero Ω

The pair of parallel vortices of different types cancel its θ_A charges and energy per unit length is logarithmically diverges. The same situation with the pair of parallel vortices of the same type and opposite winding. At the same time, energy of the lonely vortex diverges linearly with the size of the system. However, at $\Omega = 0$ even a lonely vortex have logarithmically divergent energy. So, one can conclude that at nonzero Ω vortices exist only in pairs.

The existence of the domain wall provides us with yet another exciting link with the physics of strong interactions described by Quantum Chromodynamics (QCD). If the domain wall in the mentioned vortex pair gets broken, new vortices appear from the condensate. The created vortices produce additional vortex pairs that are attached to the broken ends of the domain wall [85, 87]. The process is a direct analogue of the confining QCD string breaking, which extends between the (anti)quarks and gets broken if a sufficiently long distance separates the quarks. Thus, the appearance of the domain wall leads to a rather nontrivial vortex-pair dynamics [87, 88].

The confinement picture works only for a relatively small inter-condensate coupling given by the Rabi frequency Ω (or, for small off-diagonal mass m_5 in our notations). At a high inter-condensate coupling, the domain wall becomes unstable, and the vortex pairs are no more confined [85]. The inter-vortex potential is then given by the long-

range logarithmic potential (3.79) determined by the density wave exchange.

Non-Hermitian two-condensate model

The energy of the non-Hermitian two-condensate model (3.59) can also be rewritten as a formal expression similar to its Hermitian counterpart (3.60). In the non-Hermitian case, the meaning of the Rabi frequency Ω becomes rather transparent: the Rabi coupling Ω should couple to the different hyperfine spin components with a different sign. Leaving aside the physical realization of such a scenario, we notice that the non-Hermitian case can be analyzed closely paralleling the Hermitian case considered above. In particular, exactly the same field combinations (3.63) and (3.64) can be used to rewrite the non-Hermitian theory (3.59) in terms of the massless (density wave) and massive (spin wave) phase combinations:

$$\mathcal{L}_{\rm NH} = \kappa^2 \partial_\nu \chi \partial^\nu \chi + \mathcal{L}^{(M)}_{\rm NH}(\gamma)\,. \tag{3.90}$$

This non-Hermitian model possesses the usual Hermitian Goldstone mode χ which leads to the long-range interactions between the combinations of the worldsheets (3.73). However, the would-be massive excitation γ exhibits a non-Hermitian behavior described by the Lagrangian:

$$\mathcal{L}^{(M)}_{\rm NH}(\gamma) = \tilde{\kappa}^2 \left(\partial_\nu \gamma \partial^\nu \gamma + 2iM^2 \sin\gamma\right)\,, \tag{3.91}$$

and therefore the interaction between the would-be massive components of the vortex sheets (3.74) is not evident.

The model (3.91) is nothing but a non-Hermitian version of the Sine-Gordon model in (3+1) dimensions. As a side remark, we notice that the Lagrangian (3.91) appears as a bosonic dual of the non-Hermitian massive Thirring Model in (1+1) dimensions [27]. According to Ref. [27], this model with the purely imaginary coupling in front of the sine-term resides in the $\mathcal{PT}$-broken domain and, therefore, should be characterized by complex energy dispersions which correspond to dissipation or instability, or the both.

The second term in the Lagrangian (3.91) implies that the $\gamma = 0$ point is not a local extremum of the corresponding action. The stable minima could appear around the values $\gamma_\pm = \pm\pi/2$. Defining $\gamma = \pm\pi/2 + \delta\gamma$, we get the following equations of motion:

$$\Box\,\delta\gamma \pm iM^2 \sin\delta\gamma = 0\,, \tag{3.92}$$

which differ from the classical equations of motion of the Hermitian model (3.66) by the purely complex coefficient in front of the sine term. For small fluctuations around the minimum, $\delta\gamma = 0$, the solutions of Eq. (3.92) give us the dispersions for the energy:

$$\omega_{\boldsymbol{k}} = \sqrt{\boldsymbol{k}^2 \pm iM^2}. \tag{3.93}$$

We find that the particle-like, positive-energy solutions with $\mathrm{Re}\,\omega > 0$ lead to an explosive behavior near the $\gamma = -\pi/2$ minimum which appears to be unstable. For example, the amplitude of any zero-momentum solution ($\boldsymbol{k} = 0$) diverges with time t as $\delta\gamma \sim \exp(\Gamma t)$ where

$$\Gamma = \frac{M}{\sqrt{2}} \equiv \frac{\kappa_1^2 + \kappa_2^2}{\kappa_1 \kappa_2} \frac{m_5^2}{\sqrt{2}} > 0\,. \tag{3.94}$$

In the language of a Hermitian theory, the point $\gamma = -\pi/2$ would correspond to an extremum.

However, the minimum $\gamma = +\pi/2$ is stable so that all particle excitations around it behave as dissipative solutions $\delta\gamma \sim \exp(-\Gamma t)$ that approach the minimum point $\gamma = +\pi/2$ should the field γ deviate from it. Since the angle γ takes a constant value in the stable minimum, it evidently means that the field γ contains no vortex singularities in this ground state. According to Eq. (3.74), the vortex singularities in the both phases θ_1 and θ_2 should coincide with each other: $\Sigma_{\mu\nu}^{(M)} = \Sigma_{\mu\nu}^{(1)} - \Sigma_{\mu\nu}^{(2)} = 0$.

Thus, the vortices in the ϕ_1 and ϕ_2 condensate can only exist provided they coincide with each other, $\Sigma_{\mu\nu}^{(0)} = \Sigma_{\mu\nu}^{(1)} = \Sigma_{\mu\nu}^{(2)}$ thus forming a single double-vortex sheet $\Sigma_{\mu\nu}^{(0)}$ according to Eq. (3.73). Any fluctuation that separates the vortices leads to the energy dissipation with the dissipation rate (3.94) which returns the vortices back to their common stable non-dissipative minimum.

The common vortex line is described by the action of the vortex in the one-component condensate (3.48), where the coupling κ is given in Eq. (3.69). The energy per unit length of the joint vortex is thus given by Eq. (3.53). In this state, the common vortex segments interact with other segments via a long-range interaction mediated by massless particles. For the straight static vortices separated by the distance R, the interaction is given by Eq. (3.54).

As we mentioned earlier, the Hermitian counterpart (3.7) of the non-Hermitian system (3.5) appears in various physical contexts, including colour superconductors in high-density quark matter described by QCD, relevant for the description of, for example, the interior of the neutron stars [81, 82], and the axion cosmic strings [89]. In the field-theoretical context, both original U(1) degrees of freedom, representing the phases of the scalar condensates, mix up to form the $\mathrm{U}(1)_B$ ("baryon") global symmetry where both condensates transform with the same phase and $\mathrm{U}(1)_A$ ("axial") global symmetry which rotates the phases of the fields oppositely.[1] In our models, these global symmetries correspond to the Goldstone massless mode (3.63) and the massive excitation (3.64), respectively.

[1]The terms are taken from chiral physics of (massless) Dirac fermions where the vector and chiral rotations in internal space transform upper (right-handed) and lower (left-handed) Weyl components with the same (opposite) phases which corresponds to the vector (baryon) and axial rotations, respectively [90].

In particle physics, the axial symmetry is usually broken either by the axial quantum anomaly [91] or explicitly, by the (strange) quark mass, depending on the physical system described by the model. This effect is important in the cosmological context as it is responsible for the rapid decay of axion cosmic strings [89]. These topological defects, which are suggested to be formed in the early moments of our Universe, gets bounded to the QCD domain walls at the QCD finite-temperature phase transition. The walls decay rapidly after the QCD phase transition thus leaving no trace of the cosmic strings in the present-day Universe [92]. We will not pursue this topic further concentrating, instead, on the properties of vortices themselves in the contexts of the models. We notice that in model (3.7), the "axial" invariance is explicitly violated by the nonzero coupling $m_5 \neq 0$ between the two fields in the scalar doublet which makes the overall mechanism similar to the explicit breaking of the axial symmetry in QCD.

Vortices in Hermitian and non-Hermitian models in long-range limit: a brief comparison

It is worth comparing the properties of the vortices in Hermitian and non-Hermitian versions of the two-field model in the long-range limit. We have already seen that outside the long-range limit, the phase diagram of the Hermitian model (Section 3.1.3) has a much simpler structure as compared to the rich and complicated diagram which characterizes the phases of the non-Hermitian model (Section 3.1.3). The properties of the corresponding vortices, discussed in Sections 3.2.2 and 3.2.2, respectively, differ dramatically as well.

The Hermitian version of the model possesses two types of stable vortices associated with the phases of both condensates (3.75). The vortices interact with each other via nonlocal action (3.76) which describes the massive and massless interaction of the vortex worldsheets via exchanges of the massless (density wave) and massive (spin wave) excitations. The model also possesses the domain wall, a coherent structure in both condensates. However, in the limit of the sizeable inter-condensate coupling (given by the Rabi coupling Ω or the off-diagonal mass m_5, in our notations), the domain wall becomes unstable [85] and the long-range vortex dynamics is determined by the repulsive logarithmic potential.

The long-range limit of the non-Hermitian model resides in the $\mathcal{PT}$-broken phase, which indicates, according to the general arguments discussed earlier, instability. The instability indeed appears as a dissipation provided the vortex cores of different types are not overlapping exactly. Therefore, the separated vortices from different condensates tend to attract each other until they form a tightly bound pair that is perfectly stable.

Therefore, the behaviour of the vortices in the Hermitian and non-Hermitian cases

are somewhat similar: both of them tend to form pairs, albeit for different reasons. However, one should notice that the similarity is not exact: the binding of vortices in the Hermitian model appears due to the domain wall, which exists at low inter-condensate coupling, while the dissipative vortex binding in the non-Hermitian case is realized at the large values of this coupling.

3.3 Vortices in general case

The non-Hermitian two-field model possesses vortex solutions not only in the London (long-range) limit, where the amplitudes are fixed by the large quartic couplings λ_1 and λ_2 but also at finite values of the quartic couplings. The general is particularly interesting for the properties of the system at the scales of the order or smaller than the healing length.

In this section, we consider examples of the static straight vortex solutions of the classical equations of motion (3.16) assuming the standard axial ansatz for the scalar fields

$$\phi_a(r,\theta) = v_a f_a(r) e^{in\theta}\,, \qquad a = 1,2, \tag{3.95}$$

where r and θ are the radial coordinates in the (x_1, x_2) plane and $n \in \mathbb{Z}$ is the vorticity of the solution. These static and straight field configurations do not depend on time and x_3 coordinates. The vacuum values of the condensates, v_1 and v_2, are the solutions of Eqs. (3.21).

The consistency of the coupled solutions at $m_5 \neq 0$ imply that the vortices in ϕ_1 and ϕ_2 condensates should be superimposed on each other and they should have the same winding numbers $n_1 = n_2 = n$ in Eq. (3.95). Below we concentrate on the non-Hermitian model which is the subject of our work (the analysis of the Hermitian counterpart can also be performed in the same way).

The radial profiles of the vortices are described by the functions f_a with the following asymptotics:

$$\lim_{r\to\infty} f_a(r) = 1, \qquad \lim_{r\to 0} f_a(r) = 0, \qquad a = 1,2, \tag{3.96}$$

which guarantee that the total energy of the vortex solution is converging both at the spatial infinity and at the origin, respectively.

The classical equations of motion (3.16) lead to the following system of equations for the profile functions:

$$f_1''(r) + \frac{f_1'(r)}{r} - \frac{n^2}{r^2} f_1(r) - m_1^2 f_1(r) - m_5^2 \frac{v_2}{v_1} f_2(r) - 2\lambda_1 v_1^2 f_1^3 = 0\,, \tag{3.97a}$$

$$f_2''(r) + \frac{f_2'(r)}{r} - \frac{n^2}{r^2} f_2(r) - m_2^2 f_2(r) + m_5^2 \frac{v_1}{v_2} f_1(r) - 2\lambda_2 v_2^2 f_2^3 = 0\,, \tag{3.97b}$$

which, evidently, do not possess straightforward analytical solutions.

Close to the origin, the last non-linear terms in both equations (3.97) can be neglected and the differential equations can be linearized. The solutions can be represented in the form of the polynomials,

$$f_a(r) = \sum_{k=0}^{\infty} A_a^{(2k)} r^{n+2k} \,, \tag{3.98}$$

which involve only the positive even powers of the radius starting from the power r^n determined by the vorticity number $n = 1, 2, \ldots$. The ansatz (3.98) is thus consistent with the asymptotics (3.96). One gets for the first three coefficients:

$$\begin{aligned}
A_1^{(0)} &= A_1 \,, \qquad A_1^{(2)} = \frac{A_1 v_1 m_1^2 + A_2 v_2 m_5^2}{4(n+1)v_1} \,, \\
A_1^{(4)} &= \frac{A_1 v_1 (m_1^4 - m_5^4) + A_2 v_2 m_5^2 (m_1^2 + m_2^2)}{32(n+1)(n+2)v_1} \,, \\
A_2^{(0)} &= A_2 \,, \qquad A_2^{(2)} = \frac{A_2 v_2 m_1^2 - A_1 v_1 m_5^2}{4(n+1)v_2} \,, \\
A_2^{(4)} &= \frac{A_2 v_2 (m_1^4 - m_5^4) - A_1 v_1 m_5^2 (m_1^2 + m_2^2)}{32(n+1)(n+2)v_2} \,,
\end{aligned} \tag{3.99}$$

where A_1 and A_2 are free parameters of the solution which cannot be fixed at this stage. The series (3.99) of the f_1 and f_2 profile functions are related to each other by the flip of the sign in front of the off-diagonal mass term m_5^2.

In the large-distance region, $r \to \infty$, the asymptotics (3.96) imply $f_a = 1 - h_a$ where $|h_a| \ll 1$ at sufficiently large distances. The linearized equations of motion,

$$h_1''(r) + \frac{h_1'(r)}{r} - \frac{n^2}{r^2} h_1(r) - m_1^2 h_1(r) - m_5^2 \frac{v_2}{v_1} h_2(r) - 6\lambda_1 v_1^2 h_1(r) = 0 \,, \tag{3.100}$$

$$h_2''(r) + \frac{h_2'(r)}{r} - \frac{n^2}{r^2} h_2(r) - m_2^2 h_2(r) + m_5^2 \frac{v_1}{v_2} h_1(r) - 6\lambda_2 v_2^2 h_2(r) = 0 \,, \tag{3.101}$$

suggest that their solutions can be represented in the following form:

$$h_a(r) = B_a^{(0)} r^s e^{-\mu r} \,. \tag{3.102}$$

The self-consistency of the solutions provides us with the power $s = -1/2$ of the algebraic prefactor r^s and also imposes two simultaneous constraints:

$$\mu^2 - m_1^2 - m_5^2 \frac{B_2^{(0)} v_2}{B_1^{(0)} v_1} - 6\lambda_1 v_1^2 = 0 \,, \tag{3.103a}$$

$$\mu^2 - m_2^2 + m_5^2 \frac{B_1^{(0)} v_1}{B_2^{(0)} v_2} - 6\lambda_2 v_2^2 = 0 \,. \tag{3.103b}$$

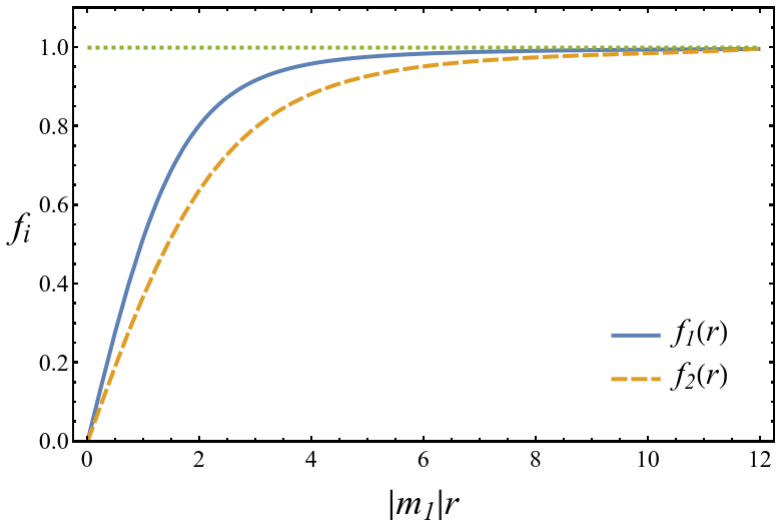

Figure 3.7: The profile functions of the elementary $n = 1$ vortex solution at the mass parameters $m_2^2 = |m_1^2|$ and $m_5^2 = 0.1|m_1^2|$ with $m_1^2 < 0$ and the equal quartic couplings $\lambda_1 = \lambda_2 = 1$. This figure has been taken from the work from A. Begun et. al, Phase diagram and vortex properties of a $\mathcal{PT}$-symmetric non-Hermitian two-component superfluid, Phys.Rev.D 104 (2021), 056024.

These equations give us two possible solutions for the ratio of the coefficients $B_a^{(0)}$ from Eq. (3.102):

$$\frac{B_1^{(0)}}{B_2^{(0)}} = \frac{v_2}{v_1}\left(\alpha \pm \sqrt{\alpha^2 - 1}\right), \tag{3.104}$$

and also determines the common exponent:

$$\mu = \sqrt{6\lambda_1 v_1^2 + m_1^2 + m_5^2\left(\alpha \pm \sqrt{\alpha^2 - 1}\right)}. \tag{3.105}$$

We denoted for brevity:

$$\alpha = \frac{6(\lambda_2 v_2^2 - \lambda_1 v_1^2) + m_2^2 - m_1^2}{2m_5^2}. \tag{3.106}$$

The next-order correction to Eq. (3.102) can also be easily obtained,

$$h_a(r) = \left(\frac{B_a^{(0)}}{r^{\frac{1}{2}}} + \frac{B_a^{(1)}}{r^{\frac{3}{2}}} + O\left(r^{-\frac{5}{2}}\right)\right) e^{-\mu r}, \tag{3.107}$$

where

$$B_a^{(1)} = \frac{1}{2\mu}\left(n^2 - \frac{1}{4}\right) B_a^{(0)}. \tag{3.108}$$

If the off-diagonal mass vanishes, $m_5^2 = 0$, the non-Hermitian two-scalar model reduces to two non-interacting scalar models $\mathcal{L}(\phi_1, \phi_2) = \mathcal{L}_1(\phi_1) + \mathcal{L}_2(\phi_2)$ with

$$\mathcal{L}_a(\phi_a) = \partial_\nu \phi_a^* \partial^\nu \phi_a - m_a^2 |\phi_a|^2 - \lambda_a \phi_a^4. \tag{3.109}$$

This single-field model possesses the asymptotic solutions of the form (we omit the index a for simplicity):

$$\begin{aligned} f(r) &= A\left[r^n + \frac{m^2}{4(n+1)}r^{n+2} + \frac{m^4}{32(n+1)(n+2)}r^{n+4} + O\left(r^{n+6}\right)\right], \quad (3.110) \\ h(r) &= B\left[\frac{1}{\sqrt{r}} + \frac{1}{2\mu r^{3/2}}\left(n^2 - \frac{1}{4}\right) + O\left(r^{-5/2}\right)\right] e^{-\mu r}, \end{aligned}$$

where the asymptotic behavior is controlled by the mass of the single scalar field:

$$\mu = \sqrt{m^2 + 6\lambda v^2} = 2\sqrt{\lambda}v^2 . \quad (3.111)$$

In this limit, the two equations (3.103) decouple, and the mass parameters reduce to Eq. (3.111) for each field. The asymptotics of the non-Hermitian solution (3.98), (3.100), (3.107), and (3.108) are consistent with the single-field solution (3.110) as well.

Our numerical analysis confirms the existence of the stable vortex solutions in the regions of the phase diagram with non-zero condensates. An example of the profile functions for a set of coupling constants is shown in Fig. 3.7. All the radial $n = 1$ profiles of the vortices exhibit the same qualitative features, the linear rise close to the origin and the exponentially slow approach of the corresponding vacuum expectation values at large distances. These properties reveal the generic behaviour of all solutions that we have analyzed.

The energy density of the non-Hermitian vortex (calculated per unit vortex length),

$$E_{\rm NH} = 2\pi \int_0^\infty r dr \big(|\nabla\phi_1|^2 + |\nabla\phi_2|^2 + m_1^2\phi_1^2 + m_2^2\phi_2^2 + \lambda_1\phi_1^4 + \lambda_2\phi_2^4\big), \quad (3.112)$$

can be simplified with the use of the corresponding equations of motion (3.16). It can be expressed via the profile functions f_a as follows:

$$E = 2\pi \int_0^\infty r dr \left\{\lambda_1 v_1^4[1 - f_1^4(r)] + \lambda_2 v_2^4[1 - f_2^4(r)]\right\}, \quad (3.113)$$

where the energy is normalized in such a way that $E = 0$ in the absence of the vortex. The very same expression (3.113) also gives us the energy of the vortex in the counterpart Hermitian theory (3.7),

$$E_{\rm H} = 2\pi \int_0^\infty r dr \big(|\nabla\phi_1|^2 + |\nabla\phi_2|^2 + m_1^2\phi_1^2 + m_2^2\phi_2^2 + 2m_5^2\phi_1\phi_2 + \lambda_1\phi_1^4 + \lambda_2\phi_2^4\big) \quad (3.114)$$

after the use of the corresponding classical equations of motion (3.27).

Finally, despite of the mundane similarity of the numerically obtained vortex configurations in various regions, one notices a rather unusual difference of the evolution of the vortex energy as the function of the off-diagonal mass parameter m_5 in Hermitian and non-Hermitian regions. We show examples of vortex energies in Hermitian and non-Hermitian theories in different stability areas, with $m_1^2 < 0$ and $m_2^2 > 0$ in

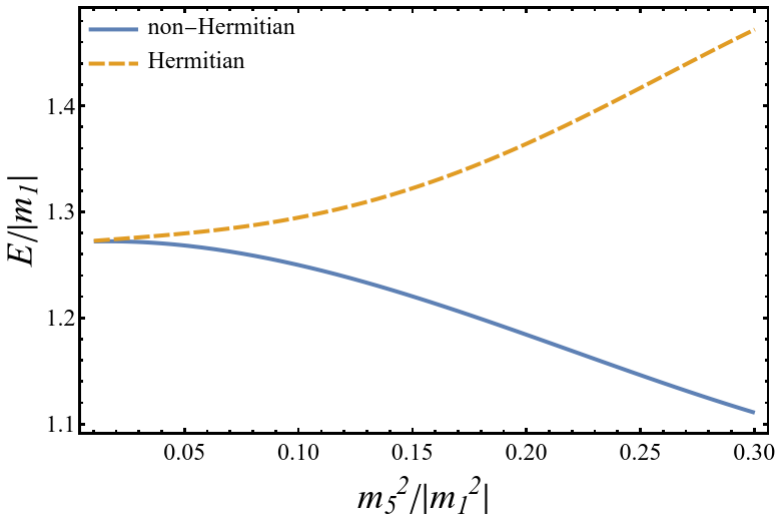

(a)

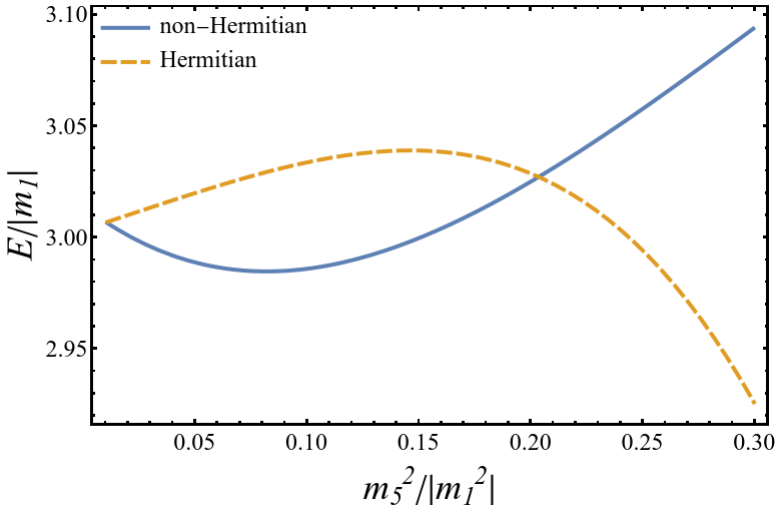

(b)

Figure 3.8: Hermitian and non-Hermitian vortex energies vs. the off-diagonal mass squared m_5^2 in different stability areas (a) $m_2^2 = -m_1^2 > 0$ corresponding to the border of the stable and unstable regions and (b) $m_2^2 = 2.5m_1^2 < 0$ residing within the stable region, at $\lambda_1 = \lambda_2 = 1$, Fig. 3.4(g). This figure has been taken from the work from A. Begun et. al, Phase diagram and vortex properties of a $\mathcal{PT}$-symmetric non-Hermitian two-component superfluid, Phys.Rev.D 104 (2021), 056024.

Fig. 3.8(a) and with $m_1^2, m_2^2 < 0$ in Fig. 3.8(b) at the same values of quartic couplings. The vortex energies in the Hermitian and non-Hermitian versions trivially coincide at $m_5 = 0$ and then they tend to separate as the off-diagonal mass m_5 increases. One notices the non-monotonic behaviour of energies in the completely broken ($m_1^2, m_2^2 < 0$) part of the phase diagram.

3.4 Discussion and Conclusion

In our work, we discuss the phase diagram and reveals the properties of line-like topological excitations and vortices in the non-Hermitian relativistic model of two interacting scalar complex fields. We concentrate on non-Hermitian parity-time ($\mathcal{PT}$) symmetric realization of the model, which describes an open system that communicates with an external environment with precisely balanced gains and losses. The exact balance is encoded in the $\mathcal{PT}$ symmetry of the model Lagrangian. This symmetry ensures the stability of its steady ground state provided that the $\mathcal{PT}$-invariance of the model is not broken spontaneously.

The model describes the properties of two scalar condensates that can exhibit the spontaneous breaking of the discrete $\mathcal{PT}$ symmetry in addition to the spontaneous breaking of the continuous global U(1) symmetry. Given the presence of the two symmetries that can be either broken or unbroken, the model thus contains four different phases, which makes the phase structure of the model very nontrivial.

The phase diagram of the non-Hermitian two-condensate model is shown in Figs. 3.1 and 3.4. We compared the non-Hermitian model with its Hermitian counterpart with identical couplings (Fig. 3.1), and we have observed the striking difference between the two cases. While the Hermitian model hosts the stable U(1) broken phase almost at every point of the phase diagram (except for a thin line, where the condensates decouple), the non-Hermitian diagram shows a wide variety of intertwined stable and unstable phases with both broken and respected U(1) symmetry. The richness of the phase diagram is guaranteed by the nontrivial pattern of the spontaneous $\mathcal{PT}$–symmetry breaking to the interacting theory.

On the practical level, the stability of the ground state can be identified via the absence of the negative modes in fluctuation matrix $\mathcal{M}^2_{\text{NH}}$ that describes the quadratic fluctuations of the fields (3.31) over the ground-state condensates. On the contrary, in the spontaneously $\mathcal{PT}$-broken regions, the quadratic fluctuation matrix contains at least a single negative eigenvalue.

In addition to the phase diagram, we studied the basic properties of global vortices in the non-Hermitian model in various regimes.

Firstly, we considered the model in the limit where the lengths of the condensates are frozen and the analytical analysis is feasible. To reveal the vortex properties,

we used a set of exact transformations of the field variables that did not involve the explicit solution of the equations of motion. Noticing that the model resides in the $\mathcal{PT}$-broken phase where the vortices are expected to be unstable, we show that the superfluid vortices can propagate non-dissipatively if and only if the vortex singularities in different condensates have the same vorticity (winding number) and, in addition, they overlap. In the case of the strong inter-condensate coupling determined by the non-Hermitian mass m_5, the joint vortex segments interact via a long-ranged exchange of a massless excitation, similarly to the vortices in a Hermitian one-condensate model. The dissipation rate of the individual (separated) vortex segments is controlled by the off-diagonal mass m_5, which, in turn, determines the interaction between the condensates.

The behaviour of the vortices in the Hermitian and non-Hermitian cases is qualitatively similar: both of them are forming pairs. However, the similarity is not exact for two reasons: In the Hermitian model, the binding of vortices proceeds via a formation of the domain wall that emerges between the vortices. In the non-Hermitian case, the binding appears due to the dissipative dynamics of the vortices until they overlap. Moreover, the confining domain walls exist at low inter-condensate coupling values, contrary to the non-Hermitian case in which the dissipative vortex binding is realized at the large inter-condensate coupling.

Secondly, we also studied the classical vortex configurations at finite quartic couplings. In order to identify the classical configurations, we used a single set of classical equations of motion, which is obtained by the variation of the action with respect to the original fields. We omitted the equivalent but the incompatible, complimentary set of equations that correspond to the action variation with respect to the conjugated fields. This procedure, which follows Refs. [58, 68], seems appropriate for the open systems residing in a steady-state regime, which does not necessarily coincide with the (thermal) equilibrium. Moreover, in this approach, the classical solutions possess a real-valued energy spectrum bounded below. The latter property is essential on the practical level as we search for the classical states using a (numerical) procedure based on the energy minimization as a criterion for the true (ground) state.

An alternative approach, based on the similarity transformation, does not possess the incompatibility of the two sets of equations of motion. This property makes the analytical procedure of finding the classical solutions more elegant [51, 65]. However, the same approach makes the kinetic term (of, at least, one of the fields) negatively valued, leading to the emergence of a negative quadratic mode for the classical solutions. Therefore, the mentioned class alternative solutions correspond to different, sphaleron-type saddle-point configurations, which can be significant for the thermal properties of the system.

We found that the $\mathcal{PT}$-symmetric two-component model admits the vortex solutions inside and at the border of the $\mathcal{PT}$-broken regions. These two-condensate vortex

solutions share similar behaviour with the vortices in the one-component relativistic superfluids. For consistency of the classical solution, the vortices of different condensates should have the same position in space-time and possess the same vorticity (winding number).

Finally, we proposed that a non-Hermitian two-condensate system can be realized in the Bose-Einstein condensates of atoms in two hyperfine spin states with the asymmetric Rabi coupling Ω, which couples to the different spin components with a different sign.

Appendices

Appendix A

Modelling of protein dynamics in terms of Landau-Ginzburg-Wilson approach

Lattice gauge field theory provides universal framework for analysis of systems with infinite degrees of freedom with corresponding local and global symmetry. It allows to develop new theoretical concepts for the condensed and soft matter physics. From other other hand such systems allow direct experimental study of new nontrivial properties of the gauge field theory, what can be applied to QCD and confinement understanding. One of the most interesting and unusual subjects to which a field theory approach can be applied is the protein research.

Currently, the most ambitious computational approaches to modelling the structure of proteins are based on classical molecular dynamics that allows us to describe the processes of protein folding in the case of short and fast folding proteins only [93]. For a realistic description of the tertiary and quaternary structures on large spatial and temporal scales computing power by 5-6 orders of magnitude greater than is technically achievable now is needed [94]. To overcome the computational problems and to make possible the practical modelling of the properties of proteins and their complexes over large time scales, a number of models based on a rough physical assumptions has been developed. These models, increasing the speed of calculations, systematically exclude the contributions to the total atomic force fields, which are assumed to be insignificant. For example, the force field UNRES [95] gives a very detailed, but still approximate expression for the potential energy, which includes fifteen different terms in conjunction with a simplified geometry. The considerable success of various approximate approaches allows us to raise the question - what are the factors that really important to describe the free energy?

In particular, is there a systematic method to approximate the force fields, based on first principles that can reproduce the correct structure of proteins? Such a classification scheme as the CATH [4] (http://www.cathdb.info/) and SCOP [96] (http://scop.mrc-lmb.cam.ac.uk/scop/), who develop a taxonomic approach to describe the topology of protein available database PDB, found that despite the differences in their amino acid structures, the

number of different shapes is limited. Such empirical data provide a conceptual framework for new methods for structure prediction. Within these methods folded protein structure assembled by combining fragments obtained from homologously related proteins already described in PDB. Since the number of conformations, which may be in a particular sequence is very limited, the basic idea is that various fragments, which have been described in the PDB, can be used as the designer of the building blocks for creating the folded protein. The whole structure can be obtained by coupling these fragments in the three-dimensional conformation, frequently via the energy function by comparison with similar homology by its control structures from PDB. According to the generally accepted tests Critical Assessment for Structural Prediction (http://www.predictioncenter.org/index.cgi), at the moment this type of practices have the greatest predictive power for the conformation of the protein. However, the disadvantage of these methods is the lack of sound energy function, which greatly complicates their application for research of dynamic aspects, including the processes of folding, and especially the nature of and reasons for the transition to incorrect protein folding.

One of the solutions of the problem can be obtained with the help of coarse grain modelling within effective field theory, which allows a natural way to introduce the collective degree of freedom and nonlinear topological structures based on fundamental principles of gauge symmetry. The corresponding field theory model is based on local symmetry of proteins that will dynamically define tertiary structure of proteins [97].

We develop an effective theory approach to investigate the phase properties of globular proteins. Instead of interactions between individual atoms or localized interaction centers, the approach builds directly on the tertiary structure of a protein.

A.1 Curves on the plane and in space

Consider a curve $\gamma(t)$ defined parametrically on a plane in Cartesian coordinates (x, y) with unit vectors $\mathbf{e_1}$ and $\mathbf{e_2}$. It is convenient to write the equation of the curve using a vector function:

$$\mathbf{r} = \mathbf{r}(t) = x\mathbf{e_1} + y\mathbf{e_2}, \tag{A.1}$$

where $\dot{x} = \frac{dx}{dt}$, $\dot{y} = \frac{dy}{dt}$.

The velocity vector of the curve $\gamma(t)$ is a vector with coordinates $\left(\frac{dx(t)}{dt}, \frac{dy(t)}{dt}\right)$. Then using a vector function, one can obtain :

$$|\mathbf{v}(t)| = |\frac{d\mathbf{r}(t)}{dt}| = |\dot{x}\mathbf{e_1} + \dot{y}\mathbf{e_2}| \tag{A.2}$$

As a parameter, one can use the length of the arc from some fixed point of the curve to its arbitrary point:

$$l = \int_a^b |\mathbf{v}(t)|\, dt, \tag{A.3}$$

Such a parametrization $\mathbf{r}(l) = (x(l), y(l))$ is called natural, and the length of the arc l is called a natural parameter. In this case, the vector velocity is unit $|v_l| = 1$.

In addition, it turns out to be useful to introduce another vector - the acceleration of the curve:

$$\ddot{\mathbf{r}}(l) = \frac{d\mathbf{v}}{dl}. \tag{A.4}$$

It is easy to see that the vectors $\mathbf{v}(l)$ and $\dot{\mathbf{v}}(l)$ are orthogonal. In the general case, the acceleration vector is not unit, normalizing it, we get a unit vector called the normal vector:

$$\mathbf{n}(l) = \frac{\dot{\mathbf{v}}(l)}{|\dot{\mathbf{v}}(l)|} \tag{A.5}$$

Thus, we obtain a family of frames $(\mathbf{v}(s), \mathbf{n}(s))$, called Frenet frames.

The curvature of a curve at a point l is the quantity

$$k(l) = |\frac{d^2\mathbf{r}(l)}{dl^2} \tag{A.6}$$

i.e. acceleration module.

If the curve is given by a natural parameter, there are equations called Frenet's formulas:

$$\frac{d\mathbf{v}(l)}{dl} = k(l)\mathbf{n}(l), \tag{A.7}$$

$$\frac{d\mathbf{n}(l)}{dl} = -k(l)\mathbf{v}(l). \tag{A.8}$$

In the matrix form

$$\frac{d}{dl}\begin{pmatrix}\mathbf{v}(l)\\ \mathbf{n}(l)\end{pmatrix} = \begin{pmatrix}0 & k\\ -k & 0\end{pmatrix}\begin{pmatrix}\mathbf{v}\\ \mathbf{n}\end{pmatrix} \tag{A.9}$$

From this expression follows the geometric sense of curvature, as the rate of rotation of the Frenet frame. Thus, in the case of a plane curve, a smooth function $k(l)$ such that $k \neq 0$ for any l uniquely defines a curve with subtlety up to parallel translation for which $k(l)$ is the curvature, and l as a natural parameter.

Now let us consider curve in three dimensional space

$$\mathbf{r}(l) = x\mathbf{e_1} + y\mathbf{e_2} + z\mathbf{e_3}. \tag{A.10}$$

It's speed is given by the following expression:

$$\mathbf{v}(l) = \dot{x}\mathbf{e_1} + \dot{y}\mathbf{e_2} + \dot{z}\mathbf{e_3}. \tag{A.11}$$

In three-dimensional space, two vectors are not enough to construct the frame, we need to introduce the third vector - the binormal vector

$$\mathbf{b} = [\mathbf{v}, \mathbf{n}] \tag{A.12}$$

In this notation, the following Frenet formulas hold for any space curve

$$\frac{d\mathbf{n}}{dl} = \quad \tau\mathbf{b} - k\mathbf{v}, \tag{A.13}$$

$$\frac{d\mathbf{b}}{dl} = -\tau\mathbf{n}, \tag{A.14}$$

$$\frac{d\mathbf{v}}{dl} = \quad k\mathbf{n}, \tag{A.15}$$

where τ is the torsion of the curve. The geometric meaning of torsion is the rate of rotation of the frame $(\mathbf{n}, \mathbf{b})$ around the velocity vector $\mathbf{v}$.

In matrix form, these equations can be written as follows:

$$\frac{d}{dl}\begin{pmatrix}\mathbf{n}\\ \mathbf{b}\\ \mathbf{v}\end{pmatrix} = \begin{pmatrix}0 & \tau & -k\\ -\tau & 0 & 0\\ k & 0 & 0\end{pmatrix}\begin{pmatrix}\mathbf{n}\\ \mathbf{b}\\ \mathbf{v}\end{pmatrix}. \tag{A.16}$$

Thus, curvature and torsion for a space curve represent a complete set of geometric invariants, that is, if the functions $k(l)$ and $\tau(l)$ are known along the entire length of the curve, it is possible to reconstruct the curve up to the motions of the entire space. This pair of functions is called the Frenet coordinates of the curve.

It is easy to see that local rotation Frenet frame around $\mathbf{v}$ in any point leaves form of the curve invariant. Frenet's equations with such a rotation are as follows

$$\frac{d}{dl}\begin{pmatrix}\mathbf{n}\\ \mathbf{b}\\ \mathbf{v}\end{pmatrix} = \begin{pmatrix}0 & (\tau+\eta_l) & -k\cos\eta\\ -(\tau+\eta_l) & 0 & k\sin\eta\\ \kappa\cos\eta & -\kappa\sin\eta & 0\end{pmatrix}\begin{pmatrix}\mathbf{n}\\ \mathbf{b}\\ \mathbf{v}\end{pmatrix}, \tag{A.17}$$

where η is the rotation angle.

If the curve is not smooth, but piecewise-linear, it is necessary to pass from continuous functions $k(l)$ and $\tau(l)$ of curvature and torsion to their discrete analogs - the angle of curvature κ_i and the angle of torsion τ_i, where i is the number of the curve site.

We replace the continuous vector function $\mathbf{r}(l)$ by the set of radius vectors $\mathbf{r}_i$ of each individual site of the chain. The velocity vector $\mathbf{v} = \dot{\mathbf{r}}$ will go into a vector connecting two neighboring sites, that is, coinciding with a piecewise linear curve at a given point:

$$\mathbf{t}_i = \frac{\mathbf{r}_{i+1} - \mathbf{r}_i}{||\mathbf{r}_{i+1} - \mathbf{r}_i||}. \tag{A.18}$$

The binormal vector $\mathbf{b_i}$ is defined as the cross product of two adjacent tangential vectors:

$$\mathbf{b_i} = [\mathbf{t}_{i-1}, \mathbf{t}_i], \tag{A.19}$$

The third vector of the Freinet frame is defined as the cross product of the other two

$$\mathbf{n}_i = [\mathbf{b_i}, \mathbf{t_i}]. \tag{A.20}$$

The triple of vectors $(\mathbf{n_i}, \mathbf{b_i}, \mathbf{t_i})$ is a discrete analog of the Frenet frame at each site of a piecewise linear curve in three-dimensional space.

Let us transfer from continuous Frenet coordinates to the angles of curvature and torsion

$$\kappa_i = \arccos(\mathbf{t_{i+1}}, \mathbf{t_i}), \tag{A.21a}$$

$$\tau_i = \arccos(\mathbf{b_{i+1}}, \mathbf{b_i}). \tag{A.21b}$$

In this term discrete analog of Frenet equations is

$$\begin{pmatrix}\mathbf{n_{i+1}}\\ \mathbf{b_{i+1}}\\ \mathbf{t_{i+1}}\end{pmatrix} = \begin{pmatrix}\cos\kappa\cos\tau & \cos\kappa\sin\tau & -\sin\kappa\\ -\sin\tau & \cos\tau & 0\\ \sin\kappa\cos\tau & \sin\kappa\sin\tau & \cos\kappa\end{pmatrix}_i \begin{pmatrix}\mathbf{n_i}\\ \mathbf{b_i}\\ \mathbf{t_i}\end{pmatrix} \tag{A.22}$$

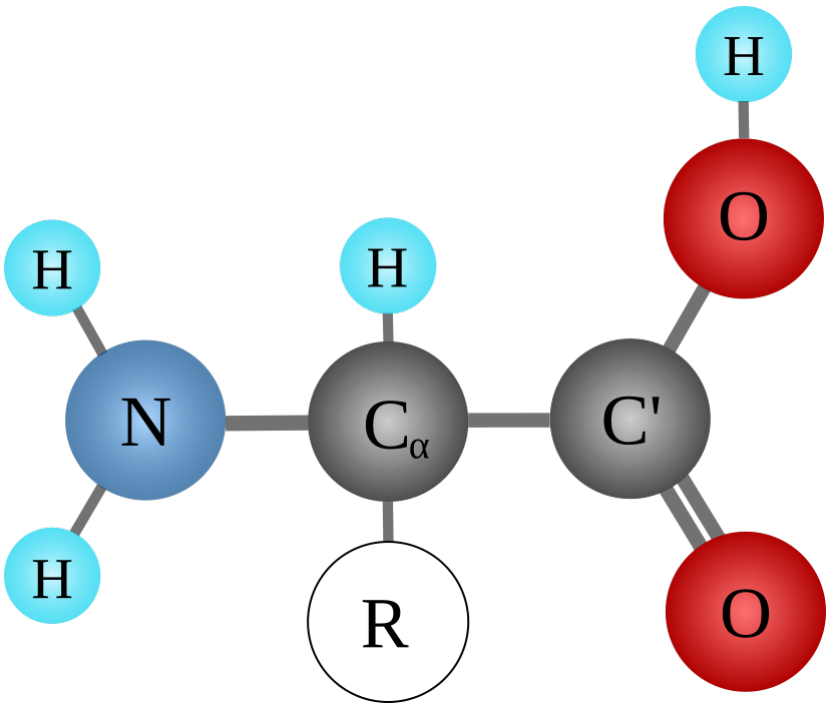

Figure A.1: Aminoacid molecule

Using this equation, from the Frenet frame at the site i we can get the frame at the site $i+1$. Having passed in this way along the entire curve from the beginning to the end, we can restore the frames at each point of the curve, which means we get the geometric place in the space of all sites of the curve:

$$\mathbf{r_i} = \sum_{i=0}^{i-1} l_0 \mathbf{t_i}, \tag{A.23}$$

where l_0 is the distance between the two nearest nodes of the curve. In the general case, l_0 can vary from site to site, then, in addition to the complete set of angles of curvature and torsion, it is also necessary to know the set of lengths of segments of a piecewise linear curve.

A.2 Protein structure

In 1902, E. Fisher showed that a protein is a polymer - a long peptide chain of amino acid residues. Amino acids are called aminocarboxylic acids - organic molecules that simultaneously contain amine ($-NH_2$) and carboxyl ($-COOH$) groups. The structure of an amino acid is shown in the figure A.1.

At the center of the amino acid is a carbon atom called the α atom or C_α. The *alpha*-carbon is associated with the nitrogen of the N amine group, the carbon C' of the carboxyl group, the hydrogen atom and the hydrocarbon radical R, which determines the type of amino acid.

Amino acids can interact with each other, whereby the hydrogen atom bonded to the nitrogen atom in the amine group of one molecule binds to the hydroxyl group OH of the carboxyl group of another molecule. As a result, a water molecule is formed, and a chemical

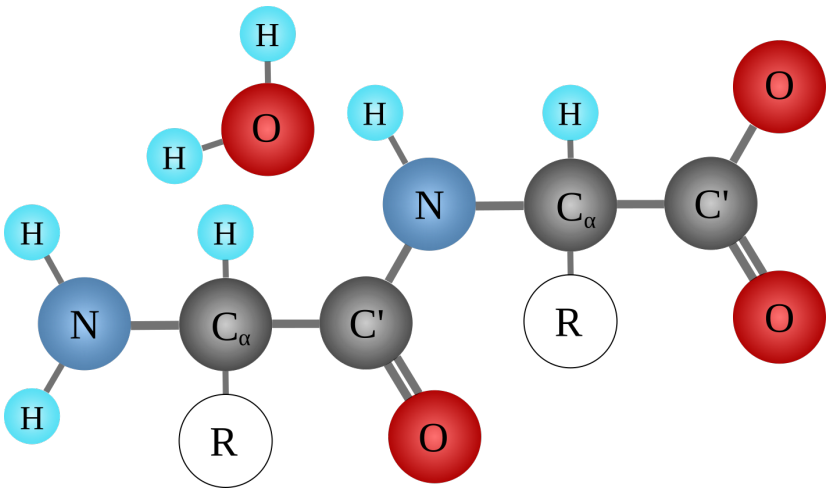

Figure A.2: Peptide bond formation

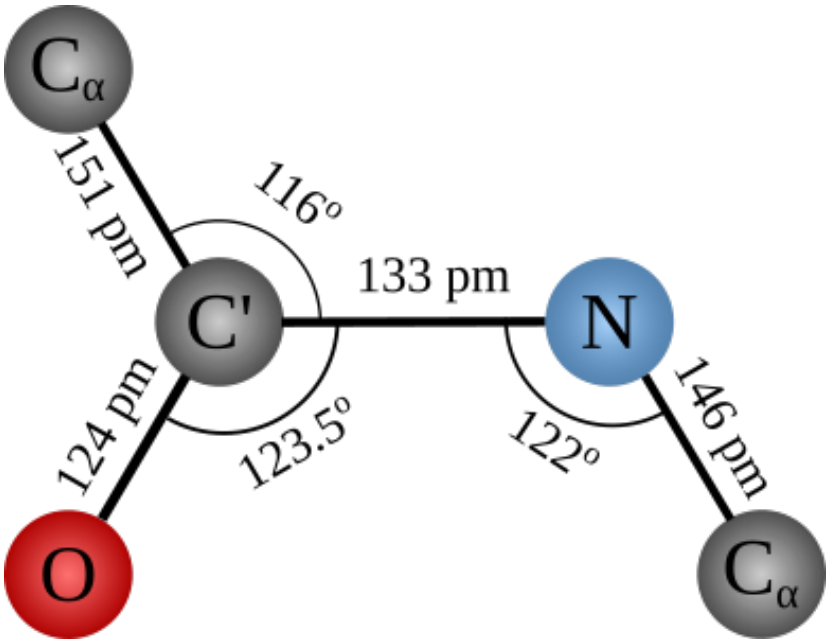

Figure A.3: Structure of peptide plane

bond occurs between nitrogen and carbon, shown in the figure A.2 and called a peptide bond. Further, other amino acids can be attached to this molecule, forming a long peptide chain.

Amino acid residues in such a chain have a rigid structure: fixed angles and distances between atoms (Figure A.3). In addition, it is important that all the atoms of the amino acid residue backbone lie in one plane.

The covalent bond between the central atom of the amino acid C_α and the carbon of the carboxyl group C' has a very low rotational energy, while the energy of the remaining bonds is very high and all the atoms of the peptide group lie in the same plane, as mentioned earlier.

With this in mind, we can imagine the protein chain as a sequence of planes freely rotating around this $C_\alpha - C'$ bond. Taking into account the rigid bonds in the peptide group, it can be found that the positions of the C_α atoms uniquely determine the coordinates of all other atoms. Based on this, to simplify the description of a protein molecule as much as possible,

we can leave only the C_α atoms in consideration, connect them with links, and describe the peptide chain in terms of discrete Frenet coordinates (angles of curvature and torsion).

Hydrophobic and hydrophilic forces wrap amino acids in and out of the secondary structure of the protein. Such a violation of symmetry can be regarded as a manifestation of chirality as a consequence of the geometric structure of amino acids. The C_α atom is in a sp^3 hybridized state, so its covalent bonds form a regular tetrahedron, at the vertices of which are the H, N , C' and C_β atoms. This structure is chiral. All constituent amino acids are left-handed, except for glycine, which has no radical and, as a consequence, is not chiral. This violation of symmetry leads to chirality of the basic structures of polypeptide states.

A.3 Abelian Higgs model

Consider the Lagrangian of the form

$$\mathcal{L} = -\frac{1}{4}F_{\mu\nu}^2 + D_\mu\phi^* D^\mu\phi - \lambda(\phi^*\phi - v^2)^2, \tag{A.24}$$

where $F_{\mu\nu} = \partial_\mu A_\nu - \partial_\nu A_\mu$, $D_\mu\phi = \partial_\mu\phi - ieA_\mu\phi$ is covariant derivative and A_μ is gauge field.

This Lagrangian is invariant under local $U(1)$ gauge transformation

$$\phi(x) \to e^{i\alpha(x)}\phi(x), \tag{A.25}$$

$$A_\mu(x) \to A_\mu(x) - \partial\alpha(x). \tag{A.26}$$

Let us choose the function $\alpha(x)$ so that at all points of the space the scalar field $\phi(x)$ has only a real component. In this case, the potential will have minimum at two values of the field: $\phi = v$ and $\phi = -v$.

Corresponding Hamiltonian is as follows

$$H = \frac{1}{4}F_{\mu\nu}^2 + |(\partial_\mu + ieA_\mu)\phi| + \lambda(\phi^2 - v^2)^2. \tag{A.27}$$

Referring to the Frenet coordinates, you can see that when you rotate the local coordinate system (Frenet frame) (A.17), the dynamic variables (curvature and torsion) are transformed as a two-dimensional Abelian Higgs multiplet [98]. Such a transformation can be rewritten as a gauge transformation of scalar and vector fields (A.25, A.26), while the curvature is identified with the scalar field, and torsion - with the vector [97, 99]

$$\kappa \sim \phi \to \kappa e^{-i\eta} \equiv \phi^{-i\eta}, \tag{A.28}$$

$$\tau \sim A_i \to \tau + \eta_l \equiv A_i + \eta_l. \tag{A.29}$$

Thus, the Hamiltonian of the Higgs Abelian model (A.27) takes the form:

$$H = \int_0^L dl\big(|(\partial_l + ie\tau)\kappa|^2 + \lambda(|\kappa|^2 - m^2)^2\big). \tag{A.30}$$

The Chern-Simons term $a\tau$ should be added to the Hamiltonian (A.30) in order to ensure the chirality of the proteins and the dominance of the right α helices. It is also necessary

to add the Proca mass term $\frac{c}{2}\tau^2$, which is responsible for the partial breaking of the gauge symmetry. Then we will finally have:

$$H = \int_0^L dl\big(|(\partial_s + ie\tau)\kappa|^2 + \lambda(|\kappa|^2 - m^2)^2 + a\tau - \frac{c}{2}\tau^2\big). \tag{A.31}$$

A.3.1 Soliton solutions

Protein structure studies have shown that folded proteins have a modular structure, that is, they consist of a set of [100] building blocks. The discovery of new topological blocks is so rare that many scientists believe that most of the building blocks are already known. Such universality in architecture suggests that protein folding occurs in accordance with some universal principle of self-organization [101]. This is confirmed by the results of the work of K. Anfinsen [102, 103]. In 1962, he showed that the formation of a three-dimensional structure of a protein, which usually occurs immediately during biosynthesis, can also occur spontaneously during the folding of a previously unfolded protein, that is, the amino acid sequence itself determines the spatial structure of the protein.

Based on the Hamiltonian (A.31), we can observe the ground states of the protein chain as vacua with different topological sectors:

- α-helix (broken chiral symmetry, negative parity)

$$\begin{cases} \kappa \simeq \frac{\pi}{2} \\ \tau \simeq 1 \end{cases} \tag{A.32}$$

- β-strand (restored chiral symmetry, positive parity)

$$\begin{cases} \kappa \simeq 1 \\ \tau \simeq \pi \end{cases} \tag{A.33}$$

Loops can be considered as a spatial transition between different ground states [104, 105]. They represent the points of inflection of the protein chain, at these points the curve becomes flat ($\tau = 0$). The equation of motion for the torsion-independent real part of the Hamiltonian (A.31) has the form of an exact soliton solution [106, 107]:

$$\kappa(l) = m\tanh(m\sqrt{\lambda}(l - l_0), \tag{A.34}$$

that has the energy

$$E = \int ds(\kappa_s^2 + \lambda(\kappa^2 - m^2)^2 - a\tau - b\kappa^2\tau + \frac{c}{2}\tau^2 + \frac{d}{2}\kappa^2\tau^2). \tag{A.35}$$

The stable conformation of the protein should obviously correspond to the minimum of the energy functional (A.35). Therefore, we can express the torsion τ from the energy extremum condition:

$$\frac{\delta E}{\delta \tau} = d\kappa^2\tau - b\kappa^2 - a + c\tau = 0. \tag{A.36}$$

And in the discrete form

$$\tau_i = \frac{a + b\kappa_i^2}{c + d\kappa_i^2}, \tag{A.37}$$

$$E = \sum_{i=0}^{N}(\kappa_{i+1} - \kappa_i)^2 + \sum_{i=1}^{N}(\lambda(\kappa_i^2 - m^2)^2 - a\tau_i - b\kappa_i^2\tau_i + \frac{c}{2}\tau_i^2 + \frac{d}{2}\kappa_i^2\tau_i^2). \tag{A.38}$$

This approach makes it possible to represent the protein structure with high accuracy in the form of a superposition of one-dimensional solitons (multi-soliton), as well as to describe the dynamic properties of the protein chain.

The multi-soliton profile then describes the various super-secondary structures such as helix-loop-helix (regular-loop-regular) as mutually interacting individual solitons [108, 109]. Over a single soliton profile the parameter values in (A.38) are uniform, and since a soliton extends over several amino acids the number of parameters is generically much smaller than the number of amino acids.

A.4 Protein tertiary structure and the myoglobin phase diagram

Myoglobin is a stable, relatively simple globular protein that exemplifies a paradigm in protein folding and unfolding research. The native folded state (N) of myoglobin is very compact and contains eight α helices (labeled A to H). Since there is no obvious static channel for ligand entry and exit, myoglobin must undergo conformational deformations for their passage [110–114]. These deformations are determined by changes in physiological conditions, in particular changes in temperature and acidity. Several experiments have been carried out to study the (en) folding of myoglobin as a function of pH, mainly at room temperature. These experiments show that unfolding occurs reversibly and sequentially in accordance with a four-state scheme: at low values of $pH \sim 2$, the structure resembles a random coil (U). In the $2 \leq pH \leq 4$ region, two intermediate states I_a and I_b [115, 116] can be found, both akin to a molten globule [117, 118] with a structure that changes when $changespH$. When pH reaches values in excess of $4 - 4.5$ myoglobin begins to enter its natural folded state (N). In general, the transitions, obviously, occur according to the scheme $N \leftrightarrow I_b \leftrightarrow I_a \leftrightarrow U$ when the acidity [115] changes. Experiments with temperature variation are less common, but the results are very similar [119–121]: at very low temperatures and almost neutral pH, the myoglobin structure is in a folded native state N; The F helix is disordered even at relatively low temperatures. Below $T \sim 340K$ and pH, which is close to neutral, the structure remains in the region of its native state. With a further increase in T, myoglobin turns into a molten globule, and when the temperature becomes even higher, the percentage of the helices begins to decrease: first, the F helix unfolds, followed by the B, C, D and E helices, then helices A, G and H. At very high temperatures, the structure resembles a random wandering of the polymer chain.

In the case of a myoglobin, we use the Protein Data Bank (PDB) structure 1ABS (sperm whale) [122] as a decoy to construct the parameters. This structure has been measured at

the very low liquid helium temperature value of around 20 Kelvin and as a consequence the thermal B-factors are very small. We identify ten individual solitons profiles along the 154 residue 1ABS backbone that become combined into a single multi-soliton solution of the DNLS equations (A.35), (A.36) with $\sim$ 0.8Å C_α root-mean-square-distance (RMSD) precision [99].

We construct the T-pH phase diagram by computing the grand canonical ensemble of statistical physics, and evaluate the observables $\mathcal{O}(\theta,\phi)$ by averaging them over all possible tertiary structures, weighted by the grand canonical distribution with free energy (A.38):

$$< \mathcal{O}(\theta,\phi) >_{\beta,\mu} = \frac{1}{\mathcal{Z}} Tr\{\mathcal{O}(\theta,\phi) e^{-\beta(E-\mu N)}\} \tag{A.39}$$

Here $\mathcal{Z}$ is a normalization factor, β is the inverse temperature factor and μN is a chemical potential contribution to be specified. Since the trace extends over all possible tertiary structures, the entropy contribution relates to the number of all possible tertiary structures. We evaluate (A.39) numerically, using the Glauber algorithm (appendix B.2) with acceptance ratio determined by the probability distribution

$$P = \frac{e^{-\beta\Delta(E-\mu N)}}{1+e^{-\beta\Delta(E-\mu N)}}, \tag{A.40}$$

where $\Delta(E-\mu N)$ is the variation of $(E-\mu N)$ between consecutive Monte Carlo steps.

We determine the chemical potential contribution in (A.39), by recalling the Henderson-Hasselbalch equation [123] that relates the concentrations of protonated and non-protonated amino acids to the difference between pH and acid dissociation constant pK_a. On the other hand, Gibbs free energy is commonly taken to vary with acidity as follows,

$$\Delta G = RT\ln(10)\sum_a (pH - pK_a) = RT\sum_a \ln\left(\frac{1-P_H^a}{P_H^a}\right), \tag{A.41}$$

where P_H^a is the protonation probability of a particular amino acid. Histidine with $pK_a \sim 6.0$ is the only amino acid in the genetic code that has strong reactivity to pH variations in the physiologically important range from pH$\sim$ 8 down to pH$\sim$ 4. For lower pH both glutamic acid ($pK_a \sim 4.2$) and aspartic acid ($pK_a \sim 3.9$) need to be accounted for. For simplicity, here we only aim to model the phase diagram for pH above ~ 4 and up to neutral value so that we only need to account to the contribution of the $N_H^{his} = 12$ histidines in 1ABS. Then

$$P_H^{his} = \frac{e^{-\Delta G/RT}}{1+e^{-\Delta G/RT}} \tag{A.42}$$

and to leading order

$$\Delta G \approx RT\ln(10)(pH-pK_a)N_H^{his}\frac{e^{-\ln(10)(pH-pK_a)}}{1+e^{-\ln(10)(pH-pK_a)}}. \tag{A.43}$$

We recognize in (A.42) the format of the Glauber transition probability (A.40). Moreover, since a unique conserved number operator $N \sim \kappa^2$ [106] we propose that in the LGW approach

$$G \sim E - \mu N = E - \mu\sum_{i\in his}\kappa_i^2, \tag{A.44}$$

where the summation extends over the histidines of 1ABS. As a consequence, to leading order in the LGW approximation μ depends linearly on pH. We also note that for 1ABS pH=9.0. Accordingly we normalize $\mu = 0$ at that value, to ensure that the ensuing multi-soliton profile models the 1ABS backbone.

As order parameters a.k.a. reaction coordinates we use the radius of gyration R_g and the α-helical content Q_α. We compute their (T, μ) dependence numerically from (A.39). We take a C_α atom to be in an α-helical posture when for (κ_i, τ_i) both

$$|\kappa_i - \kappa_0| \leq 0.14\,(rad), \tag{A.45}$$

$$|\tau_i - \tau_0| < 0.3\,(rad), \tag{A.46}$$

where $\kappa_0 = 1.55$ and $\tau_0 = 0.9$ are the PDB average values of the α-helical bond and torsion angle. The Q_α counts the relative number of residues in α-helical posture as a function of T and pH; most PDB myoglobins have a Q_α value 72–78%, and for 1ABS $Q_\alpha = 72\%$.

We have simulated 5000 independent heating and cooling (unfolding and folding) trajectories using the Glauber algorithm, obtained by varying the inverse temperature factor β; the trajectories are equally distributed between 50 values of $\mu \in [0, 0.05]$. Along each trajectory we first increase temperature (i.e. decrease β) at an adiabatically slow rate, so that the system remains very close to a thermal equilibrium for all β. The value of β is also kept at its high temperature value for a large number of simulation steps, for full thermalization. Finally, the system is brought back to the low temperature value, by reversal of the heating procedure: we have been extremely careful to always thermalize the ensemble before we evaluate any observable.

In Figure A.4 we compare the $\mu = 0$ temperature dependence of the observable Q_α to experimentally measured α-helicity of (horse heart) myoglobin during thermal denaturation. The experimental data is adapted from [120]. We use this Figure to relate the Glauber temperature T_G to Celsius scale. Accordingly, our simulations cover the range $0℃ - 120℃$ at each μ value.

We got that the Glauber scale is related to the Kelvin scale as follows

$$T_G = T_K e^{0.232 T_K - 107.8}. \tag{A.47}$$

Figure shows the helix (dis)ordering during a heating and cooling simulation cycle, as a function of temperature at $\mu = 0$ and in terms of the average value of torsion angles τ; we recall that for an α-helix $\tau \approx 1$ (rad).

We observe that F-helix starts to disorder soon after $T = 20℃$ and becomes fully randomized slightly above $T = 40℃$. The next to disorder are the helices B, C, D and E; this occurs near $T = 90℃$. This is followed by disordering of the helices H and A, and the helix G is last to disorder. Slightly above $T = 100℃$ the entire chain is fully randomized; according to Figure A.4, at these temperature values Q_α also reaches its high temperature asymptotic value. All these simulation results are fully in line with experimental observations [124].

Figure A.6 identifies the simulated phase structure on the (T, μ) plane in terms of radius of gyration R_g. For $\mu \approx 0$ we confirm the findings of the Figures A.4 and A.5: The native state

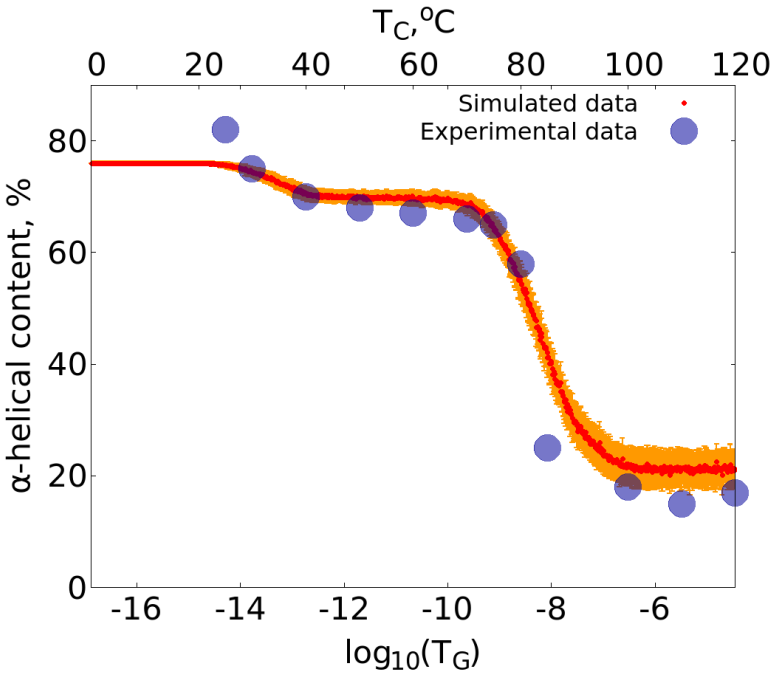

Figure A.4: Comparison between simulated (sperm whale) value Q_α that counts the relative number of residues in α-helical posture, and experimentally determined (horse heart) α-helical content during thermal denaturation. Experimental data is adapted from [120]. This figure has been taken from the work from A. Begun et. al, Protein tertiary structure and the myoglobin phase diagram, Scientific Reports vol. 9 (2019), 10819.

(N) is a region with low temperature ($T < 30$℃) and very small values $\mu < 0.003$. Beyond this there is a region where the F-helix (dis)orders (F), it extends to around $T \approx 40$℃ and to μ-values up to $\mu \approx 0.01$. When T and μ increase further, we identify a phase that we denote Ib and identify as a molten globule intermediate; the radius of gyration values are above 20Å but below 28Å in this region, depending on values of T and μ.

We propose that the high sensitivity of the F-helix that we observe, when either temperature or acidity increases from their low values, controls the ligand entry and exit: The F-helix contains the proximal histidine that is connected to the heme. Thus disordering of the F-helix may expose the heme, for ligand transport.

At $\mu \approx 0.027$ and for values $T < 80$℃ we observe a rapid transition: The radius of gyration decreases in a jump-like fashion, by around $4 - 6$Å depending on T. We interpret this to be a transition between two molten globule intermediates so that for $\mu > 0.027$ we have the second molten globule I_a [115, 116].

Most notably, we observe the presence of an apparent tricritical point, in conjuction with the two molten globule states: The transition line between I_a and I_b terminates at around $T \approx 80$℃ when both molten globules simultaneously enter the random coil phase.

Finally, in Figure A.7 we display the values of $Q\alpha$ that counts the relative number of residues in α-helical posture, for $T < 40$℃. We observe that there is only a weak dependence

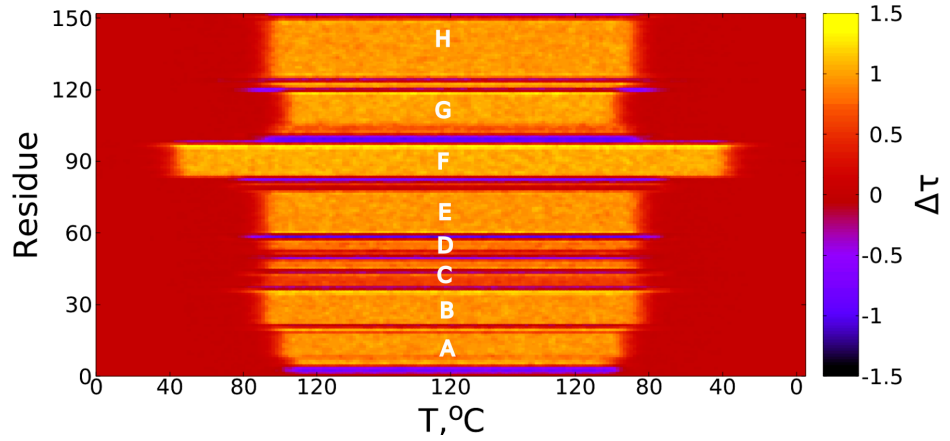

Figure A.5: (Dis)ordering temperatures for the eight helices A-H at $\mu = 0$, in terms of deviations in torsion angles from their α-helical values. This figure has been taken from the work from A. Begun et. al, Protein tertiary structure and the myoglobin phase diagram, Scientific Reports vol. 9 (2019), 10819.

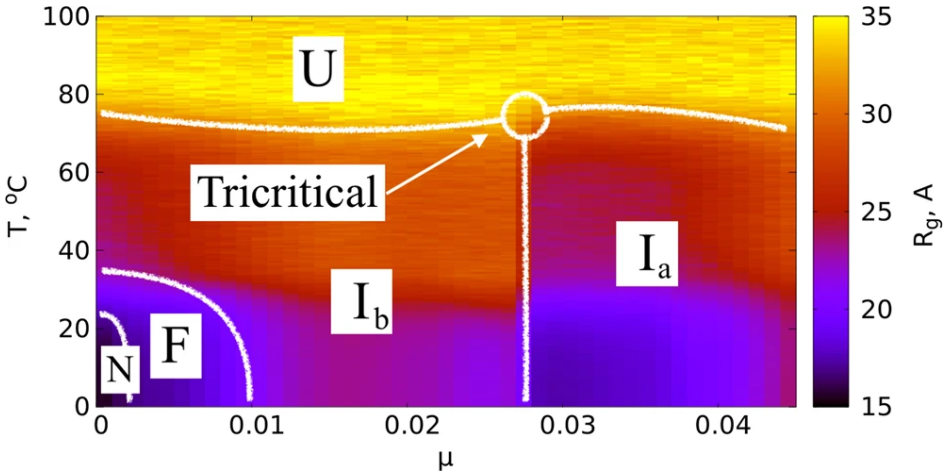

Figure A.6: The R_g phase diagram: Collapsed native state (N), (dis)ordering of F-helix (F), two molten globules (I_a and I_b) and random coil (U) phase are identified. This figure has been taken from the work from A. Begun et. al, Protein tertiary structure and the myoglobin phase diagram, Scientific Reports vol. 9 (2019), 10819.

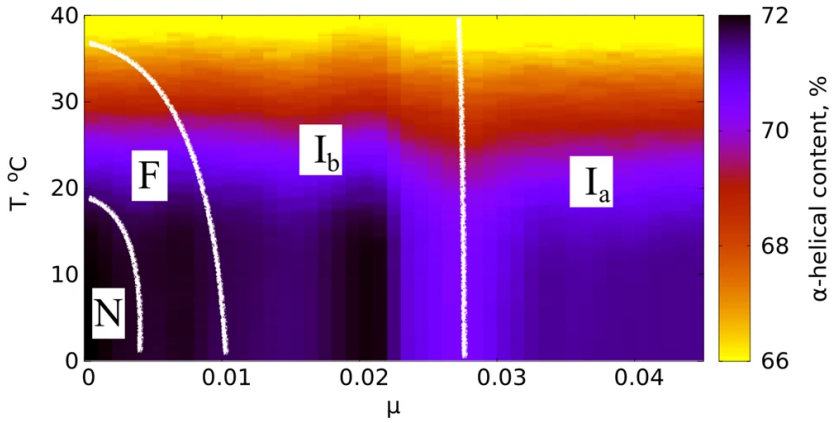

Figure A.7: The phase diagram in terms of the observable Q_α that counts the relative number of residues in α-helical posture, at low temperatures $T < 40$℃. This figure has been taken from the work from A. Begun et. al, Protein tertiary structure and the myoglobin phase diagram, Scientific Reports vol. 9 (2019), 10819.

on μ, even though we do note a slight change in the overall stability of helix-F even at relatively small μ values. We conclude that at low temperatures the increase of μ appears to have a stronger influence on loops than on helices. In particular, the ligand transport mechanism if indeed associated with instability in helix-F, appears to engage the adjacent loop structures as well.

The results in Figure A.7 are consistent with room temperature CD helicity measurements that report only minor signal variations for pH values above ~ 4.523: Acidity does not have a strong effect on the hydrogen bonds that stabilize the helical structures. In the Figure we identify the transition between I_b and I_a, in terms of a region with slightly decreased value of Q_α. It is also notable that right prior to the transition, there is region in I_b with an enhanced Q_α values.

In summary, we have proposed to model protein thermodynamics directly at the tertiary level of structures, in terms of the multi-soliton solution of the DNLS equation. We have numerically evaluated the ensuing grand canonical partition function at finite temperature and chemical potential, with the latter identified by comparison with the Henderson-Hasselbalch equation. As an example we have constructed the (T, pH) phase diagram of myoglobin. All our results are in a good agreement with experimental observations. In particular, the ordering of helix stabilization and the emergence of two molten globules are qualitatively in full agreement with experimental observations. Furthermore, we observe that the F-helix with its proximal histidine, is the first to loose stability as either temperature or acidity increase from neutral values. This supports that the destabilization of the F-helix region might have a pivotal role for ligand entry and exit. We have also made predictions for future experiments, in particular we have proposed that at high temperatures near $T = 80$℃ there is an apparent tricritical point where the two molten globules come together with the random coil phase. Our results show that effective theories that model protein structure directly at the tertiary structure level, can provide a viable computational approach to investigate the phase

structure of complex globular proteins.

A.5 Topology and knotty entanglement in protein folding

Here we propose to introduce topological techniques to study protein folding and dynamics, where thus far these techniques have been used only sparsely. As an example we analyze the formation of knots and self-entanglement in protein folding. A knot along a protein backbone is a delocalized structure, with a definite topological character. A knot can not be removed by any small amplitude local motion such as twisting, bending or crumpling of the protein backbone. A knotty self-entanglement persists as long as there is no backbone chain crossing, and provided the C and N terminals of the protein are not circumnavigated.

We start and construct a multi-soliton that models the three-dimensional C_α backbone of the folded AFV3-109 protein as a solution of the generalized DNLS equation. We use the crystallographic Protein Data Bank (PDB) structure with PDB code 2J6B [125] as a decoy. The AFV3-109 is an α/β protein that, when folded, supports a self-entangled structure akin the shoelace slipknot. Even though the slipknot is technically not a proper knot, it has nevertheless a topological character, with a large degree of structural stability under local backbone deformations; the topological character of the slipknotted AFV3-109 is similar to that encountered in other, more elaborately self-entangled knotty proteins [126–129]. Moreover, our simulation results reveal that in the case of the AFV3-109 protein, the formation of the slipknot entails a trefoil knot as a folding intermediate. The AFV3-109 protein has been studied previously as a prototype example of a slipknotted protein [125, 126], but these previous simulations have not reported of an intermediate trefoil structure. On the contrary, it is presumed that a slipknot itself occurs as an intermediate, along the folding pathway of more complex knot formation, including a trefoil [126–129].

The Protein Data Bank structure 2J6B that we use as a decoy for constructing the multi-soliton solution has 109 amino acids. The core of this α/β protein consists of a β-sheet with five β-strands that are connected by helices and loops. The residues 78-106 make up a looped segment that is threaded into a slipknot through a knotting loop that consists of residues 8-77: The Figure A.8 shows the slipknot structure

We have constructed the multi-soliton that describes the C_α backbone of 2J6B as a minimum energy critical point of the mechanical free energy (A.38). According to [125] there are 3 helical and 5 strand-like regular segments in the crystallographic structure. Thus, including the C and N terminals, there are at least 9 individual loops along the relatively short backbone This suggests us to start and introduce a division of the C_α backbone into 9 individual solitons. However, a scrutiny of the crystallographic 2J6B structure reveals that it has a more complex geometry. There are relatively long loops between residues 6-18, 57-74 and 81-91, and some of the β-strands are slightly bent. In order to describe the backbone with a precision that is comparable to the resolution of the crystallographic structure we then

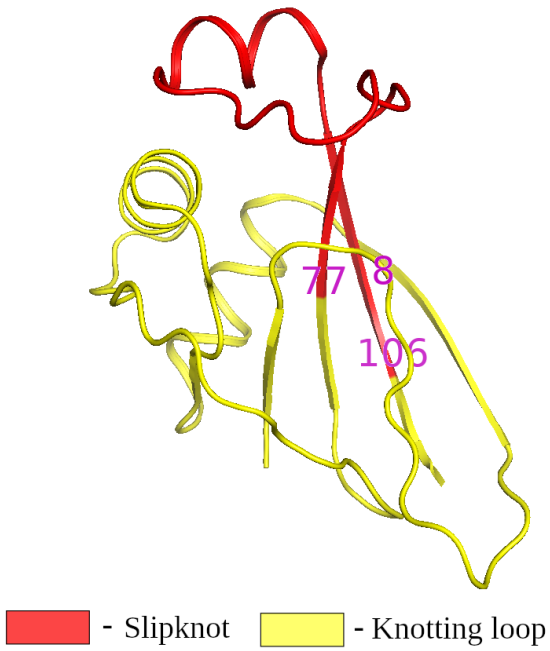

Figure A.8: A 3D view of the AFV3-109 (PDB code 2J6B), the yellow knotting loop extends over residues 8-77 and the red threaded slipknot consists of residues 78-106. This figure has been taken from the work from A. Begun et. al, On topology and knotty entanglement in protein folding, PLOS ONE 16(1) (2021), e0244547.

introduce additional soliton structures: we identify a total of 20 individual soliton profiles, with the long loops comprising more than a single soliton each and the β-strands supporting a soliton that accounts for their bending. In the S1 File we present the parameter values of the free energy function (A.38) that supports the multi-soliton solution as its energy minimum. The Figure A.9 panels (a) and (b) summarizes the multi-soliton model we have constructed. Figure A.9 (a) shows an overlay comparison between the C_α trace of the PDB structure 2J6B and its multi-soliton model. The root-meansquare-distance (RMSD) between the two is 1,23 Å, comparable with the reported resolution 1.3 Å of the experimental structure. Figure A.9 (b) shows a comparison of the C_α trace bond angles (A.21a) and torsion angles (A.21b) between the PDB structure and its multi-soliton model.

Figure A.10 show our results for a particular heating and cooling simulation. The heating always starts from the multi-soliton that models 2J6B; the folding events we observe are fully reversible. The solid lines in the Figure A.10 denote the evolution of the mean value over all structures in the simulated ensemble. The spread around each solid line shows the extent of one standard deviation around the mean. We note that in the high temperature stage we have random structures that reside in the phase of a self-avoiding random walk, with no regular structural details and in particular no structural resemblance to the folded conformation.

The lower horizontal axis in the Figure A.10 gives the logarithmic value of the temperature factor $\beta = T_G^{-1}$ during the simulation. The upper horizontal axis gives a corresponding Celsius value, that we deduce from a comparison with myoglobin simulations in [130]; the

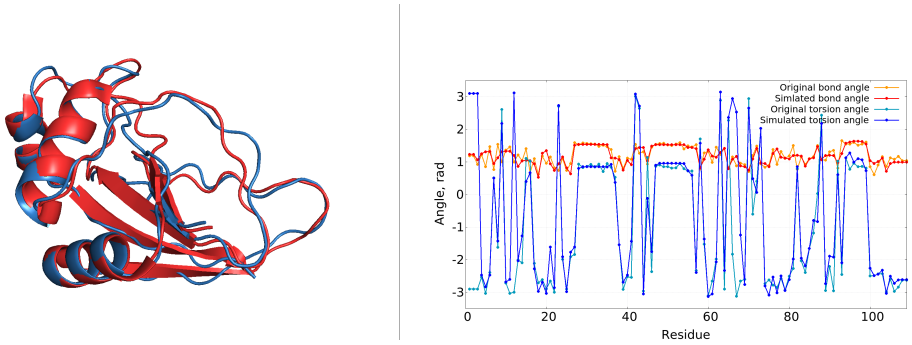

(a) (b)

Figure A.9: Multi-soliton model summarizing. Panel (a) shown overlay comparison of PDB structure 2J6B (red) and its multi-soliton structure (blue). The RMS distance between the two structures is 1.23 Å. Panel (b) shows the virtual C_α trace bond and torsion angles, for the PDB structure 2J6B and for its multi-soliton model. This figure has been taken from the work from A. Begun et. al, On topology and knotty entanglement in protein folding, PLOS ONE 16(1) (2021), e0244547.

Celsius value should not be taken literally, it is intended to be suggestive, and for an accurate comparison between the simulation temperature and the corresponding Celsius value additional folding and unfolding experiments need to be performed over an extended range of temperature values. For a detailed analysis how to derive a relation between the temperature factor β and the physiological temperature value measured in Celsius, we refer to [109].

In the Figure A.10 (c) we show the evolution of R_g at low temperatures, during the very early stages of the heating simulation. We observe a very slight but systematic initial decrease in the R_g value. This means that when the chain starts unknotting, its effective volume initially shrinks, before the chain then expands and unfolds: The initial slipknotted multi-soliton structure appears to be (slightly) swelled in comparison to an unknotted but collapsed structure, even though the free energy of the slipknot has a lower value. As shown in Figure A.10 (d) we observe a corresponding, systematic but very small increase of R_g i.e. swelling at the end of the cooling period, before the energy minimum is reached.

Even though the swelling is very small in terms of the radius of gyration value R_g, at the visual level of the structure the effect is much more clear. The Fig 4 shows a structure at the minimal value of R_g together with the fully folded conformation; the configuration with minimal R_g value appears more compact.

A swelling that is caused by knottiness has been previously reported in an analysis of knotted crystallographic PDB structures [131]

We have analyzed the folding and unfolding transitions by following the temperature dependent fluctuations $\Delta\tau$ in the values of the torsion angle (A.21b). In terms of $\Delta\tau$ the initial unfolding process appears to start at the location of the β-bridge that is centered at the proline with PDB residue number 61. In Figure A.12 (a) we show how initially, at very low temperature values, the amplitude of the thermal fluctuations $\Delta\tau(61)$ slowly increases. This increase coincides with the decrease in the radius of gyration R_g shown in Figure A.10

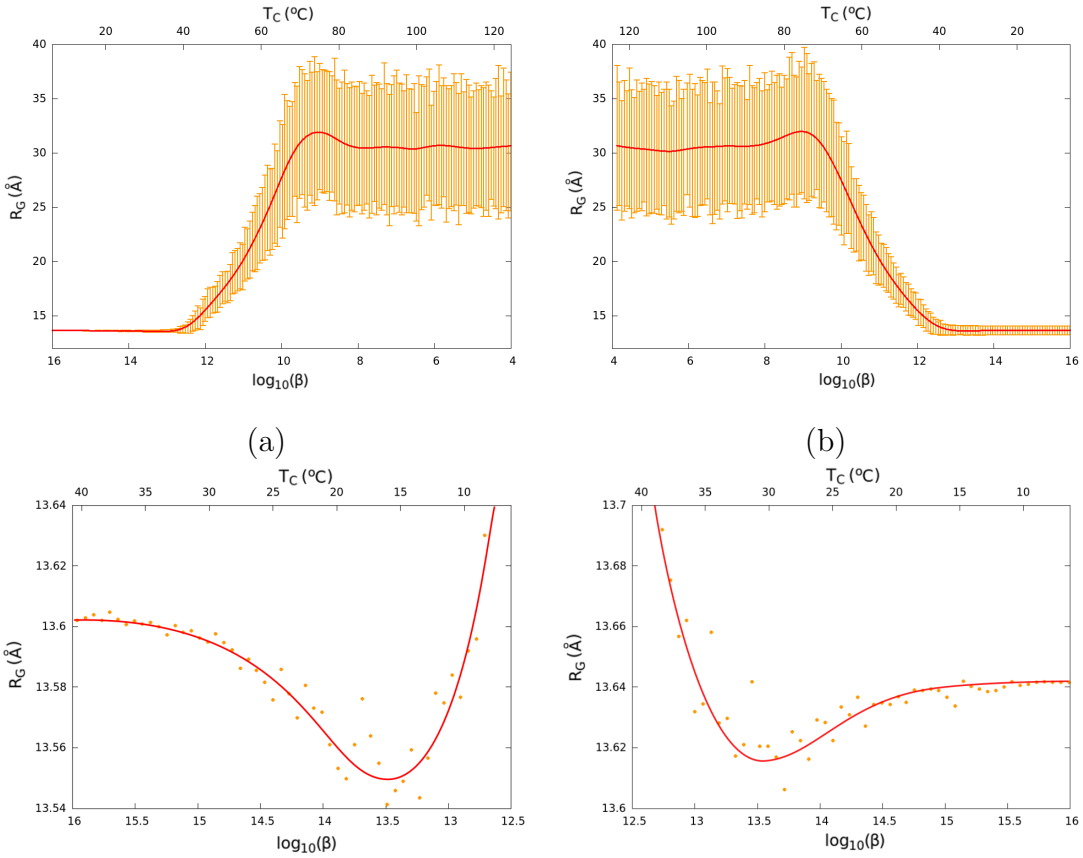

Figure A.10: Panel (a) shows the evolution of radius of gyration R_g of the multi-soliton during the heating stage, and Panel (b) shows the R_g evolution during the cooling stage. The solid line shows the mean value of the simulation ensemble that consist of 1.000 independent cycles, and the spread denotes one standard deviation. Panels (c) and (d) are close looks to the R_g values, at early/late stages of heating/cooling. This figure has been taken from the work from A. Begun et. al, On topology and knotty entanglement in protein folding, PLOS ONE 16(1) (2021), e0244547.



(a) (b)

Figure A.11: The Panel (a) shows the native folded conformation, and the Panel (b) shows the conformation with the minimal R_g value. This figure has been taken from the work from A. Begun et. al, On topology and knotty entanglement in protein folding, PLOS ONE 16(1) (2021), e0244547.

(c) and at the same time we observe that the slipknot starts opening. When the temperature factor reaches a value $\log_1 0\beta \approx 13.0$ we observe a sharp order-disorder transition in the fluctuation amplitude $\Delta\tau(61)$. At this β-value the slipknot opens, and becomes converted into a trefoil knot shown in Figure A.12 (b). When the temperature factor further increases, the trefoil unknots and the chain starts unfolding, with a rapid, sharp increase in the radius of gyration value R_g as shown in Figure A.10 (c).

The folding transition proceeds similarly but in the opposite direction, the slipknot forms through an intermediate trefoil knot.

Previous authors have investigated the folding of knotted proteins, mostly using different variants of C_α structure based Go models. These authors do not report on trefoil knot folding intermediate, but they report significant difficulties in reaching the natively folded knotty conformation. Apparently, a knotted fold either does not appear at all [132] without the help of funneling or other kind of augmentation during the folding process, or then it occurs only very rarely, in about 1-2% of folding simulations [126] (2.8% in the case of AFV3-109 [126]). We have performed a series of folding and unfolding simulations under different conditions and Figure A.13 summarizes our results: When cooling proceeds very quickly the relative number of slipknots is small. However, when the cooling process becomes progressively slower, the number of slipknotted final conformations increases rapidly and as shown in the Figure A.13 we reach around 98 percent success rate in the long and slow cooling simulations that we have performed. Thus we conclude that the slipknotted AFV3-109 is a

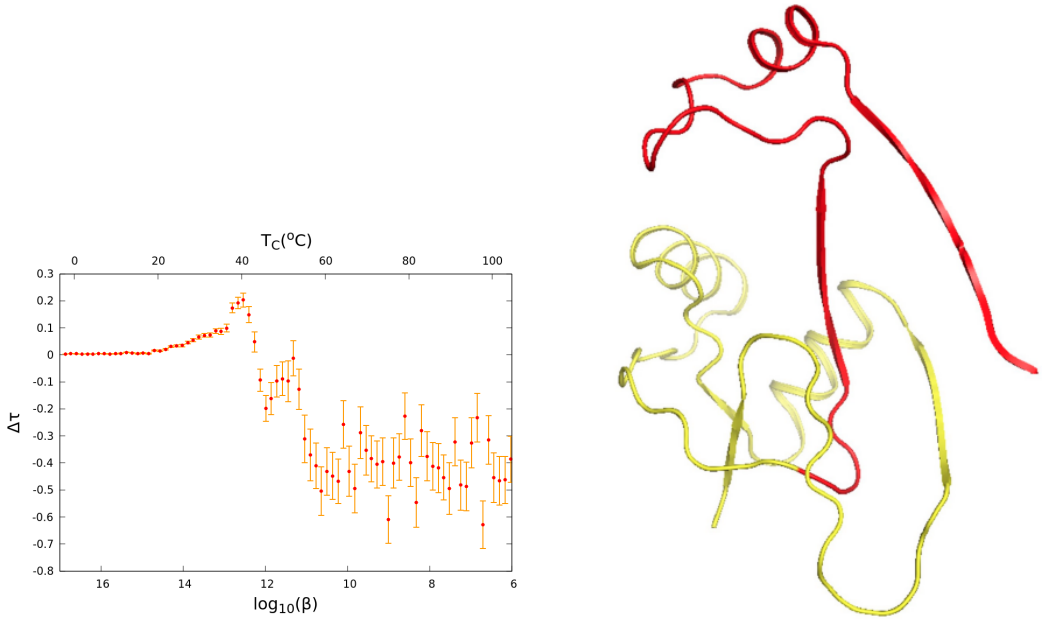

(a) (b)

Figure A.12: The Panel (a) shows the initial increase in the thermal fluctuations $\Delta\tau_{61}$ of the torsion angle located at the proline with residue number 61 (the mean value of τ_{61} and its one standard deviation at the given $\log_{10}(\beta)$ value). The peak that is visible at $\log_{10}(\beta)13 - 12.5$ identifies the β-values where we observe an intermediate trefoil knot. The Panel (b) shows the trefoil knot folding intermediate identified in the Panel (a). The Panel shows that the trefoil knot forms, when the C-terminal of the looped segment pulls out from the knotting loop. This figure has been taken from the work from A. Begun et. al, On topology and knotty entanglement in protein folding, PLOS ONE 16(1) (2021), e0244547.

slow folder [133, 134], proceeding through a trefoil knot folding intermediate. Moreover, since we observe both a trefoil knot folding intermediate and a light swelling at the final stages, the folding of AFV3-109 is not a pure relaxation (Arrhenius) process [135].

We have developed a global technique that is rooted on topological concepts, to analyze and describe the formation of topological structures in proteins, in particular aspects of knottiness and self-entanglement. For this, we have modeled the entire C_α backbone of a protein in terms of a single topological multi-soliton entity; the multi-soliton describes the minimum of a mechanical free energy. As a case study, we have investigated the folding and unfolding of the slipknotted AFV3-109 protein, instigated by variable ambient temperature, using powerful state-of-art Monte Carlo techniques of non-equilibrium thermodynamics. We have found that the multi-soliton describes the formation of the slipknot very accurately, and we are able to describe the folding pathways and make predictions on the physical origin of knot formation. In paricular, we have been able to observe a trefoil knot as a folding intermediate. Our results demonstrate the value of developing global approaches to protein folding and dynamics; global approaches are highly accurate, and even though they may lack

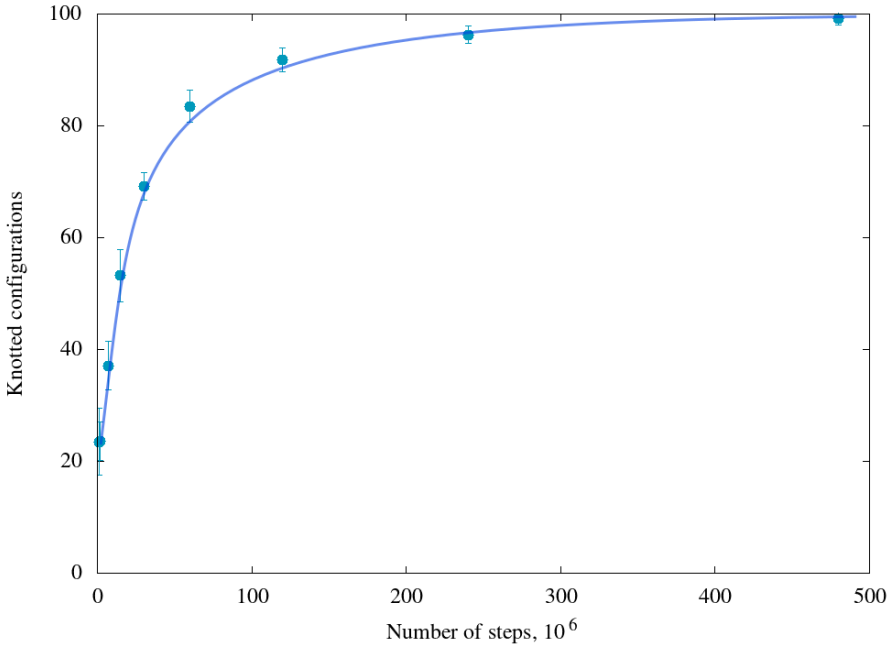

Figure A.13: Shows the relative number (in percentage) of slipknotted structures in the final folded ensemble, as a function of Monte Carlo steps after one full heating-cooling cycle.

in atomic level details they appear to correctly capture the global, topological aspects of self-entanglement during protein folding and dynamics.

Appendix B

Technical details of protein modelling

B.1 Building of protein's soliton structure

Data files from the PDB database [136] are used as a basis for constructing a soliton structure. From this file, the Cartesian coordinates of the C_α atoms are extracted and converted into the Frenet coordinates. Further, by analyzing the angles of curvature and torsion, the coordinates of the ends of the solitons, as well as their centers, are arranged; the subsequent work is carried out both with each soliton separately and with the entire sequence as a whole.

To search for energy minima in this problem, the standard gradient descent algorithm is not applicable, since there are local minima at which the solution can stop. Therefore, the software package uses the simulating annealing algorithm that allows one to filter out local minima.

The complete simulated annealing algorithm consists of the following steps:

1. The value of the function under investigation is calculated.

2. The current value of the function under investigation is compared with the smallest one found earlier; if the current value is less, then the current configuration is accepted, if it is greater, then the configuration is accepted in accordance with the Metropolis condition.

3. According to a certain law, the temperature decreases (the choice of the law of temperature change depends on the specific problem).

4. A new configuration is randomly generated.

5. If the final temperature is reached, the algorithm stops, otherwise go to point 1

The algorithm was slightly changed due to the specifics of the problem. The coefficients $a, b, c, d, \lambda_{1,2}, m_{1,2}$ of each soliton are selected as free parameters that define the configuration. The investigated function is not the energy of the string, but three functions characterizing

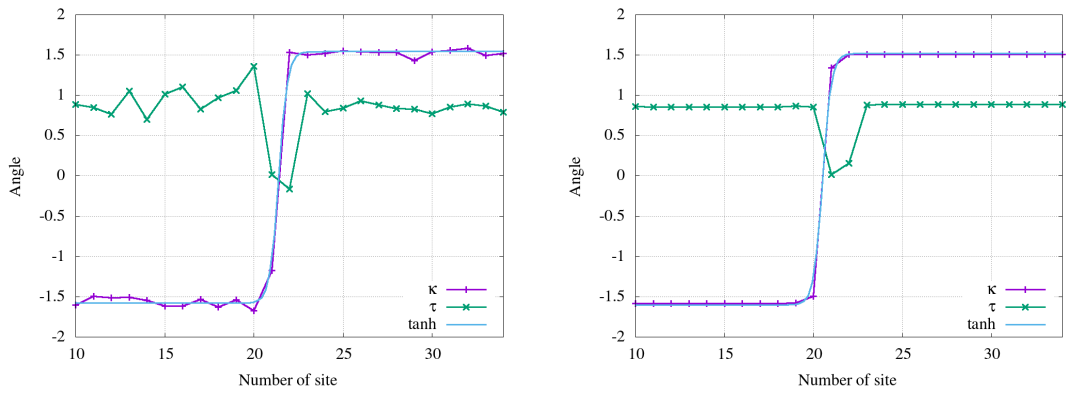

(a) (b)

Figure B.1: The graphs of Frenet coordinates of a part of myoglobin 1ABS. Panel (a) stands for PDB data, panel (b) stands for soliton structure

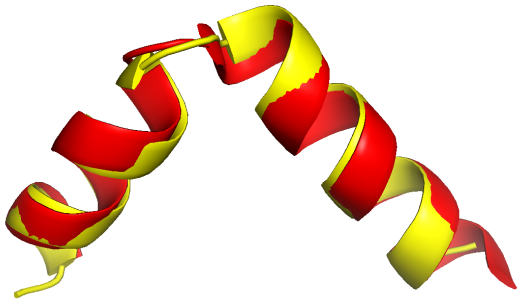

Figure B.2: Superposition of experimental (red) and soliton (yellow) protein models.

the deviation of the current configuration from the experimentally obtained one:

$$F_1 = \sum_{i=0}^{N} \sin^2(\kappa_i - \kappa_i^0), \tag{B.1}$$

$$F_2 = \sum_{i=0}^{N} \sin^2(\tau_i - \tau_i^0), \tag{B.2}$$

$$F_3 = \sqrt{\frac{1}{N} \sum_{i=0}^{N} \delta_i^2}, \tag{B.3}$$

where κ_i^0 and τ_i^0 are the angles of curvature and torsion obtained from the experimental data, respectively. In this case, configurations are generated in such a way as to minimize energy for given random parameters. The stable state is characterized by the minimum values of the observed functions.

Figure B.1 shows a comparison of a region of a real protein and its soliton model. As can be seen from the graphs, the angles of curvature and torsion in the model are stable, and each spiral has its own values of these angles, which are constant throughout the spiral. Thus, the protein is presented as a set of idealized building blocks.

Figure B.2 shows the superposition of two 3-D models, one of which is based on experimental data, and the second is a soliton model.

B.2 Simulation of protein dynamics

Glauber's algorithm used to model protein dynamics consists of the following steps:

1. A fluctuation is introduced into the value of the angle of curvature or torsion at a random node according to the law

$$\tau_i' = \quad \tau_i + 1.5R \tag{B.4}$$

$$\kappa_i' = \quad \kappa_i + 0.015R \tag{B.5}$$

   where R is a random number generated with normal distribution with expected value 0 and variance 1.

2. New configuration is being checked for selfcrosses:

$$|r_i - r_j| < 3.8, \tag{B.6}$$

   If there is, reject changes and go back to point 1.

3. The change in the configuration energy is calculated:

$$\Delta E_\tau = -a(\tau_i' - \tau_i) - b\kappa_i^2(\tau_i' - \tau_i) + \frac{c}{2}(\tau_i'^2 - \tau_i^2) + \frac{d}{2}\kappa_i^2(\tau_i'^2 - \tau_i^2), \tag{B.7}$$

$$\begin{aligned}\Delta E_\kappa = 2(\kappa_i - \kappa_i')(\kappa_{i+1} + \kappa_{i-1}) + \lambda\big((\kappa_i'^2 - m^2)^2 - (\kappa_i^2 - m^2)^2\big) \\ -b\tau_i(\kappa_i'^2 - \kappa_i^2) + \frac{d}{2}\tau_i^2(\kappa_i'^2 - \kappa_i^2).\end{aligned} \tag{B.8}$$

4. New configuration is accepted with a probability

$$P = \frac{e^{-\Delta E/T}}{1 + e^{-\Delta E/T_G}} \tag{B.9}$$

5. Temperature slightly changes by a small fixed step

6. If target temperature is reached algorithm stops, else go to point 1.

The dynamics of all proteins was simulated starting from the temperature $T_G = 10^{-17}$, followed by heating to the temperature $T_G = 10^{-4}$. After that, the protein was thermalized and cooled to the initial temperature.

As follows from the (B.9) equation, configurations in which the energy increases by more than the temperature value will be suppressed. Therefore, the contribution of thermal curvature fluctuations at low temperatures is very small.

The simulation algorithm consists of three stages; heating, thermalization and cooling. After each step we change the value of T_G, by multiplying it with a constant, and the value of the constant determines the rate of heating/cooling. During the high temperature thermalization stage the number of Monte Carlo steps is always fixed to 7×106 steps and in this stage the value of T_G remains constant. During heating and cooling the number of steps can be variable and in the simulation described here we have $480 * 10^6$ steps.

Bibliography

[1] Carl M. Bender and Stefan Boettcher. "Real Spectra in Non-Hermitian Hamiltonians Having $\mathcal{PT}$ Symmetry". In: *Phys.Rev.Lett. 80 (1998) 5243-5246* (Nov. 29, 1997). DOI: 10.1103/PhysRevLett.80.5243. arXiv: physics/9712001v3 [math-ph].

[2] C. M. Bender. "Introduction to PT-Symmetric Quantum Theory". In: *Contemporary Physics* 46.4 (July 2005), pp. 277–292. DOI: 10.1080/00107500072632. arXiv: quant-ph/0501052.

[3] A. Mostafazadeh. "Pseudo-Hermiticity versus PT symmetry. The necessary condition for the reality of the spectrum". In: *Journal of Mathematical Physics* 43.1 (Jan. 2002), pp. 205–214. DOI: 10.1063/1.1418246. arXiv: math-ph/0107001.

[4] E. Caliceti, S. Graffi, and M. Maioli. "Perturbation theory of odd anharmonic oscillators". English. In: *Communications in Mathematical Physics* 75.1 (July 1980), pp. 51–66. ISSN: 0010-3616. DOI: 10.1007/BF01962591.

[5] A. A. Andrianov. "The large N expansion as a local perturbation theory". In: 140 (1982), pp. 82–100. ISSN: 0003-4916. DOI: 10.1016/0003-4916(82)90336-0.

[6] Timothy Hollowood. "Solitons in affine Toda field theories". In: *Nuclear Physics B* 384.3 (Oct. 1992), pp. 523–540. ISSN: 0550-3213. DOI: 10.1016/0550-3213(92)90579-z.

[7] F. G. Scholtz, H. B. Geyer, and F. J. W. Hahne. "Quasi-Hermitian operators in quantum mechanics and the variational principle". In: *Annals of Physics* 213.1 (Jan. 1992), pp. 74–101. ISSN: 0003-4916. DOI: 10.1016/0003-4916(92)90284-s.

[8] Carl M. Bender et al. "Variational ansatz for $\mathcal{PT}$-symmetric quantum mechanics". In: *Physics Letters A* 259.3-4 (Aug. 1999), pp. 224–231. ISSN: 0375-9601. DOI: 10.1016/s0375-9601(99)00468-5.

[9] Carl M. Bender, Dorje C. Brody, and Hugh F. Jones. "Complex Extension of Quantum Mechanics". In: *EconfC0306234:617-628,2003; Phys.Rev.Lett.89:270401,2002; Erratum-ibid.92:119902,2004* (Aug. 12, 2002). DOI: 10.1103/PhysRevLett.89.270401. arXiv: quant-ph/0208076v2 [quant-ph].

[10] Tommy Ohlsson and Shun Zhou. "Transition Probabilities in the Two-Level Quantum System with PT-Symmetric Non-Hermitian Hamiltonians". In: *J. Math. Phys.* 61.5 (2020), p. 052104. DOI: 10.1063/5.0002958. arXiv: 1906.01567 [quant-ph].

[11] Tommy Ohlsson and Shun Zhou. "Density Matrix Formalism for PT-Symmetric Non-Hermitian Hamiltonians with the Lindblad Equation". In: *Phys. Rev. A* 103.2 (2021), p. 022218. DOI: 10.1103/PhysRevA.103.022218. arXiv: 2006.02445 [quant-ph].

[12] J. Alexandre, J. Ellis, and P. Millington. "Discrete spacetime symmetries and particle mixing in non-Hermitian scalar quantum field theories". In: *Physical Review D* 102.12 (Dec. 2020), p. 125030. DOI: 10.1103/physrevd.102.125030. arXiv: 2006.06656.

[13] Stefano Longhi. "Optical Realization of Relativistic Non-Hermitian Quantum Mechanics". In: *Physical Review Letters* 105.1 (June 2010), p. 013903. ISSN: 0031-9007. DOI: 10.1103/physrevlett.105.013903.

[14] A. Guo et al. "Observation of $\mathcal{PT}$-Symmetry Breaking in Complex Optical Potentials". In: *Physical Review Letters* 103.9 (Aug. 2009), p. 093902. ISSN: 0031-9007. DOI: 10.1103/physrevlett.103.093902.

[15] C. E. Rüter et al. "Observation of Parity-Time Symmetry in Optical Systems". In: *Optics and Photonics News* 21.12 (Dec. 2010), p. 47. ISSN: 1047-6938. DOI: 10.1364/opn.21.12.000047.

[16] Tsampikos Kottos. "Broken symmetry makes light work". In: *Nature Physics* 6.3 (Mar. 2010), pp. 166–167. ISSN: 1745-2473. DOI: 10.1038/nphys1612.

[17] Ramy El-Ganainy et al. "Non-Hermitian physics and $\mathcal{PT}$ symmetry". In: *Nature Physics* 14.1 (Jan. 2018), pp. 11–19. ISSN: 1745-2473. DOI: 10.1038/nphys4323.

[18] Ramy El-Ganainy et al. "The dawn of non-Hermitian optics". In: *Communications Physics* 2.1 (Mar. 2019). ISSN: 2399-3650. DOI: 10.1038/s42005-019-0130-z.

[19] Liang Feng, Ramy El-Ganainy, and Li Ge. "Non-Hermitian photonics based on parity–time symmetry". In: *Nature Photonics* 11.12 (Nov. 2017), pp. 752–762. ISSN: 1749-4885. DOI: 10.1038/s41566-017-0031-1.

[20] R. El-Ganainy et al. "Theory of coupled optical $\mathcal{PT}$-symmetric structures". In: *Optics Letters* 32.17 (Aug. 2007), p. 2632. ISSN: 0146-9592. DOI: 10.1364/ol.32.002632.

[21] Konstantinos G. Makris et al. "$\mathcal{PT}$-symmetric optical lattices". In: *Physical Review A* 81.6 (June 2010), p. 063807. ISSN: 1050-2947. DOI: 10.1103/physreva.81.063807.

[22] K. G. Makris et al. "$\mathcal{PT}$ -Symmetric Periodic Optical Potentials". In: *International Journal of Theoretical Physics* 50.4 (Feb. 2011), pp. 1019–1041. ISSN: 0020-7748. DOI: 10.1007/s10773-010-0625-6.

[23] S. Longhi. "Quantum-optical analogies using photonic structures". In: *Laser & Photonics Review* 3.3 (Apr. 2009), pp. 243–261. ISSN: 1863-8880. DOI: 10.1002/lpor.200810055.

[24] J. Rubinstein, P. Sternberg, and Q. Ma. "Bifurcation Diagram and Pattern Formation of Phase Slip Centers in Superconducting Wires Driven with Electric Currents". In: *Physical Review Letters* 99.16 (Oct. 2007), p. 167003. ISSN: 0031-9007. DOI: 10.1103/physrevlett.99.167003.

[25] N. M. Chtchelkatchev et al. "Stimulation of the Fluctuation Superconductivity by $\mathcal{PT}$ Symmetry". In: *Physical Review Letters* 109.15 (Oct. 2012), p. 150405. ISSN: 0031-9007. DOI: 10.1103/physrevlett.109.150405.

[26] Joseph Schindler et al. "Experimental study of active *LRC* circuits with $\mathcal{PT}$ symmetries". In: *Physical Review A* 84.4 (Oct. 2011), p. 040101. DOI: 10.1103/PhysRevA.84.040101.

[27] C. M. Bender, H. F. Jones, and R. J. Rivers. "Dual PT-symmetric quantum field theories". In: *Phys. Lett. B* 625.3-4 (Oct. 2005), pp. 333–340. DOI: 10.1016/j.physletb.2005.08.087. arXiv: hep-th/0508105.

[28] Miloslav Znojil. "Hermitian–Non-Hermitian Interfaces in Quantum Theory". In: *Advances in High Energy Physics* 2018 (2018), pp. 1–12. ISSN: 1687-7357. DOI: 10.1155/2018/7906536.

[29] Andreas Fring and Thomas Frith. "Eternal life of entropy in non-Hermitian quantum systems". In: *Physical Review A* 100.1 (July 2019), p. 010102. ISSN: 2469-9926. DOI: 10.1103/physreva.100.010102.

[30] Alexander Yu. Korchin and Vladimir A. Kovalchuk. "Decay of the Higgs boson to $\tau^-\tau^+$ and non-Hermiticy of the Yukawa interaction". In: *Physical Review D* 94.7 (Oct. 2016), p. 076003. ISSN: 2470-0010. DOI: 10.1103/physrevd.94.076003.

[31] K. G. Makris et al. "Beam Dynamics inPTSymmetric Optical Lattices". In: *Physical Review Letters* 100.10 (Mar. 2008), p. 103904. DOI: 10.1103/physrevlett.100.103904.

[32] Henning Schomerus. "Quantum Noise and Self-Sustained Radiation of $\mathcal{PT}$-Symmetric Systems". In: *Physical Review Letters* 104.23 (June 2010), p. 233601. DOI: 10.1103/PhysRevLett.104.233601.

[33] Ali Mostafazadeh. "Spectral Singularities of Complex Scattering Potentials and Infinite Reflection and Transmission Coefficients at Real Energies". In: *Physical Review Letters* 102.22 (June 2009), p. 220402. DOI: 10.1103/PhysRevLett.102.220402.

[34] Miguel Simón, Álvaro Buendía, and J. Muga. "Symmetries and invariants for non-Hermitian Hamiltonians". In: *Mathematics* 6.7 (June 2018), p. 111. ISSN: 2227-7390. DOI: 10.3390/math6070111.

[35] M. P. Blencowe, H. F. Jones, and A. P. Korte. "Applying the linear δ expansion to the $i\phi^3$ interaction". In: *Physical Review D* 57.8 (Apr. 1998), pp. 5092–5099. ISSN: 0556-2821. DOI: 10.1103/physrevd.57.5092.

[36] Carl M. Bender, Dorje C. Brody, and Hugh F. Jones. "Scalar Quantum Field Theory with a Complex Cubic Interaction". In: *Physical Review Letters* 93.25 (Dec. 2004), p. 251601. ISSN: 0031-9007. DOI: 10.1103/physrevlett.93.251601.

[37] Carl M. Bender, Vincenzo Branchina, and Emanuele Messina. "Ordinary versus PT-symmetric ϕ^3 quantum field theory". In: *Physical Review D* 85.8 (Apr. 2012), p. 085001. ISSN: 1550-7998. DOI: 10.1103/physrevd.85.085001.

[38] Carl M. Bender, V. Branchina, and Emanuele Messina. "Critical behavior of the PT-symmetric $i\phi^3$ quantum field theory". In: *Physical Review D* 87.8 (Apr. 2013), p. 085029. ISSN: 1550-7998. DOI: 10.1103/physrevd.87.085029.

[39] Abouzeid M. Shalaby. "Vacuum structure and $\mathcal{PT}$ -symmetry breaking of the non-Hermetian ($i\phi^3$) theory". In: *Physical Review D* 96.2 (July 2017), p. 025015. ISSN: 2470-0010. DOI: 10.1103/physrevd.96.025015.

[40] Abouzeid Shalaby and Suleiman S. Al-Thoyaib. "Nonperturbative tests for asymptotic freedom in the $\mathcal{PT}$-symmetric $(-\phi^4)_{3+1}$ theory". In: *Physical Review D* 82.8 (Oct. 2010), p. 085013. ISSN: 1550-7998. DOI: 10.1103/physrevd.82.085013.

[41] Carl M. Bender et al. "$\mathcal{PT}$-symmetric interpretation of unstable effective potentials". In: *Journal of Physics A: Mathematical and Theoretical* 49.45 (Oct. 2016), 45LT01. ISSN: 1751-8113. DOI: 10.1088/1751-8113/49/45/45lt01.

[42] Carl M. Bender, H.F. Jones, and R.J. Rivers. "Dual $\mathcal{PT}$-symmetric quantum field theories". In: *Physics Letters B* 625.3-4 (Oct. 2005), pp. 333–340. DOI: 10.1016/j.physletb.2005.08.087.

[43] Jean Alexandre and Carl M. Bender. "Foldy-Wouthuysen transformation for non-Hermitian Hamiltonians". In: *Journal of Physics A: Mathematical and Theoretical* 48.18 (Apr. 2015), p. 185403. ISSN: 1751-8113. DOI: 10.1088/1751-8113/48/18/185403.

[44] Jean Alexandre, Carl M. Bender, and Peter Millington. "Non-Hermitian extension of gauge theories and implications for neutrino physics". In: *Journal of High Energy Physics* 2015.11 (Nov. 2015). ISSN: 1029-8479. DOI: 10.1007/jhep11(2015)111.

[45] M. N. Chernodub. "The Nielsen-Ninomiya theorem, $\mathcal{PT}$-invariant non-Hermiticity and single 8-shaped Dirac cone". In: *Journal of Physics A: Mathematical and Theoretical* 50.38 (Aug. 2017), p. 385001. ISSN: 1751-8113. DOI: 10.1088/1751-8121/aa809a.

[46] Katherine Jones-Smith and Harsh Mathur. "Relativistic Non-Hermitian Quantum Mechanics". In: *Phys. Rev. D* 89.12 (2014), p. 125014. DOI: 10.1103/PhysRevD.89.125014. arXiv: 0908.4257 [hep-th].

[47] Tommy Ohlsson. "Non-Hermitian neutrino oscillations in matter with PT symmetric Hamiltonians". In: *EPL* 113.6 (2016), p. 61001. DOI: 10.1209/0295-5075/113/61001. arXiv: 1509.06452 [hep-ph].

[48] V. N. Rodionov, A. M. Mandel, and G. A. Kravtsova. "Restriction of the Fermion Mass Spectrum in $\mathcal{PT}$-Symmetric Systems and its Implications For Studying Dark Matter". In: *Theoretical and Mathematical Physics* 198.3 (Mar. 2019), pp. 412–424. ISSN: 0040-5779. DOI: 10.1134/s0040577919030061.

[49] J. Alexandre et al. "Gauge invariance and the Englert-Brout-Higgs mechanism in non-Hermitian field theories". In: *Physical Review D* 99.7 (Apr. 2019), p. 075024. DOI: 10.1103/PhysRevD.99.075024. arXiv: 1808.00944.

[50] Jean Alexandre et al. "Spontaneous symmetry breaking and the Goldstone theorem in non-Hermitian field theories". In: *Physical Review D* 98.4 (Aug. 2018), p. 045001. DOI: 10.1103/PhysRevD.98.045001. arXiv: 1805.06380.

[51] A. Fring and T. Taira. "Goldstone bosons in different PT-regimes of non-Hermitian scalar quantum field theories". In: *Nuclear Physics B* 950 (Jan. 2020), p. 114834. DOI: 10.1016/j.nuclphysb.2019.114834. arXiv: 1906.05738.

[52] A. Fring and T. Taira. "'t Hooft-Polyakov monopoles in non-Hermitian quantum field theory". In: *Physics Letters B* 807 (Aug. 2020), p. 135583. DOI: 10.1016/j.physletb.2020.135583. arXiv: 2006.02718.

[53] Francisco Correa, Andreas Fring, and Takanobu Taira. "Complex BPS Skyrmions with real energy". In: *Nuclear Physics B* 971 (Oct. 2021), p. 115516. ISSN: 0550-3213. DOI: 10.1016/j.nuclphysb.2021.115516.

[54] Andreas Fring and Takanobu Taira. "Non-Hermitian gauge field theories and BPS limits". In: (Mar. 2021). arXiv: 2103.13519 [hep-th].

[55] Carl M. Bender. "Introduction to $\mathcal{PT}$-Symmetric Quantum Theory". In: *Contemp.Phys.46:277-292,2005* (Jan. 11, 2005). DOI: 10.1080/00107500072632. arXiv: quant-ph/0501052v1 [quant-ph].

[56] E. Noether. "Invariante Variationsprobleme". ger. In: *Nachrichten von der Gesellschaft der Wissenschaften zu Göttingen, Mathematisch-Physikalische Klasse* 1918 (1918), pp. 235–257. URL: http://eudml.org/doc/59024.

[57] K.V. Stepanjantz. *Klassicheskaya teoriya polya*. 2009.

[58] J. Alexandre, P. Millington, and D. Seynaeve. "Symmetries and conservation laws in non-Hermitian field theories". In: *Physical Review D* 96.6 (Sept. 2017), p. 065027. DOI: 10.1103/PhysRevD.96.065027. arXiv: 1707.01057.

[59] Valery Rubakov. *Classical Theory of Gauge Fields*. Dec. 2009. DOI: 10.1515/9781400825097.

[60] J. Goldstone. "Field theories with « Superconductor » solutions". In: *Il Nuovo Cimento* 19.1 (Jan. 1961), pp. 154–164. ISSN: 0029-6341. DOI: 10.1007/bf02812722.

[61] Jeffrey Goldstone, Abdus Salam, and Steven Weinberg. "Broken Symmetries". In: *Physical Review* 127.3 (Aug. 1962), pp. 965–970. ISSN: 0031-899X. DOI: 10.1103/physrev.127.965.

[62] Yoichiro Nambu. "Axial Vector Current Conservation in Weak Interactions". In: *Physical Review Letters* 4.7 (Apr. 1960), pp. 380–382. ISSN: 0031-9007. DOI: 10.1103/physrevlett.4.380.

[63] Matthew D. Schwartz. *Quantum Field Theory and the Standard Model*. 2013. DOI: 10.1017/9781139540940.

[64] A. Zee. *Quantum Field Theory in a Nutshell*. 2010.

[65] P. D. Mannheim. "Goldstone bosons and the Englert-Brout-Higgs mechanism in non-Hermitian theories". In: *Physical Review D* 99.4 (Feb. 2019), p. 045006. DOI: 10.1103/PhysRevD.99.045006. arXiv: 1808.00437.

[66] Andreas Fring and Takanobu Taira. "Pseudo-Hermitian approach to Goldstone's theorem in non-Abelian non-Hermitian quantum field theories". In: *Phys. Rev. D* 101.4 (2020), p. 045014. DOI: 10.1103/PhysRevD.101.045014. arXiv: 1911.01405 [hep-th].

[67] A. Fring and T. Taira. *Massive gauge particles versus Goldstone bosons in non-Hermitian non-Abelian gauge theory.* [[hep-th]]. arXiv: 2004.00723.

[68] Jean Alexandre et al. "Spontaneously Breaking Non-Abelian Gauge Symmetry in Non-Hermitian Field Theories". In: *Physical Review D* 101.3 (Feb. 2020), p. 035008. DOI: 10.1103/PhysRevD.101.035008. arXiv: 1910.03985.

[69] H. B. Nielsen and P. Olesen. "Vortex-line models for dual strings". In: *Nuclear Physics B* 61 (Sept. 1973), pp. 45–61. ISSN: 0550-3213. DOI: 10.1016/0550-3213(73)90350-7.

[70] Lev Pitaevskii and Sandro Stringari. *Bose-Einstein Condensation and Superfluidity.* Oxford University Press, Jan. 2016. DOI: 10.1093/acprof:oso/9780198758884.001.0001.

[71] Lev P. Pitaevskii. "Bose-Einstein condensation in magnetic traps. Introduction to the theory". In: *Uspekhi Fizicheskih Nauk* 168.06 (June 1998), pp. 641–653. DOI: 10.3367/UFNr.0168.199806e.0641.

[72] E. P. Gross. "Structure of a quantized vortex in boson systems". In: *Il Nuovo Cimento* 20.3 (May 1961), pp. 454–477. ISSN: 0029-6341. DOI: 10.1007/bf02731494.

[73] L.P. Pitaevskii. "Vortex Lines in an Imperfect Bose Gas". In: *J. Exp. Theor. Phys.* 13.2 (1961), p. 451.

[74] F. Dalfovo and S. Stringari. "Bosons in anisotropic traps: Ground state and vortices". In: *Physical Review A* 53.4 (Apr. 1996), pp. 2477–2485. ISSN: 1050-2947. DOI: 10.1103/physreva.53.2477.

[75] M. H. Anderson et al. "Observation of Bose-Einstein Condensation in a Dilute Atomic Vapor". In: *Science* 269.5221 (July 1995), pp. 198–201. ISSN: 0036-8075. DOI: 10.1126/science.269.5221.198.

[76] Egor Babaev and Martin Speight. "Semi-Meissner state and neither type-I nor type-II superconductivity in multicomponent superconductors". In: *Physical Review B* 72.18 (Nov. 2005), p. 180502. ISSN: 1098-0121. DOI: 10.1103/physrevb.72.180502.

[77] V. Moshchalkov et al. "Type-1.5 Superconductors". In: *Physical Review Letters* 102.11 (Mar. 2009), p. 117001. DOI: 10.1103/PhysRevLett.102.117001.

[78] J. Carlstrom, J. Garaud, and E. Babaev. "Semi-Meissner state and non-pairwise intervortex interactions in type-1.5 superconductors". In: *Physical Review B* 84.13 (Oct. 2011), p. 134515. DOI: 10.1103/PhysRevB.84.134515. arXiv: 1101.4599.

[79] Lukas Schwarz et al. “Vortices in Bose-Einstein condensates with PT-symmetric gain and loss”. In: *Physical Review A* 95.5 (May 2017), p. 053613. DOI: 10.1103/PhysRevA.95.053613.

[80] K. Kasamatsu, M. Tsubota, and M. Ueda. “Vortices in multicomponent Bose-Einstein condensates”. In: *International Journal of Modern Physics B* 19.11 (Apr. 2005), p. 1835. DOI: 10.1142/S0217979205029602.

[81] M. M. Forbes and A. R. Zhitnitsky. “Global strings in high density QCD”. In: *Physical Review D* 65.8 (Mar. 2002), p. 085009. DOI: 10.1103/PhysRevD.65.085009. arXiv: hep-ph/0109173.

[82] D. B. Kaplan and S. Reddy. “Charged and superconducting vortices in dense quark matter”. In: *Physical Review Letters* 88.13 (Mar. 2002), p. 132302. DOI: 10.1103/PhysRevLett.88.132302. arXiv: hep-ph/0109256.

[83] L. D. Landau and E. M. Lifshitz. “Course of Theoretical Physics”. In: *Statistical Physics, Third Edition, Part* 1 (1980).

[84] H. Kleinert. *Gauge Fields in Condensed Matter. Vol. 1: Superflow and Vortex Lines (Disorder Fields, Phase Transitions)Vol. 2: Stresses and Defects (Differential Geometry, Crystal Melting)*. WORLD SCIENTIFIC, Mar. 1989. DOI: 10.1142/0356.

[85] D. T. Son and M. A. Stephanov. “Domain walls of relative phase in two-component Bose-Einstein condensates”. In: *Physical Review A* 65.6 (June 2002), p. 063621. DOI: 10.1103/physreva.65.063621.

[86] J. J. García-Ripoll, V. M. Pérez-García, and F. Sols. “Split vortices in optically coupled Bose-Einstein condensates”. In: *Physical Review A* 66.2 (Aug. 2002), p. 021602. DOI: 10.1103/PhysRevA.66.021602.

[87] M. Tylutki et al. “Confinement and precession of vortex pairs in coherently coupled Bose-Einstein condensates”. In: *Physical Review A* 93.4 (Apr. 2016), p. 043623. DOI: 10.1103/PhysRevA.93.043623.

[88] L. Calderaro et al. “Vortex dynamics in coherently coupled Bose-Einstein condensates”. In: *Physical Review A* 95.2 (Feb. 2017), p. 023605. DOI: 10.1103/PhysRevA.95.023605.

[89] A. Vilenkin and E. P. S. Shellard. “Cosmic strings and other topological defects”. In: *Cambridge University Pres* (2000). URL: https://www.amazon.com/Strings-Topological-Cambridge-Monographs-Mathematical/dp/0521654769.

[90] M. E. Peskin and D. V. Schroeder. “An Introduction To Quantum Field Theory”. In: *Avalon Publishing* (1995).

[91] M. A. Shifman. "Anomalies and Low-Energy Theorems of Quantum Chromodynamics". In: *Physics Reports* 32.6 (Dec. 1989), pp. 289–309. DOI: 10.1016/0370-1573(91)90020-M.

[92] D. T. Son, M. A. Stephanov, and A. R. Zhitnitsky. "Domain walls of high density QCD". In: *Physical Review Letters* 86.18 (Apr. 2001), pp. 3955–3958. DOI: 10.1103/PhysRevLett.86.3955. arXiv: hep-ph/0012041.

[93] P.L. Freddolino et al. "Challenges in protein-folding simulations". In: *Nature physics* 6.10 (2010), pp. 751–758.

[94] K.L. Larsen et al. "How fast-folding proteins fold". In: *Science* 334 (2011), pp. 517–520.

[95] Emilia A. Lubecka and A Liwo. "New UNRES force field package with fortran 90". In: *TASK Quarterly* 20.4 (2016), pp. 399–407.

[96] Tim J. P. Hubbard et al. "SCOP: a Structural Classification of Proteins database". In: *Nucleic Acids Research* (1997).

[97] A.J. Niemi. "Gauge fields, strings, solitons, anomalies, and the speed of life". In: *Theoretical and Mathematical Physics* 181 (2014), pp. 1235–1262.

[98] A.V. Molochkov, A.M. Begun, and A. Niemi. "Gauge symmetries and structure of proteins". In: *EPJ Web of Conferences* 1 (2017), pp. 174–182.

[99] X. Peng, A.K. Sieradzan, and A.J. Niemi. "Thermal unfolding of myoglobin in the Landau-Ginzburg-Wilson approach". In: *Phys. Rev. E* 94 (2016).

[100] L.H. Greene et al. "The CATH domain structure database: new protocols and classification levels give a more comprehensive resource for exploring evolution". In: *Nucleic Acids Research* 35 (2007), pp. D291–D297.

[101] A. Liwo et al. "A unified coarse-grained model of biological macromolecules based on mean-field multipole–multipole interactions". In: *J. Mol. Model.* 20 (2014), pp. 306–318.

[102] Christian B. Anfinsen. "Protein Structure." In: *Journal of the American Chemical Society* 84.13 (July 1962), pp. 2656–2656. ISSN: 0002-7863. DOI: 10.1021/ja00872a049.

[103] Christian B. Anfinsen. "Some observations on the basic principles of design in protein molecules". In: *Comparative Biochemistry and Physiology* 4.2-4 (Oct. 1962), pp. 229–240. ISSN: 0010-406X. DOI: 10.1016/0010-406x(62)90007-5.

[104] S. Hu et al. "Towards quantitative classification of folded proteins in terms of elementary functions". In: *Physical Review E* 83.4 (2010).

[105] S. Hu, M. Lundgren, and A.J. Niemi. "Solitons and Collapse in the lambda-repressor protein". In: *Physical review. E* 86.2 (2012).

[106] Ludwig D. Faddeev and Leon A. Takhtajan. *Hamiltonian Methods in the Theory of Solitons*. Springer Berlin Heidelberg, 1987. DOI: 10.1007/978-3-540-69969-9.

[107] M. J. Ablowitz, B. Prinari, and A. D. Trubatch. "Discrete and continuous nonlinear Schredinger systems". In: *Cambridge Univ. Press* (2004), p. 257.

[108] Maxim Chernodub, Shuangwei Hu, and Antti J. Niemi. "Topological solitons and folded proteins". In: *Physical Review E* 82.1 (July 2010), p. 011916. ISSN: 1539-3755. DOI: 10.1103/physreve.82.011916.

[109] Nora Molkenthin, Shuangwei Hu, and Antti J. Niemi. "Discrete Nonlinear Schrödinger Equation and Polygonal Solitons with Applications to Collapsed Proteins". In: *Physical Review Letters* 106.7 (Feb. 2011), p. 078102. DOI: 10.1103/PhysRevLett.106.078102.

[110] J. C. Kendrew et al. "A Three-Dimensional Model of the Myoglobin Molecule Obtained by X-Ray Analysis". In: *Nature* 181.4610 (Mar. 1958), pp. 662–666. ISSN: 0028-0836. DOI: 10.1038/181662a0.

[111] H. I. L. A. R. Y. MUIRHEAD and M. F. PERUTZ. "Structure Of Hæmoglobin: A Three-Dimensional Fourier Synthesis of Reduced Human Haemoglobin at 5.5 Å Resolution". In: 199.4894 (Aug. 1963), pp. 633–638. ISSN: 0028-0836. DOI: 10.1038/199633a0.

[112] J. C. KENDREW et al. "Structure of Myoglobin: A Three-Dimensional Fourier Synthesis at 2 Å. Resolution". In: 185.4711 (Feb. 1960), pp. 422–427. ISSN: 0028-0836. DOI: 10.1038/185422a0.

[113] R. Elber and M. Karplus. "Enhanced sampling in molecular dynamics: use of the time-dependent Hartree approximation for a simulation of carbon monoxide diffusion through myoglobin". In: *Journal of the American Chemical Society* 112.25 (Dec. 1990), pp. 9161–9175. ISSN: 0002-7863. DOI: 10.1021/ja00181a020.

[114] A. Krokhotin, Niemi A.J., and Peng X. "On the role of thermal backbone fluctuations in myoglobin ligand gate dynamics". In: *The Journal of Chemical Physics* 138 (2013), p. 175101. ISSN: 0021-9606. DOI: 10.1063/1.4801330.

[115] Marc Jamin and Robert L. Baldwin. "Two forms of the pH 4 folding intermediate of apomyoglobin 1 1Edited by P. E. Wright". In: *Journal of Molecular Biology* 276.2 (Feb. 1998), pp. 491–504. ISSN: 0022-2836. DOI: 10.1006/jmbi.1997.1543.

[116] Marc Jamin et al. "Submillisecond Unfolding Kinetics of Apomyoglobin and its pH 4 Intermediate". In: *Journal of Molecular Biology* 292.3 (Sept. 1999), pp. 731–740. ISSN: 0022-2836. DOI: 10.1006/jmbi.1999.3074.

[117] Mikio Ohgushi and Akiyoshi Wada. "'Molten-globule state': a compact form of globular proteins with mobile side-chains". In: *FEBS Letters* 164.1 (Nov. 1983), pp. 21–24. ISSN: 0014-5793. DOI: 10.1016/0014-5793(83)80010-6.

[118] O. B. Ptitsyn et al. "Evidence for a molten globule state as a general intermediate in protein folding". In: *FEBS Letters* 262.1 (Mar. 1990), pp. 20–24. ISSN: 0014-5793. DOI: 10.1016/0014-5793(90)80143-7.

[119] Yoshihiro OCHIAI et al. "Thermal Denaturation Profiles of Tuna Myoglobin". In: *Bioscience, Biotechnology, and Biochemistry* 74.8 (Aug. 2010), pp. 1673–1679. ISSN: 0916-8451. DOI: 10.1271/bbb.100290.

[120] Yoshiko Moriyama and Kunio Takeda. "Critical Temperature of Secondary Structural Change of Myoglobin in Thermal Denaturation up to 130 °C and Effect of Sodium Dodecyl Sulfate on the Change". In: *The Journal of Physical Chemistry B* 114.7 (Jan. 2010), pp. 2430–2434. ISSN: 1520-6106. DOI: 10.1021/jp908700j.

[121] Mala Nurilmala, Hideki Ushio, and Yoshihiro Ochiai. "pH- and temperature-dependent denaturation profiles of tuna myoglobin". In: *Fisheries Science* 84.3 (Apr. 2018), pp. 579–587. ISSN: 0919-9268. DOI: 10.1007/s12562-018-1198-1.

[122] Ilme Schlichting et al. "Crystal structure of photolysed carbonmonoxy-myoglobin". In: 371 (1994), pp. 808–812. ISSN: 0028-0836. DOI: 10.1038/371808a0.

[123] Henry N. Po and N. M. Senozan. "The Henderson-Hasselbalch Equation: Its History and Limitations". In: *Journal of Chemical Education* 78.11 (Nov. 2001), p. 1499. ISSN: 0021-9584. DOI: 10.1021/ed078p1499.

[124] H. Jane Dyson and Peter E. Wright. "How Does Your Protein Fold? Elucidating the Apomyoglobin Folding Pathway". In: *Accounts of Chemical Research* 50.1 (Dec. 2016), pp. 105–111. ISSN: 0001-4842. DOI: 10.1021/acs.accounts.6b00511.

[125] Jenny Keller et al. "Crystal structure of AFV3-109, a highly conserved protein from crenarchaeal viruses". In: *Virology Journal* 4.1 (Jan. 2007). DOI: 10.1186/1743-422X-4-12.

[126] J. I. Sulkowska, P. Sulkowski, and J. Onuchic. "Dodging the crisis of folding proteins with knots". In: *Proceedings of the National Academy of Sciences* 106.9 (Feb. 2009), pp. 3119–3124. DOI: 10.1073/pnas.0811147106.

[127] Pawel Dabrowski-Tumanski and Joanna Sulkowska. "To Tie or Not to Tie? That Is the Question". In: *Polymers* 9.12 (Sept. 2017), p. 454. DOI: 10.3390/polym9090454.

[128] Aleksandra I. Jarmolinska et al. “Proteins’ Knotty Problems”. In: *Journal of Molecular Biology* 431.2 (Jan. 2019), pp. 244–257. DOI: 10.1016/j.jmb.2018.10.012.

[129] Claudio Perego and Raffaello Potestio. “Computational methods in the study of self-entangled proteins: a critical appraisal”. In: *Journal of Physics: Condensed Matter* 31.44 (Aug. 2019), p. 443001. ISSN: 0953-8984. DOI: 10.1088/1361-648x/ab2f19.

[130] Alexander Begun, Alexander Molochkov, and Antti J. Niemi. “Protein tertiary structure and the myoglobin phase diagram”. In: *Scientific Reports* 9.1 (July 2019). ISSN: 2045-2322. DOI: 10.1038/s41598-019-47317-y.

[131] Martin Lundgren and Antti J. Niemi. “Knots and Swelling in Protein Folding”. In: (June 26, 2009). arXiv: 0906.4950 [cond-mat.soft].

[132] Stefan Wallin, Konstantin B. Zeldovich, and Eugene I. Shakhnovich. “The Folding Mechanics of a Knotted Protein”. In: *Journal of Molecular Biology* 368.3 (May 2007), pp. 884–893. DOI: 10.1016/j.jmb.2007.02.035.

[133] N. P. King et al. “Structure and folding of a designed knotted protein”. In: *Proceedings of the National Academy of Sciences* 107.48 (Nov. 2010), pp. 20732–20737. ISSN: 0027-8424. DOI: 10.1073/pnas.1007602107.

[134] Anna L. Mallam and Sophie E. Jackson. “Knot formation in newly translated proteins is spontaneous and accelerated by chaperonins”. In: *Nature Chemical Biology* 8.2 (Dec. 2011), pp. 147–153. ISSN: 1552-4450. DOI: 10.1038/nchembio.742.

[135] M. L. Scalley and D. Baker. “Protein folding kinetics exhibit an Arrhenius temperature dependence when corrected for the temperature dependence of protein stability”. In: *Proceedings of the National Academy of Sciences* 94.20 (Sept. 1997), pp. 10636–10640. ISSN: 0027-8424. DOI: 10.1073/pnas.94.20.10636.

[136] *Protein Data Bank*. Research Collaboratory for Structural Bioinformatics. 1971. URL: http://www.rcsb.org/pdb/home/home.do.